7-2020

Thiophene Derivative Monomers Co-electropolymerized on Microelectrodes within Arrays for Tailored Surface Chemistry and Electrochemical Properties

Benjamin J. Jones
University of Arkansas, Fayetteville

Thiophene Derivative Monomers Co-electropolymerized on Microelectrodes within Arrays for Tailored Surface Chemistry and Electrochemical Properties

A dissertation submitted in partial fulfillment
of the requirements for the degree of
Doctor of Philosophy in Chemistry

by

Benjamin J. Jones
University of Arkansas
Bachelor of Science in Chemistry, 2007

July 2020
University of Arkansas

This dissertation is approved for recommendation to the Graduate Council.

_____
Ingrid Fritsch, Ph.D.
Dissertation Director

_____
Jingyi Chen, Ph.D.
Committee Member

_____
Colin Heyes, Ph.D.
Committee Member

_____
David Paul, Ph.D.
Committee Member

Abstract

Potentiodynamic co-electropolymerization of two thiophene derivatives, (2,3-dihydrothieno[3,4-b]dioxin-2-yl)methanol (**1**) and 4-((2,3-dihydrothieno[3,4-b][1,4]dioxin-2-yl)-methoxy)-4-oxobutanoic acid (**2**), in aqueous solutions (0.02 M total monomer, 0.05 M sodium dodecyl sulfate (SDS) and 0.1 M $LiClO_4$) on gold microband electrodes in an array was investigated. A modified Steglich esterification reaction between monomer **1** and succinic anhydride produced monomer **2** at 93.6% yield. Seven deposition solutions of the two monomers, defined by mol% of monomer **2** (0, 25, 34, 50, 66, 75, 100) generated seven sets of polymer films by cyclic voltammetry in a specially designed cell to conserve monomer. The onset potential for monomer oxidation and total monomer deposited (*m*) were calculated from the deposition voltammograms. Decreasing monomer deposited (*m)* from 0 to 100 mol% **2** is attributed to a decreasing pH that inhibits electropolymerization. Cyclic voltammetry (CV) of the resulting films in aqueous buffer yielded capacitances that decrease similarly to the decrease in *m* for solutions from 0 to 75 mol% **2**. Thus, the electrochemical behavior of the polymer film itself, which depends on the ability of ions to transport through the film, is unaffected by the comonomer composition. However, for films from solutions in which only monomer **2** is present (100 mol% **2**), the capacitance is the same as the bare gold. These films have a minimal background current and further modified by a chemical reporter would make a suitable sensor platform. The facility of electron transfer at films by ferrocyanide, measured by the potential difference in CV between faradaic current peaks, was not significantly affected by the mol% **2**, either, except for the 100 mol% **2** case. The ratio of monomers **2** and **1** in the films, determined by micro-attenuated total reflectance Fourier transform infrared spectroscopy and supported by X-ray photoelectron spectroscopy, linearly tracks the ratio in the deposition solutions. It is

proposed that this deposition behavior, which differs from prior reports of other thiophene mixtures, is enabled through SDS solubilization. These studies demonstrate electrochemical capacitance of the films is unimpeded by the polymer composition and yet can be formed with predictable numbers of carboxylic acid and hydroxyl functional groups for further modification.

Dedication

This work is dedicated to my parents, Rick and Pam Jones, whose unwavering support and sacrifice serves as the foundation for all that I am able to accomplish.

Table of Contents

List of Published Papers

1. B. J. Jones, C. L. Korzeniewski, J. H. Franco, S. D. Minteer, I. Fritsch, *Journal of the Electrochemical Society*, (2020). (Submitted) – Chapters 3 and 3S.

1. Introduction to the Co-electropolymerization of Thiophene Derivatives for Tailored Surface Chemistry and Electrochemical Properties

1.1 Introduction

Conducting polymers (CPs) were initially developed by the electronics industry to fulfill their need for transparent, thermally stable, and vacuum moldable antistatic coating.[1] In the years since their initial development they have been used in a number of applications including electrochemical biosensors,[2-5] molecular electronics,[6] and energy storage.[7] Their rapid increase in applications is a direct result of the ability to change and modify the underlying monomers of the polymer films through organic synthesis, thus changing and adjusting their chemical and electronic properties.

Thiophenes are a unique subset of monomers that, when oxidatively polymerized, form intrinsic CPs. These CPs can be electrochemically generated, are stable in undoped states, and can be structurally modified to produce new and advantageous chemical characteristics.[8, 9] The type of solvent system, electrolyte, and electrochemical technique used, electrode material can affect the electrochemically generated polythiophenes (PTs). PTs have been used in the same areas as other CPs.

A specific thiophene derivative monomer relevant to this work is 3,4-ehtylenedioxythiophene (EDOT), shown in Figure 1.1. It was developed in the mid to late 1980s at Bayer AG. They found that by blocking polymerization routes at the β and β' positions by the addition of the ethylenedioxy bridge, they could force linear polymerization resulting in films with high conductivities at ambient conditions in organic solvents. The transition to use of EDOT in aqueous conditions was possible by pairing the hydrophobic monomer and polymer with the polyelectrolyte poly(styrenesulfonate) as the counter ion. The resulting films were very stable and conductive film in aqueous environments. The success of PEDOT caused researchers

to search for and develop synthetic routes to similar monomers and expand the possible chemistry.

Direct functionalization of the ethylenedioxy group is not possible and alternative synthetic routes to similar monomers lead to the development of (2,3-dihydrothieno[3,4-b]dioxin-2-yl)methanol (**1**) (Figure 1.1).[10, 11] The hydroxy group causes the new monomer to be hydrophilic and readily dissolved in aqueous solutions, does not interfere with the conductivity and linear polymerization, maintains a low oxidation potential similar to EDOT and makes further derivatization and modification possible. Carboxylic acid functional groups are also desirable because of their known reactivity and established conjugation protocols. EDOT derivatives containing carboxylic acid functional groups have been synthesized and used in DNA detection,[12] cell engineering and capturing,[13, 14] glucose sensing,[15] nanomaterial synthesis,[16] surface engineering,[17, 18] and chemical sensing.[19]

The carboxylic acid containing monomer used in this work is 4-((2,3-dihydrothieno[3,4-b][1,4]dioxin-2-yl)-methoxy)-4-oxobutanoic acid (**2**) (Figure 1.1) and can be synthesized by a modified Steglich esterification reaction between monomer **1** and succinic anhydride (Figure 1.2).[20] Much of the early work focused on the single monomer and resulting pristine polymer films.[21] However, copolymer films of monomers **1** and **2** have been produced both chemically and electrochemically at various molar ratios under different conditions for use as biocompatible interfaces and neural electrodes.[22-24]

The inspiration for this research is rooted in the desire to electrochemically functionalize microelectrodes for further derivatization. However, little is understood regarding the resulting electrochemically generated copolymer film's physical and electrochemical properties as a

function of the systematic variation of the molar ratio of the monomers in the deposition solution.

The focus of Chapter 2 is modified Steglich esterification reaction between monomer **1** and succinic anhydride to produce monomer **2**. The product was characterized by nuclear magnetic resonance spectroscopy, infrared spectroscopy, and mass spectrometry. The product was recovered at a 93.6% yield and used for the systematic copolymerization with monomer **1**.

Chapter 3 includes the co-electropolymerization of the two monomers from systematic molar rations in aqueous deposition solutions. The resulting polymer films are characterized electrochemically as well as by infrared spectroscopy and X-ray photoelectron spectroscopy to compare the relative concentration of the monomers incorporated into the film to that in the deposition solutions.

The focus of Chapter 4 is the X-ray photoelectron spectroscopy of both monomers **1** and **2** as well as their resulting polymer and copolymer films. Survey scans of all samples and narrow scans of the O(1s) and C(1s) regions are shown. A quantitative analysis of the C(1s) spectra are provided and show the relative concentration of monomers incorporated into the films to be proportional to their molar rations in the deposition solution.

This dissertation is written in such that it is compatible to be published in peer reviewed journals. Each individual chapter is the main text and any supporting information is given at the end of the chapter and labeled as Chapter Number.S.

1.2 References

1. L. B. Groenendaal, F. Jonas, D. Freitag, H. Pielartzik, and J. R. Reynolds, *Adv. Mater. (Weinheim, Ger.),* **12** (7), 481-494 (2000).

2. N. Aydemir, J. Malmstrom, and J. Travas-Sejdic, *Phys. Chem. Chem. Phys.*, **18** (12), 8264-8277 (2016).

3. S. Cosnier, *Analytical and Bioanalytical Chemistry,* **377** (3), 507-520 (2003).

4. A. Kros, R. J. M. Nolte, and N. A. J. M. Sommerdijk, *Adv. Mater. (Weinheim, Ger.),* **14** (23), 1779-1782 (2002).

5. G. Bidan, M. Billon, T. Livache, G. Mathis, A. Roget, and L. M. Torres-Rodriguez, *Synth. Met.,* **102** (1-3), 1363-1365 (1999).

6. X. Liu, *Small,* **6** (21), 2333-2335 (2010).

7. J. G. Ibanez, M. E. Rincon, S. Gutierrez-Granados, M. h. Chahma, O. A. Jaramillo-Quintero, and B. A. Frontana-Uribe, *Chem. Rev. (Washington, DC, U. S.)*, **118** (9), 4731-4816 (2018).

8. T. P. Kaloni, P. K. Giesbrecht, G. Schreckenbach, and M. S. Freund, *Chem. Mater.*, **29** (24), 10248-10283 (2017).

9. E. W. C. Chan, P. Baek, D. Barker, and J. Travas-Sejdic, *Polym. Chem.,* **6** (43), 7618-7629 (2015).

10. A. Lima, P. Schottland, S. Sadki, and C. Chevrot, *Synth. Met.*, **93** (1), 33-41 (1998).

11. J. Roncali, P. Blanchard, and P. Frere, *J. Mater. Chem.*, **15** (16), 1589-1610 (2005).

12. S.-C. Luo, H. Xie, N. Chen, and H.-h. Yu, *ACS Appl. Mater. Interfaces*, **1** (7), 1414-1419 (2009).

13. S.-C. Luo, B. Zhu, A. Nakao, R. Nakatomi, and H.-h. Yu, *Adv. Biomater. (Weinheim, Ger.),* (6), B423-B427 (2011).

14. J. Sekine, S.-C. Luo, S. Wang, B. Zhu, H.-R. Tseng, and H.-h. Yu, *Adv. Mater. (Weinheim, Ger.),* **23** (41), 4788-4792 (2011).

15. B. Kannan, D. E. Williams, C. Laslau, and J. Travas-Sejdic, *Biosens. Bioelectron.,* **35** (1), 258-264 (2012).

16. S.-C. Luo, J. Sekine, B. Zhu, H. Zhao, A. Nakao, and H.-h. Yu, *ACS Nano,* **6** (4), 3018-3026 (2012).

17. T. Darmanin and F. Guittard, *Soft Matter,* **9** (25), 5982-5990 (2013).

18. J. Malmstrom, M. K. Nieuwoudt, L. T. Strover, A. Hackett, O. Laita, M. A. Brimble, D. E. Williams, and J. Travas-Sejdic, *Macromolecules (Washington, DC, U. S.),* **46** (12), 4955-4965 (2013).

19. D. Hu, L. Zhang, K. Zhang, X. Duan, J. Xu, L. Dong, H. Sun, X. Zhu, and S. Zhen, *J. Appl. Polym. Sci.,* **132** (9), 41559/41551-41559/41559 (2015).

20. E. M. Ali, E. A. B. Kantchev, H.-h. Yu, and J. Y. Ying, *Macromolecules,* **40** (17), 6025-6027 (2007).

21. L. Zhang, Y. Wen, Y. Yao, J. Xu, X. Duan, and G. Zhang, *Electrochimica Acta,* **116** 343-354 (2014).

22. N. Bhagwat, K. L. Kiick, and D. C. Martin, *J. Mater. Res.,* **29** (23), 2835-2844 (2014).

23. N. Bhagwat, R. E. Murray, S. I. Shah, K. L. Kiick, and D. C. Martin, *Acta Biomater.,* **41** 235-246 (2016).

24. S. C. Luo, E. Mohamed Ali, N. C. Tansil, H. H. Yu, S. Gao, E. A. Kantchev, and J. Y. Ying, *Langmuir,* **24** (15), 8071-8077 (2008).

1.3 Figures

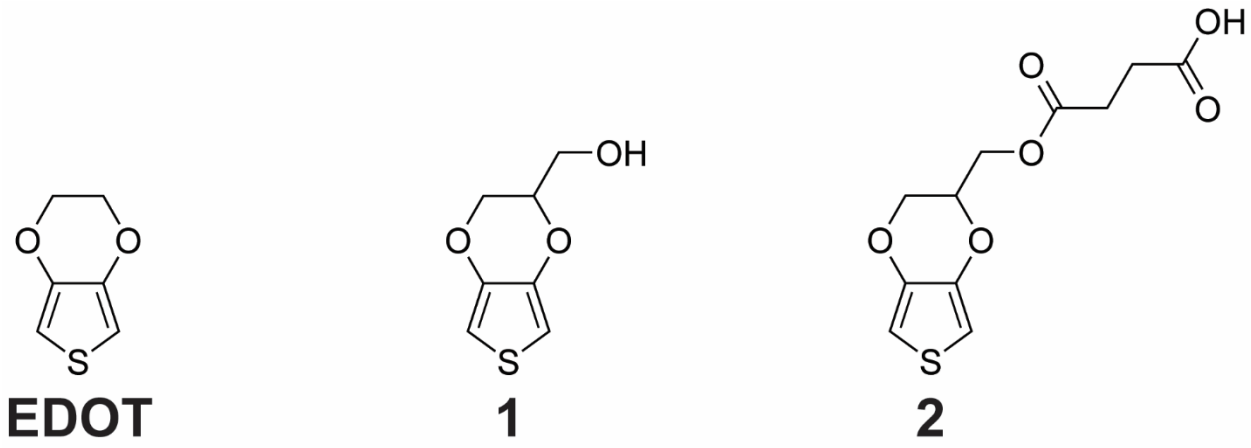

Figure 1.1 Molecular structures of monomers relevant to this work. EDOT, widely reported in the literature, shares the same base structure as **1** and **2**. Monomers **1** and **2** are synthesized independently from EDOT. Monomer **2** is synthesized from **1.**

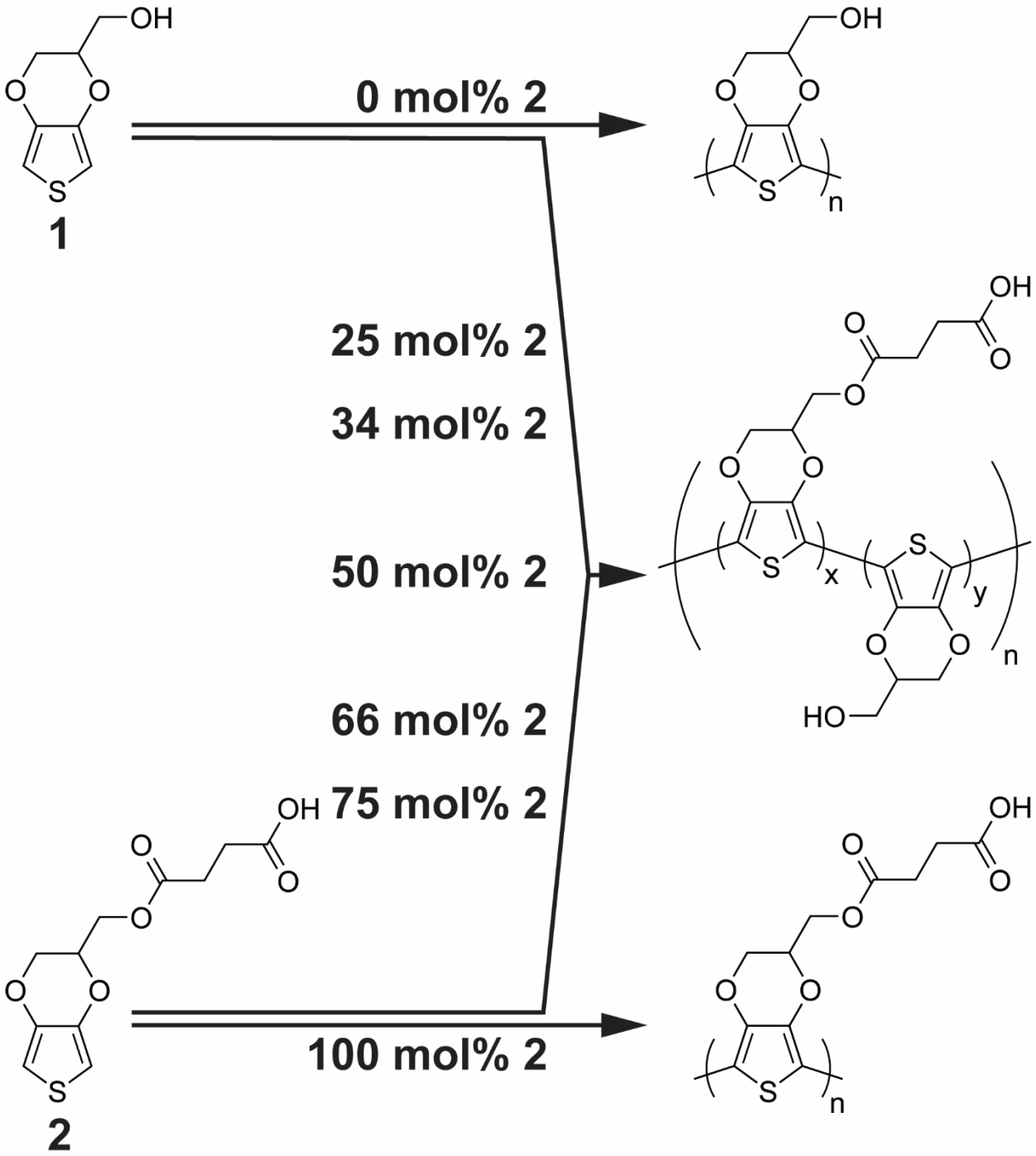

Figure 1.2. Strategy for electropolymerization of monomers **1** and **2** to form copolymer blends. The deposition solutions studied contained the following monomer **2** compositions: 0, 25, 34, 50, 66, 75, and 100 mol% **2**, where mol% **2** = [mol **2** / (mol **1** + mol **2**)] × 100%. The total monomer concentration in the deposition solutions was maintained constant at 0.02 M.

2. Synthesis and Characterization of 4-((2,3-dihydrothieno[3,4-b][1,4]dioxin-2-yl)-methoxy)-4-oxobutanoic acid

2.1 Abstract

A modified Steglich esterification was used to synthesize 4-((2,3-dihydrothieno[3,4-b][1,4]dioxin-2-yl)-methoxy)-4-oxobutanoic acid from (2,3-dihydrothieno[3,4-b]dioxin-2-yl)methanol and succinic anhydride. The product was recovered at 93.6% yield and characterized by proton nuclear magnetic resonance spectrometry, attenuated total reflectance Fourier transform infrared spectrometry, and liquid chromatography coupled with mass spectrometry. The results of the product characterizations were compared to the same characterizations of the starting materials.

2.2 Introduction

The ability to customize and tailor the surface of an electroactive material is fundamental to both energy conversion and bio-sensing applications.[1-3] In addition to creating customized electroactive surfaces there are also application based and economic factors pushing these technologies to miniaturized platforms. For example, a biofuel cell used to power implanted electronic devices must be small enough to implant and use in a practical manner.[4] There are a multitude of materials and strategies to create conductive and tailored surfaces for small devices and in almost all instances these strategies rely upon a technique known as drop-casting for surface modification. In brief, required materials, usually a carrier solvent, cross-linking agent, conductive material, and specific redox active species, are mixed in a slurry that is then physically dropped onto a conductive surface. The cross-linking agent links the required materials together in the carrier solvent before the solution is physically dropped onto the surface. After some time, the carrier solvent evaporates leaving a customized and tailored electrochemically active and conductive surface. This is a "top down" approach where the building blocks are put together first and then deposited onto a foundation. This method is excellent for rapid preparation of electrode surfaces but suffers from low spatial resolution. It is difficult to control the spread of the drop cast as well as the resulting film thickness and even distribution of materials.

As devices become further miniaturized and both electrode size and spacing is minimized, drop casting becomes less practical and a "bottom up" approach to electrode surface modification is desired. Using the electrochemical technique of oxidative polymerization is one approach to modify small electrodes with small gaps in a programmable and controllable manner. A requirement of this technique is to use electrochemically active monomers. One such

monomer that has received much attention in a variety of applications such as antistatic coatings, electrochromic devices, electrochemical capacitors, and biosensing, due to its stable chemical structure and high conductivity in a wide variety of environments is 3,4-ehtylenedioxythiophene (EDOT), shown in Figure 2.1.[5, 6] Despite its many advantages, such as low oxidation potential, linear polymerization, and stability in physiological and ambient conditions, EDOT cannot be further derivatized, because it lacks a synthetically accessible functional group, while keeping the thiophene ring intact. However, there are other thiophene derivatives other than EDOT, that share the same base structure, that also have similar characteristics and can be further derivatized to create monomers for tailored surface chemistry of miniaturized electrodes.[7]

The thiophene derivative (2,3-dihydrothieno[3,4-b]dioxin-2-yl)methanol (**1**) (Figure 2.1) has the advantage of being electrochemically similar to EDOT but also has the ability to be further derivatized by way of the hydroxyl group. Another EDOT derivative, 4-((2,3-dihydrothieno[3,4-b][1,4]dioxin-2-yl)-methoxy)-4-oxobutanoic acid (**2**), shown in Figure 2.1, has a slightly different structure but with a tethered carboxylic acid. The addition of the carboxylic acid provides the possibility of further derivatization away from the base structure as well as offer suitability for well-known conjugation chemistry, such as the formation of amide linkages with primary amines in amino acid residues. Although monomer **1** is commercially available, monomer **2** must be synthesized in the lab, and procedures have been reported previously. One approach, which is used in this work, is a modified Steglich reaction, where 4-(dimethylamino)pyridine (DMAP) is used to catalyze the esterification, shown in Figure 2.2.

To ensure the reaction was successful, characterization of the product, as well as the starting materials, was performed by proton nuclear magnetic resonance (^{1}H NMR) spectrometry, attenuated total reflectance Fourier transform infrared (ATR-FTIR) spectrometry,

and analysis by liquid chromatography coupled to electrospray ionization and mass spectrometry (LC-ESI-MS).

2.3 Experimental

2.3.1 Chemicals and materials. All chemicals were reagent grade and used as received unless otherwise specified. Succinic anhydride (SA), 4-(dimethylamino)pyridine (DMAP), triethylamine (Et_3N), and monomer **1** were obtained from Sigma Aldrich (St.Louis, MO, USA). Concentrated hydrochloric acid (HCl), dichloromethane (DCM), and alumina (Neutral, Brockman Activity I) were purchased from Fisher Scientific (Pittsburg, PA, USA). Sodium chloride (NaCl), magnesium sulfate ($MgSO_4$), and acetonitrile (MeCN), were obtained from EMD Chemicals (Billerica, MA, USA). Deuterated chloroform ($CDCl_3$) was purchased from Cambridge Isotopes Labs (Tewksbury, MA, USA). All aqueous solutions were prepared using ACS reagent grade water, ASTM Type I, ASTM Type II (H_2O) from RICCA Chemical Company (Arlington, TX, USA). Dry, industrial grade, nitrogen gas (N_2) was purchased from Airgas (Radnor Township, PA, USA).

2.3.2 Synthesis. The synthesis of monomer **2** is a modified Steglich esterification between the hydroxy group of monomer **1** and the carboxylate anion from the opened succinic anhydride based on previously reported procedures.[8] The overall reaction schematic is shown in Figure 2.2. All glassware was cleaned, rinsed, and dried prior to use. DCM was dried over alumina in a glass chromatography column with solvent reservoir and fritted disc prior to use.

A N_2 stream was set up with tubing from the cylinder to a glass T-shaped tubing connector. One end of the T was connected to tubing that lead to a glass bubbler filled with mineral oil to observe the flow rate of the gas. The other end of the T was connected by tubing to a glass inlet adapter fitted with a reducer with a stopcock.

A 150 mL three neck, round-bottomed flask was fitted with glass stoppers and a rubber septum and purged with N_2 before and after the addition of reagents. An oval stir bar, 452.7 mg (2.629 mmol) of monomer **1**, and approximately 25 mL of DCM were added to the flask. The reaction flask was placed on a cork ring on a magnetic stirrer and connected to the N_2 stream. A 20 mL glass vial was used to contain a small stir bar, 562.7 mg (5.632 mmol, 2.1 mol eq.) SA, 28.6 mg (0.2 mmol, 0.9 mol eq.) DMAP, 0.527 mL Et_3N, and 10 mL DCM. They were stirred until dissolved. This mixture was drawn into a glass syringe fitted with a clean needle used to pierce the rubber septum of the three neck round bottom flask. The mixture was added to the flask dropwise over a period of 5 min while stirring. After completing the addition of the SA solution, the reaction continued at room temperature for 8 h with continuous stirring under N_2. The product was worked up by washing with approximately 40 mL of a 10% HCl solution followed by consecutive rinses with a saturated NaCl solution until the pH of the used rinse solution increased to that of the unused rinse solution (pH ~5). The product was then dried over $MgSO_4$ twice and residual solvent was evaporated under vacuum.

2.3.3 ^{1}H NMR. All ^{1}H NMR spectra were obtained on a 400 MHz Bruker (Billerica, MA, USA) spectrometer with Z gradient and broadband probe using a standard pulse program and analyzed with TopSpin 4.0.6 software. All spectra, except the product, are the result of 16 scans; the product spectrum is a result of 32 scans (δ -4 to δ 16, total of 131,702 data points). About 1 mg of the starting materials, catalyst, and product were put into separate standard NMR tubes and dissolved with $CDCl_3$. Peak integration and multiplet definition were calculated using TopSpin and the total sum of the peak integration was normalized to 7 and 11 for monomers **1** and **2**, respectively.

Spectra were also simulated using the online ^{1}H NMR prediction tool found at nmrdb.org (https://www.nmrdb.org/new_predictor/index.shtml?v=v2.115.0).[9] The simplified molecular-input line-entry system (SMILES) notation for monomer **1** (OCC2COc1cscc1O2), monomer **2** (O=C(O)CCC(=O)OCC2COc1cscc1O2), and SA (O=C1CCC(=O)O1) were used to generate the appropriate structures for the simulations. To approximate conditions closest to the actual measurement, the advanced options were set to a frequency of 400, a range from δ -4 to δ 16, a line width of 1 Hz, and the number of points to 512k.

2.3.4 ATR-FTIR. All ATR-FTIR spectra were obtained using a Shimadzu (Kyoto, Japan) IRAffinity-1S spectrophotometer fitted with a Specac (Orpington, Kent, UK) Quest ATR accessory and kept on the bench at ambient conditions. Spectra were analyzed with Shimadzu LabSolutions IR software. Prior to, and between measurements, the ATR puck and crystal were cleaned with acetone and enough time was given for them to fully dry. Interferograms of monomers **1** and **2** were recorded at 0.5 cm^{-1} resolution with 40 scans averaged and processed using triangular apodization before Fourier transformation. The interferogram of SA was recorded at 4 cm^{-1} resolution with 64 scans averaged and processed using the Happ-Genzel apodization before Fourier transformation. Spectra are displayed in units of pATR where,

$$pATR = -\log \frac{I_{sample}}{I_{background}} \quad [1]$$

and I_{sample} and $I_{background}$ represent the sample and background single beam spectra, respectively.

2.3.5 Mass Spectrometry. A Shimadzu 8040 triple quadrupole mass spectrometer interfaced with an ultra performance liquid chromatography (UPLC) system and equipped with an electrospray ionization (ESI) source was used to generate spectra of monomers **1** and **2**. The Shimadzu C18 (50 × 4.6 mm, 3 μm particle size) column was kept at 40 ˚C. Samples were

prepared for analysis by dissolving approximately 1 mg in a 9:1 v/v MeCN:H_2O solution. All sample volumes were 1 µL and the flow was kept at 0.5 mL/min. A solvent program consisting of LC-MS grade H_2O and MeCN with 0.1% formic acid were used. In the case of monomer **1**, the solvent program consisted of 10% MeCN for 3 min, a ramp up to 90% MeCN from 3-13 min, held at 90% MeCN for 1 min, and finally brought back to 10% MeCN to clean and equilibrate the column. In the case of monomer **2**, the solvent program consisted of 10% MeCN for 1 min, a ramp up to 80% MeCN from 1-8 min, held for 1 min, and finally brought back to 10% MeCN to clean and equilibrate the column. The desolvation line was kept at 250 ˚C and N_2 was used as the drying (18 L/min) and nebulizing (3 L/min) gas. A Q3 scan was used, where the first three quadrupoles are used as ion guides and the last quadrupole is scanned to obtain the spectrum, in positive ion mode. Each scan was 1 s and repeated throughout the entirety of the LC run. For monomer **1** the Q3 was scanned from 140 – 800 *m/z* and for monomer **2** from 150 – 700 *m/z*.

2.4 Results and Discussion.

A proposed mechanism of reaction is given in Figure 2.3.[10] The modified Steglich esterification reaction begins with the nucleophilic attack of one of the two carbonyl carbons of SA by the pyridyl group of DMAP. The resulting acylated DMAP undergoes a nucleophilic attack by the hydroxyl group of monomer **1** followed by intramolecular rearrangement ultimately leading to the release of DMAP and monomer **2**. It is important to keep all reagents, solvents, glassware, and the local environment of the reaction as dry as possible. The presence of excess H_2O can inhibit the reaction at step (c) of Figure 2.3 reverting the reactants back to monomer **1** and succinate. The resulting product, monomer **2**, was collected as a light brown viscous liquid, recovered with a 93.6% yield, and stored at 4 ˚C where the product turned into a light tan solid with the consistency of wax.

2.4.1 ^{1}H NMR. Measured spectra for SA and monomers **1** and **2**, (Figures 2.4 – 2.6) were compared with simulated spectra (Figures 2.7a-c). Table 2.1 lists the chemical shift (δ), multiplet type (Mult.), and coupling constant (*J*) of the measured (Figures 2.4 – 2.6) and simulated (Figures 2.7a-c) spectra. While there are reports on the synthesis and application of both monomers **1** and **2,** published ^{1}H NMR spectra and detailed analysis of those spectra are rare. There is a chiral center within monomers **1** and **2** at the carbon that is bound to the proton labeled 3 in the structures shown in Figures 2.5 – 2.6, however chirality was not considered in the following analysis.

The qualitative identifying feature of monomer **2** in the measured NMR spectrum, shown in Figure 2.6, is the unresolved multiplet ranging from δ 2.66 – 2.78 (4.299 H). It is the result of the spin coupled protons of the methylene groups (5, 5', 6, 6') between the ester and carboxylic acid. Although in the measured spectrum, the unresolved multiplet appears as a singlet, the simulated spectrum of monomer **2** (Figure 2.7c) assigns a series of triplets from δ 2.73 – 2.83 for the same protons. The same protons of the starting material, SA, produce a singlet in the measured spectrum (Figure 2.4) at δ 2.91 (4 H). This feature is absent in the measured and simulated spectra of monomer **1** shown in Figure 2.5 and Table 2.1, respectively, confirming that the spectra for monomer **2** is not simply a mixture of the starting materials.

The next region of interest for monomer **2** contains a series of multiplets from δ 4.06 – 4.44 in the measured spectrum (Figure 2.6). These multiplets are from the spin coupling of the protons between the ester and dioxy bridge of monomer **2**. Spin coupling and shielding effects complicate the features and the simulated spectrum was relied upon to make the following, more detailed, proton assignments. Moving downfield across the spectrum there are two doublets of doublets followed by an unresolved complex multiplet. The first doublet of doublet appears

centered at δ 4.06 (J = 11.7, 6.9 Hz) in the measured spectrum. The simulated spectrum (Figure 2.7c) assigned a similar feature to the 2 and 3 protons (δ 4.07, 2 H, J = 13.3, 9.7 Hz). The second doublet of doublets of Figure 2.6 is centered at δ 4.24 (J = 11.7, 1.9 Hz) and the simulation assigned this to the 2' proton. The simulated spectrum predicted this feature at a chemical shift that is farther upfield (δ 3.93). The closely matching coupling constants of the measured spectrum determined the proton assignment of the features in this instance, over the exact chemical shift. The next region of interest in the measured spectrum for monomer **2** is the unresolved multiplet from δ 4.30 – 4.44 resulting from the 3, 4, and 4' protons. The simulated spectrum shows something different; a simple doublet at δ 4.41 that is from the 4 and 4' protons. However, the coupling constant of this simulated doublet (3.3 Hz) is the same as the simulated triplet in the feature at δ 4.08 (Table 2.1). The coupling constants and proximity of the protons lead to the assignment of the measured spectrum. Also, as previously mentioned, chirality was not considered and may contribute to the difference between the measured and simulated spectra in this region as it directly involves the chiral center. A quick inspection of the measured spectrum (Figure 2.5) and simulated results (Table 2.1) for monomer **1** show similar features to the ones already described in this region except shifted slightly upfield. It should be noted that for monomer **1**, a primary alcohol, hydrogen bonding of the hydroxyl proton complicates the spin coupling to the neighboring protons of the methylene group and the chiral carbon. There is a high chance of atmospheric H_2O absorption by the $CDCl_3$ over time in the lab and the hydroxyl proton is most likely in rapid exchange with acidic impurities and therefore its peak is masked in the other features, as well as the carboxylic proton of monomer **2**.[11] As expected, these features are absent in both the measured (Figure 2.4) and simulated spectra of SA (Figure 2.7a).

The final region of interest in the ^{1}H NMR spectra is from δ 6.37 – 6.38 of Figure 2.6, corresponding to δ 6.25 – 6.26 of Figure 2.5, and the simulated (Figure 2.7b-c) regions of δ 6.10 and δ 6.11 – 6.24 of monomers **1** and **2**, respectively. The features in this area of the spectra are due to the protons directly associated with the thiophene ring, labeled 1 and 1'. In the case of Figure 2.6 the calibrated sum of integrals resulted in an unexpectedly low value (1.404) where 2 H was predicted. This could be attributed to the resonance of the thiophene ring and possible hydrogen bonding with solvent impurities, as mentioned previously. The features are two doublets, as both protons are spin coupled, and is consistent in the measured and simulated spectra. There is an unassigned feature in Figure 2.5 at δ 6.09 that cannot be attributed to any of the protons in monomer **1** and was not consistent with a chemical shift of a common lab solvent as the contaminant. It was left unassigned and not considered in the integration. The main difference between the measured and simulated spectra in this region is that the measured spectra do not show a well resolved set of doublets as the simulated spectra show. The simulation of monomer **2** (Figure 2.7b) shows a separation of roughly 0.13 ppm whereas in the measured spectrum there is no separation.

2.4.2 ATR-FTIR. ATR-FTIR spectra of monomer **1**, monomer **2**, and SA from 500 – 1900 cm^{-1} are shown in Figures 2.8a-c. Most of the IR information for the two monomers reported in the literature are qualitative comparisons of the monomer units and their respective pristine polymers. The focus is on one or two regions of the spectrum that are different between the two monomers. The following is a more detailed assessment of some key features of the spectra, as well as an assignment of the prominent peaks in the fingerprint region. This was done by reviewing what has been reported for both monomer and polymer forms of the same

molecules, and in some instances, different thiophene derivatives that have a similar structure to the monomers used in this work.

Esters and carboxylic acid functional groups absorb IR at a predictable range of wavenumbers. These two groups are present in monomer **2** and can be used to further identify it from the starting materials, monomer **1** and SA. Carbonyls typically result in strong absorption peaks from 1585 - 1875 cm^{-1}. Figure 2.8 shows absorption in this region for both monomer **2** (Figure 2.8c) and SA (Figure 2.8a), as both molecules have carbonyls, and as expected, a lack of absorption by monomer **1** (Figure 2.8b). The spectrum of monomer **2** (Figure 2.8c) has two peaks, the first at 1699 cm^{-1} (ν $C{=}O_{carboxylic\ acid}$) and the second at 1735 cm^{-1} (ν $C{=}O_{ester}$). There are two peaks in the spectrum of SA (Figure 2.8a), a saturated cyclic anhydride, at 1775 and 1857 cm^{-1} due to symmetric (ν_s) and asymmetric (ν_{as}) stretching modes of the carbonyl groups.[12] This is evidence that the product of the synthesis is distinct from the starting materials and contains an ester and carboxylic acid as expected. The fingerprint region (600 – 1500 cm^{-1}) of the spectra for monomers **1** and **2** (Figures 2.8b-c) each have a series of four peaks, three of which are within 13 cm^{-1} of each other. The first peak located at 750 cm^{-1} for monomer **2** and 753 cm^{-1} for monomer **1** is from the bending of the C-H bond of the thiophene ring.[13-15] The second peak in the spectrum of monomer **2** (913 cm^{-1}) is due to stretching between the C-S-C bonds of the thiophene ring.[16] The second peak in the spectrum of monomer **1** (1011 cm^{-1}) is due to stretching of the ethylenedioxy ring of the monomer.[13, 17] Spectra of both monomers have these same features, and although the peaks are not equally intense in each spectrum, they appear in the same range. The third peak in each spectrum is located at 1174 and 1187 cm^{-1} for monomers **2** and **1**, respectively.[18, 19] IR absorbance in this range is due to a combination of stretching of the C-O-C bonds of the ethylenedioxy ring and the C=C bonds in the thiophene

ring.[16, 18, 19]. The fourth and final peak in the fingerprint region occurs at 1483 cm^{-1} in the spectrum of monomer **2** and 1488 cm^{-1} in the spectrum of monomer **1** and is from the stretching and bending modes of the C=C, C-C, and C-H bonds of the thiophene ring.[13, 15-17, 19-21]

2.4.3 LC-ESI-MS. Only monomers **1** and **2** were characterized by mass analysis. The total ion and liquid chromatograms of monomer **1** are shown in Figures 2.9 – 2.10. There is only one large peak in the total ion chromatogram (Figure 2.9) at 5.53 min that corresponds to the peak at the same time in the liquid chromatogram (Figure 2.10). The mass spectrum of that peak is shown in Figure 2.11 and the base peak is the protonated monomer **1** (*m/z* 173.0 $[M+H]^+$). The total ion chromatogram of monomer **2** is shown in Figure 2.12 and has a large peak at 5.73 min and a couple of much smaller peaks at 6.75 and 7.30 min. The corresponding liquid chromatogram (Figure 2.13) detected only one species that absorbed 254 nm at 5.73 min, and there was no absorbance at 6.75 or 7.30 min. The mass spectrum of that elution is shown in Figure 2.14 where the base peak is the expected protonated monomer **2** (*m/z* 273.1 $[M+H]^+$). The subsequently labeled peaks are sodiated (*m/z* 295.0 $[M+Na]^+$) and potassiated (*m/z* 313.1 $[M+K]^+$) monomers and dimers (*m/z* 545.1 $[2M+H]^+$, *m/z* 567.1 $[2M+Na]^+$, *m/z* 583.1 $[2M+K]^+$) of **2**. Because the initial separation only has one peak it can be determined that the dimerization of the monomer took place during the ionization step, which is not uncommon, and was detected by the mass analyzer.

2.5 Conclusion

A modified Steglich esterification reaction was used to produce monomer **2** with a 93.6% yield from the starting materials: monomer **1** and SA. Further analysis of the product and starting materials by ^1H NMR, ATR-FTIR, and LC-ESI-MS show that not only was the product distinct from the starting materials but that the product was indeed monomer **2** and recovered without

measurable side products. These results demonstrate a reliable and reproducible synthesis and characterization of a thiophene derivative with additional carboxylic functionality for further derivatization with additional functional groups, electrochemically active moieties, or conjugation with enzymes of interest through established protocols. Monomers **1** and **2** have advantageous similarities such as low oxidation potentials and the same base thiophene structure but also contrasting features. Monomer **1** is hydrophobic whereas monomer **2** is hydrophobic, monomer **1** has a shorter side chain compared to monomer **2**. The similarities and differences can be exploited by their co-electropolymerization to form unique and tailored surfaces on electroactive materials.

2.6 Acknowledgements

We are grateful for financial support from the National Science Foundation (CBET-1336853 and CMI-1808286), the Arkansas Biosciences Institute, the major research component of the Arkansas Tobacco Settlement Proceeds Act of 2000, as well as Grant Number P30 GM103450 from the National Institutes of General Medical Sciences of the National Institutes of Health (NIH). We recognize the support of the Arkansas Statewide MS facility staff and their help in obtaining the LC-ESI-MS data.

2.7 References

1. A. Heller, *Acc. Chem. Res.*, **23** (5), 128-134 (1990).

2. D. J. Daly, C. K. O'Sullivan, and G. G. Guilbault, *Talanta*, **49** (3), 667-678 (1999).

3. N. D. J. Yates, M. A. Fascione, and A. Parkin, *Chem-Eur J*, **24** (47), 12164-12182 (2018).

4. A. Zebda, S. Cosnier, J. P. Alcaraz, M. Holzinger, A. Le Goff, C. Gondran, F. Boucher, F. Giroud, K. Gorgy, H. Lamraoui, and P. Cinquin, *Sci Rep*, **3** 1516 (2013).

5. L. B. Groenendaal, F. Jonas, D. Freitag, H. Pielartzik, and J. R. Reynolds, *Adv. Mater. (Weinheim, Ger.)*, **12** (7), 481-494 (2000).

6. K. B. Akshaya, T. P. Vinod, M. Nidhin, A. Varghese, and L. George, *Journal of the Electrochemical Society*, **165** (13), B582-B595 (2018).

7. L. B. Groenendaal, G. Zotti, P.-H. Aubert, S. M. Waybright, and J. R. Reynolds, *Adv. Mater. (Weinheim, Ger.)*, **15** (11), 855-879 (2003).

8. E. M. Ali, E. A. B. Kantchev, H.-h. Yu, and J. Y. Ying, *Macromolecules*, **40** (17), 6025-6027 (2007).

9. Y. Binev, M. M. B. Marques, and J. Aires-de-Sousa, *Journal of Chemical Information and Modeling*, **47** (6), 2089-2097 (2007).

10. S. Xu, I. Held, B. Kempf, H. Mayr, W. Steglich, and H. Zipse, *Chemistry*, **11** (16), 4751-4757 (2005).

11. R. M. Silverstein, F. X. Webster, and D. Kiemle, *Spectrometric Identification of Organic Compounds, 7th Edition*, Wiley (2005).

12. B. C. Smith, *Spectroscopy*, **33** (3), 16-17,19-20 (2018).

13. A. Szkurlat, *Electrochimica Acta*, **48** (24), 3665-3676 (2003).

14. T. Bahry, Z. Cui, A. Deniset-Besseau, M. Gervais, C. Sollogoub, T.-T. Bui, and S. Remita, *New Journal of Chemistry*, **42** (11), 8704-8716 (2018).

15. S. Ghosh, H. Remita, L. Ramos, A. Dazzi, A. Deniset-Besseau, P. Beaunier, F. Goubard, P.-H. Aubert, F. Brisset, and S. Remita, *New J. Chem.*, **38** (3), 1106-1115 (2014).

16. Y. Yao, Y. Wen, L. Zhang, Z. Wang, H. Zhang, and J. Xu, *Anal. Chim. Acta*, **831** 38-49 (2014).

17. F. Tran-Van, S. Garreau, G. Louarn, G. Froyer, and C. Chevrot, *Journal of Materials Chemistry*, **11** (5), 1378-1382 (2001).

18. P. Damlin, C. Kvarnström, and A. Ivaska, *Journal of Electroanalytical Chemistry*, **570** (1), 113-122 (2004).

19. C. Kvarnstrom, H. Neugebauer, S. Blomquist, H. J. Ahonen, J. Kankare, and A. Ivaska, *Electrochim. Acta*, **44** (16), 2739-2750 (1999).

20. B. Wei, L. Q. Ouyang, J. L. Liu, and D. C. Martin, *Journal of Materials Chemistry B*, **3** (25), 5028-5034 (2015).

21. Y. Lattach, A. Deniset-Besseau, J.-M. Guigner, and S. Remita, *Radiat. Phys. Chem.*, **82** 44-53 (2013).

2.8 Tables

Table 2.1. Simulated and measured ^{1}H NMR (400 MHz, $CDCl_3$) chemical shifts of monomers **1** and **2**.

	Monomer 1						Monomer 2					
	Simulated			Measured			Simulated			Measured		
Proton	δ	Mult.*	J (Hz)	δ	Mult.*	J (Hz)	δ	Mult.*	J (Hz)	δ	Mult.*	J (Hz)
1	6.10	d	2	6.25	d	3.6	6.11	d	2	6.37	d	3.6
1’	6.10	d	2	6.26	d	3.7	6.24	d	2	6.38	d	3.6
2	3.98	dd	13.2, 9.7	3.71-4.27	m		4.07	dd	13.3, 9.7	4.06	dd	11.7, 6.9
2’	3.87	dd	13.2, 1.6	3.71-4.27	m		3.93	dd	13.3, 1.6	4.24	dd	11.7, 1.9
3	3.99	dtd	9.7, 5.6, 1.6	3.71-4.27	m		4.08	dtd	9.7, 3.3, 1.3	4.30-4.44	m	
4	3.81	d	5.6	3.71-4.27	m		4.41	d	3.3	4.30-4.44	m	
4’	3.81	d	5.6	3.71-4.27	m		4.41	d	3.3	4.30-4.44	m	
5							2.73	t	7.4	2.66-2.78	m	
5’							2.73	t	7.4	2.66-2.78	m	
6							2.83	t	7.4	2.66-2.78	m	
6’							2.83	t	7.4	2.66-2.78	m	

*d = doublet, t = triplet, m = unresolved multiplet

2.9 Figures

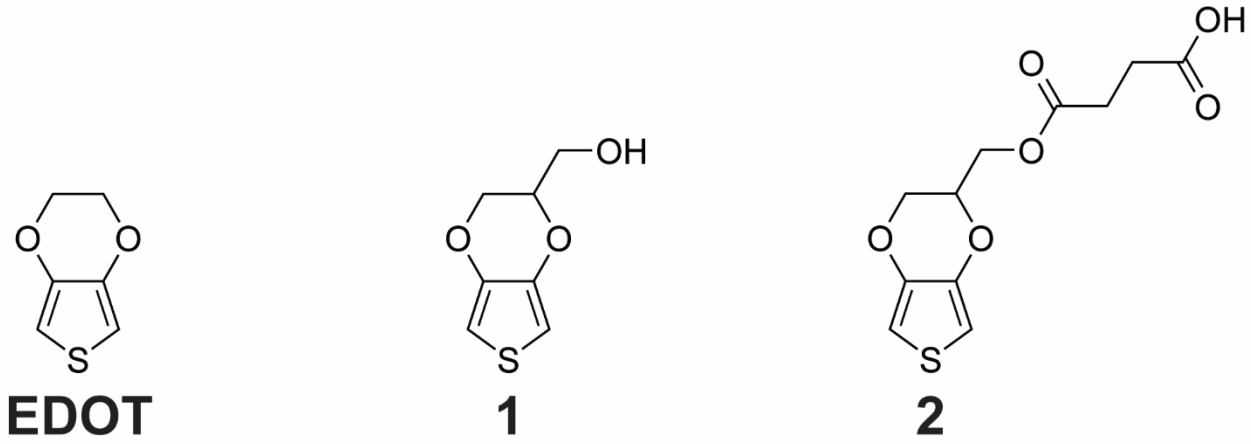

Figure 2.1. Molecular structures of the thiophene derivatives relevant to this work. EDOT, widely reported in the literature, shares the same base structure as **1** and **2**. Monomers **1** and **2** are synthesized independently from EDOT. Monomer **1** is commercially available and **2** is synthesized by a modified Steglich esterification reaction between **1** and SA.

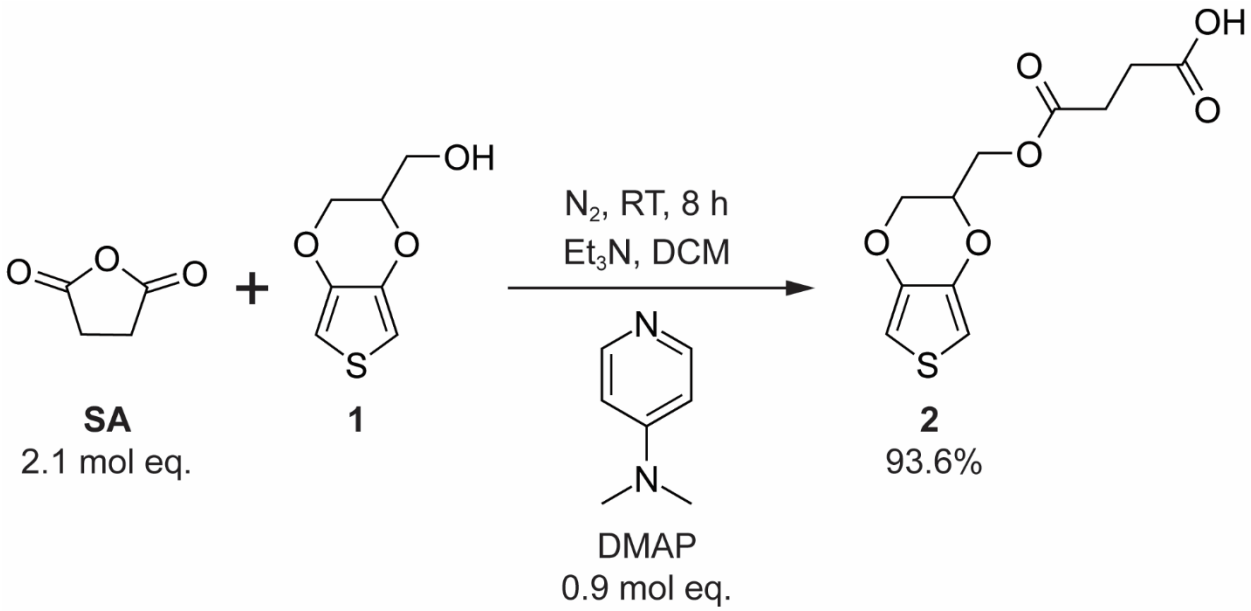

Figure 2.2. The modified Steglich esterification reaction to produce monomer **2** from monomer **1** and SA. The reaction is catalyzed by DMAP in dichloromethane (DCM) under a N_2 stream at room temperature (RT) and stirring for 8 h. The presence of triethylamine (Et_3N) serves to regenerate the catalyst.

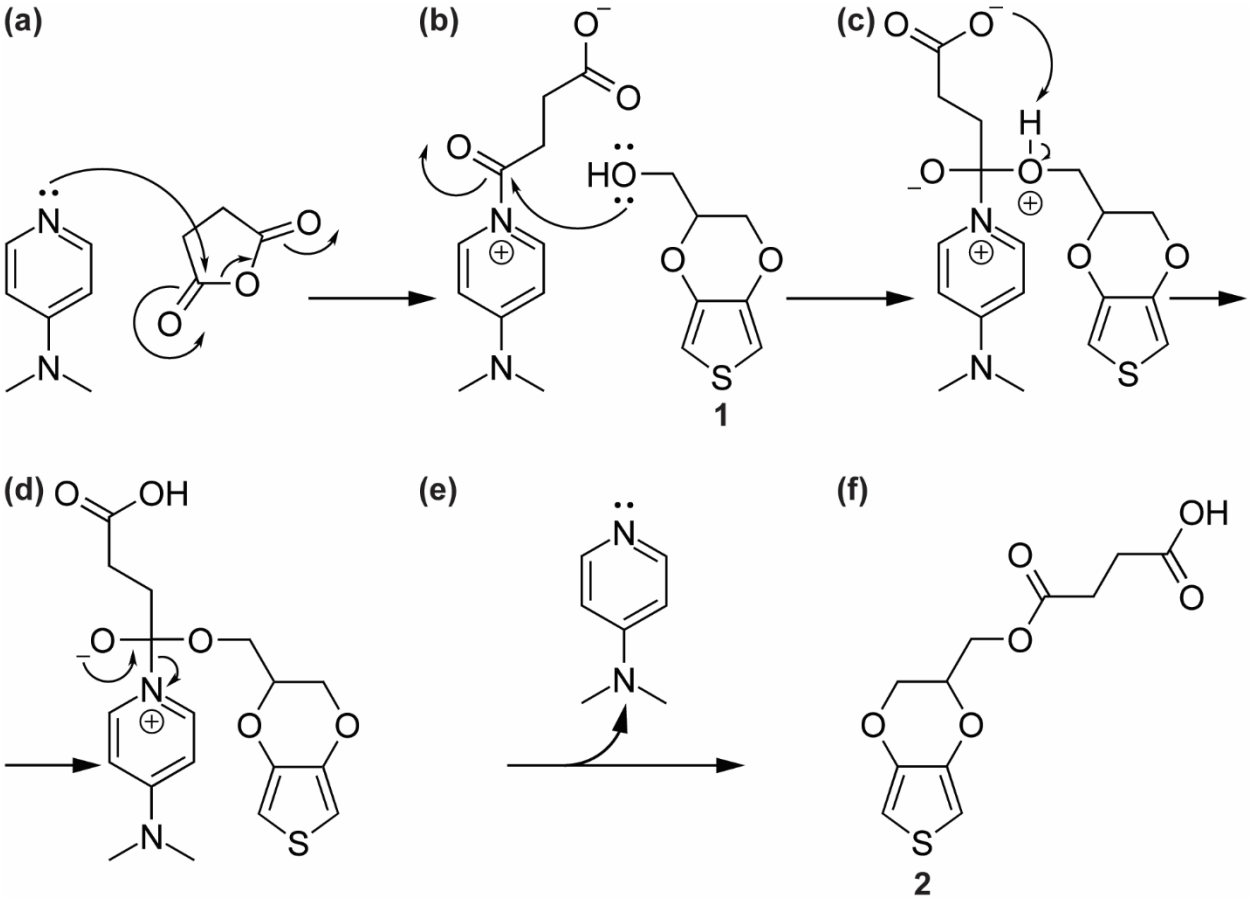

Figure 2.3. A proposed mechanism of the modified Steglich esterification reaction to produce monomer **2** from monomer **1** and SA. **(a)** The first step is a nucleophilic attack of one of the two carbonyl carbons in SA by the pyridyl group of DMAP. **(b)** The hydroxyl group of monomer **1** then reacts with the carbonyl carbon of the acylated DMAP. **(c)** The carboxylate ion attacks the proton in the intermediate complex which leads to **(d)** further intramolecular rearrangement, and ultimately **(e)** the release of DMAP and **(f)** formation of the product, monomer **2**.

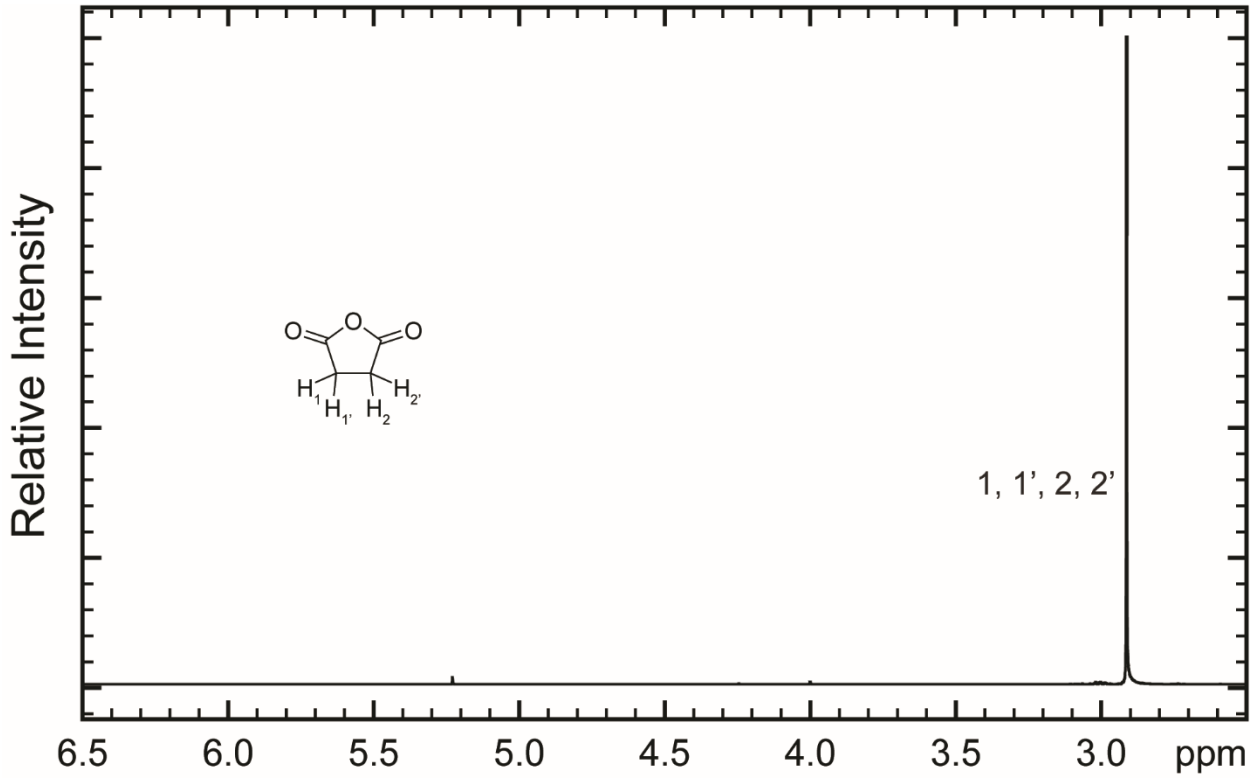

Figure 2.4. The ^{1}H NMR (400 MHz) spectrum of SA dissolved in $CDCl_3$. This spectrum is shown to highlight the peak around δ 2.9 that is the result of all four protons within the molecule.

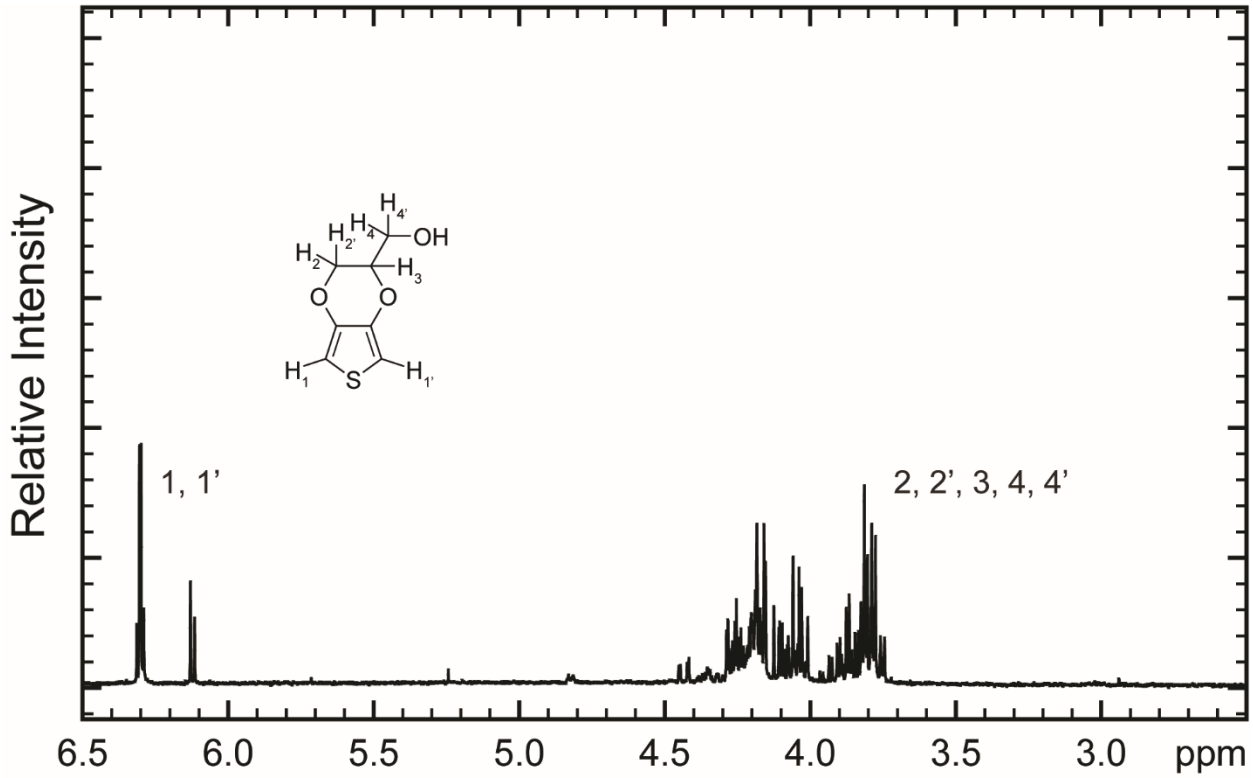

Figure 2.5. The ^{1}H NMR (400 MHz) spectrum of monomer **1** dissolved in $CDCl_3$. This spectrum is shown to highlight the complex multiplet from δ 3.7 – 4.3, that is the result of H_2, $H_{2'}$, H_3, H_4, and $H_{4'}$. The feature at δ 6.2 is from H_1 and $H_{1'}$.

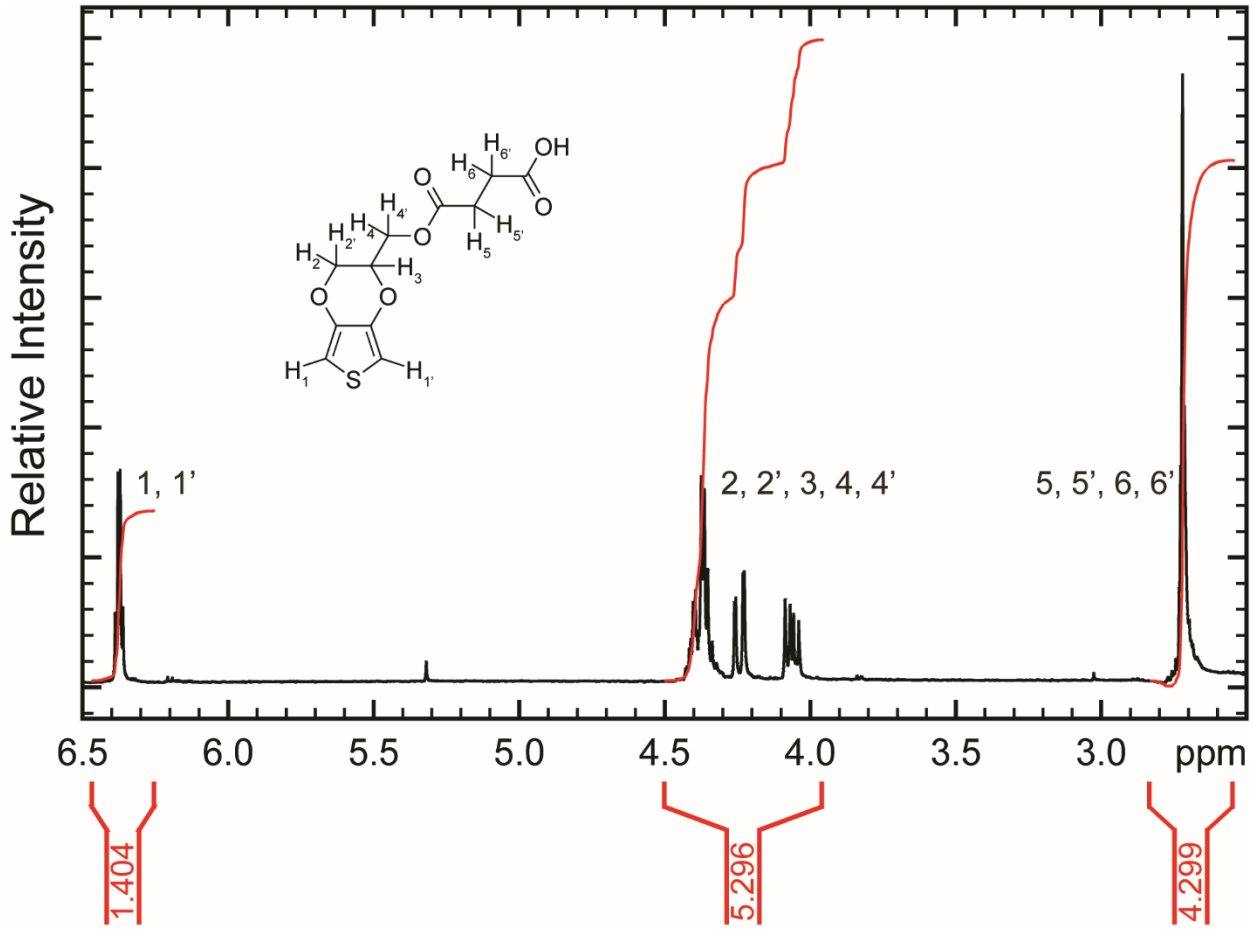

Figure 2.6. The ^{1}H NMR (400 MHz) spectrum of monomer **2** dissolved in $CDCl_3$. The feature qualitatively identifying monomer **2** in the spectrum is the multiplet from δ 2.7 – 2.74, which is due to H_5, $H_{5'}$,H_6, and $H_{6'}$.

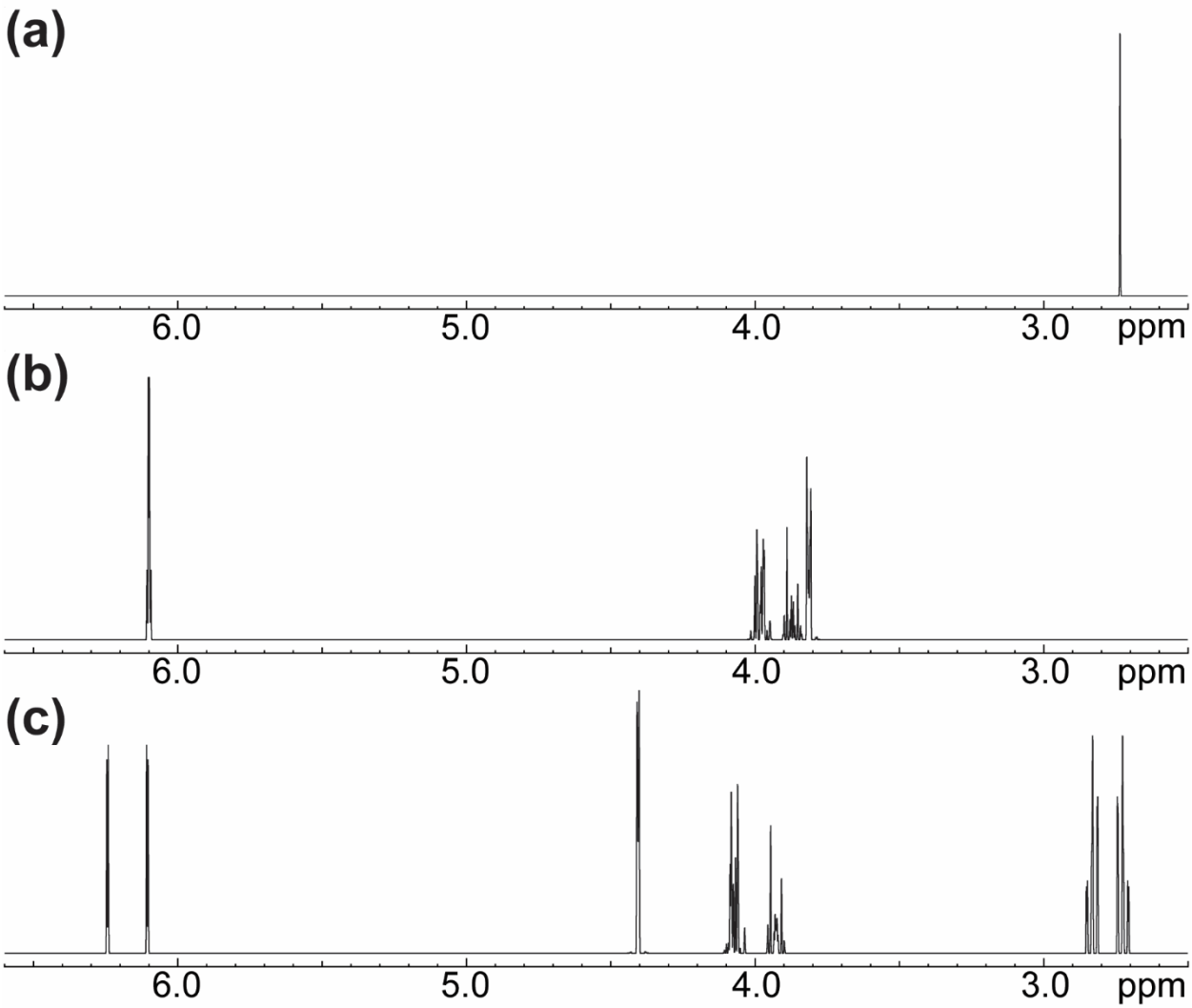

Figure 2.7. Simulated ^{1}H NMR spectra for **(a)** SA, **(b)** monomer **1**, and **(c)** monomer **2**. Each of the simulations was set to 400 MHz, from δ 2.5 – 6.6, a line width of 1 Hz, and 512k points.

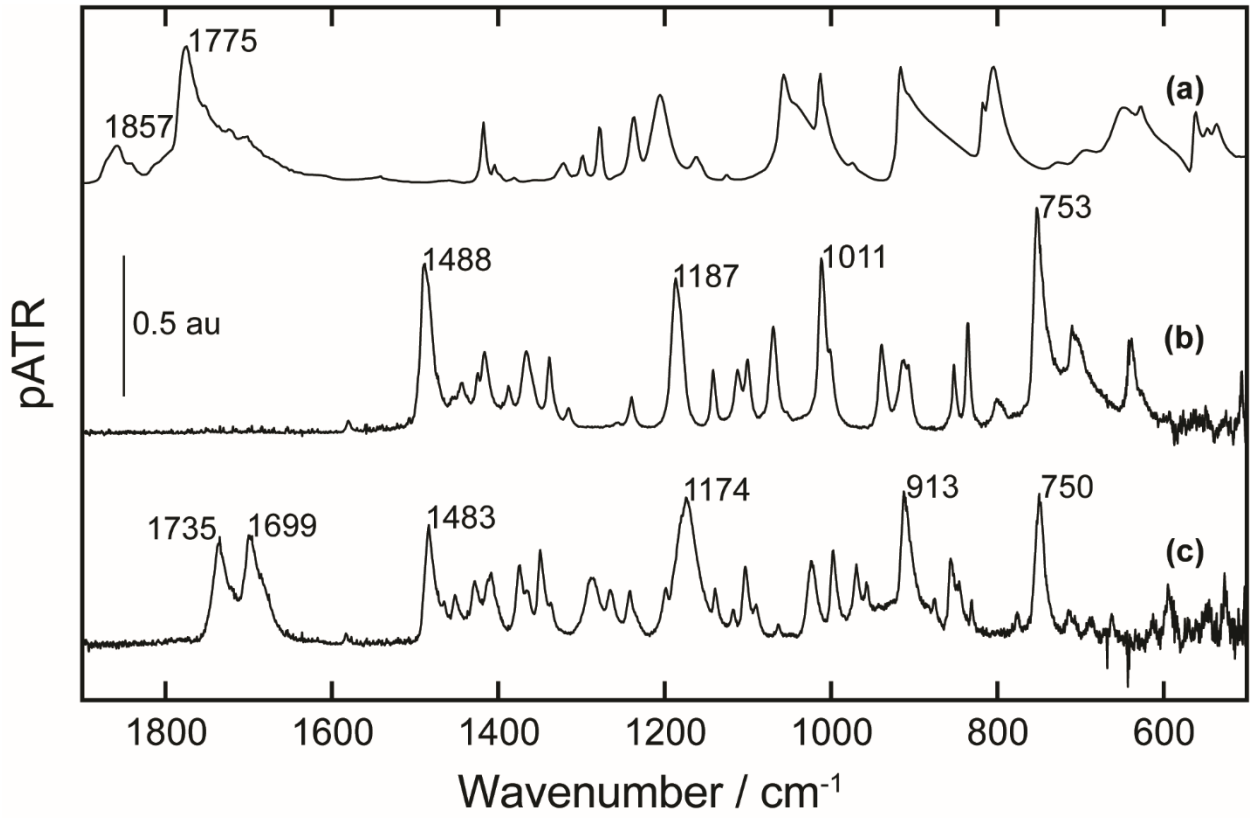

Figure 2.8. Stacked attenuated total reflectance Fourier transform infrared (ATR-FTIR) spectra of **(a)** SA (4 cm^{-1} resolution), **(b)** monomer **1** (0.5 cm^{-1} resolution), and **(c)** monomer **2** (0.5 cm^{-1} resolution).

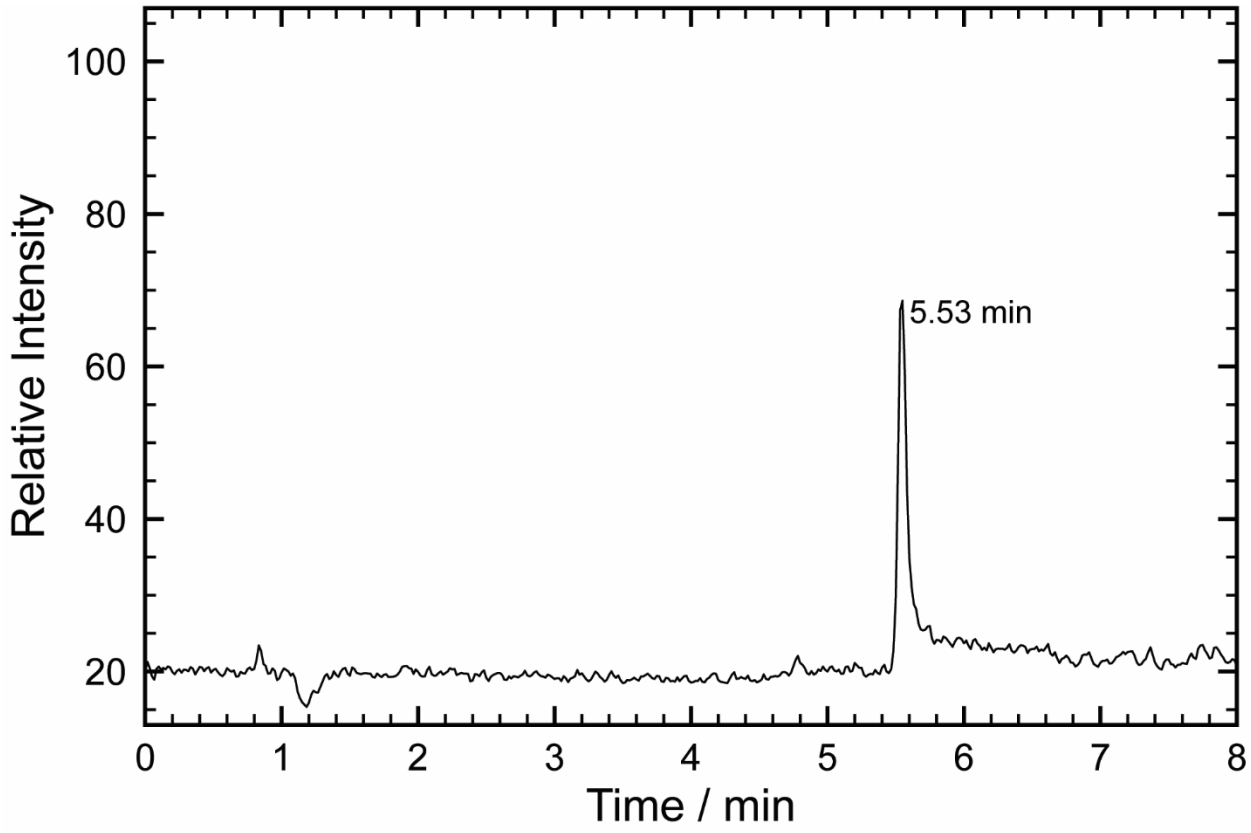

Figure 2.9. Total ion chromatogram for monomer **1**.

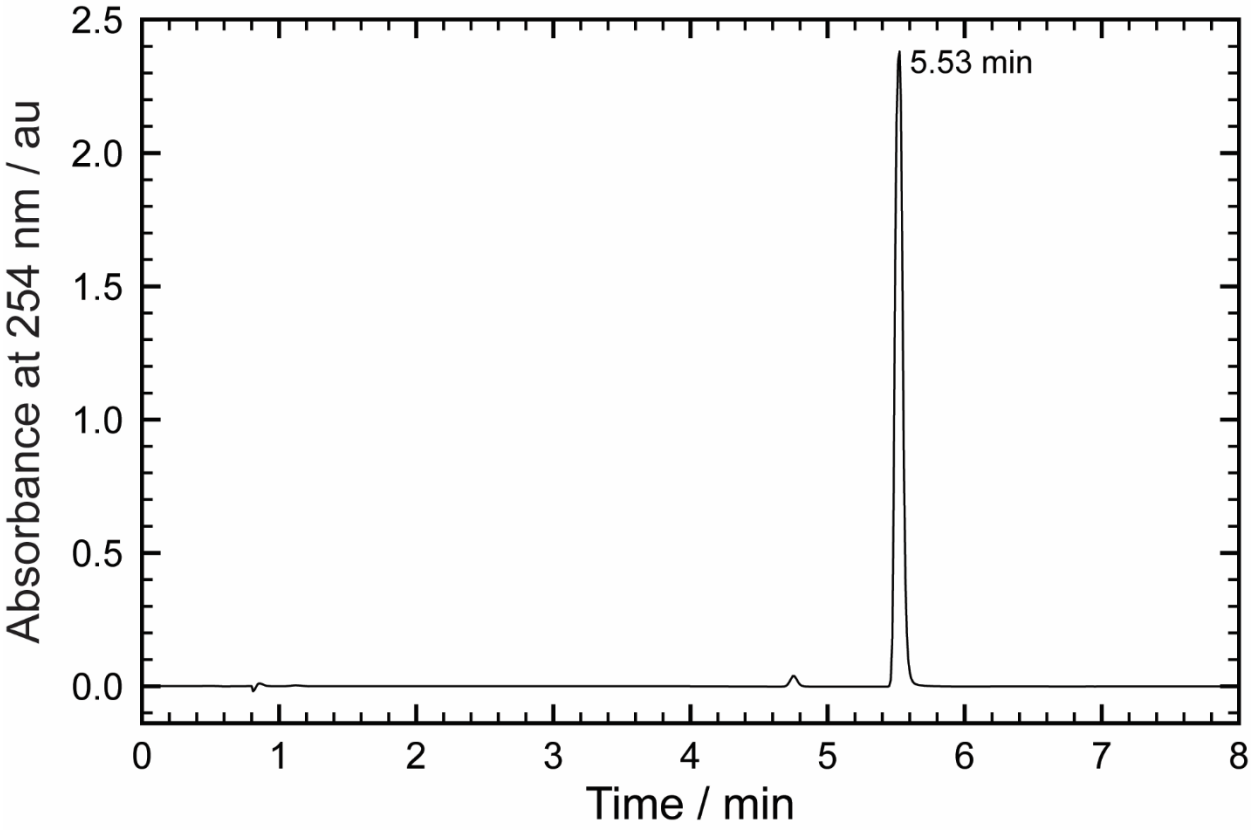

Figure 2.10. The liquid chromatogram of monomer **1**.

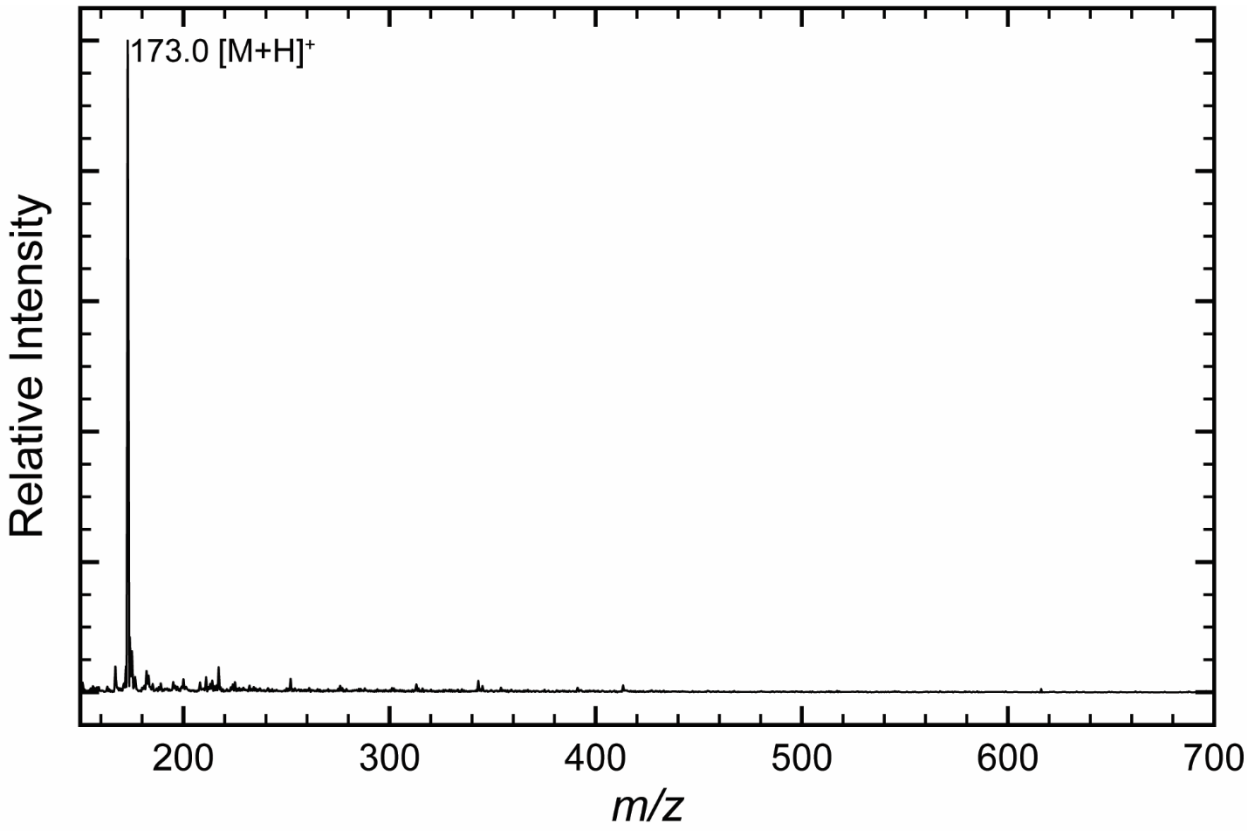

Figure 2.11. The mass spectrum of the peak at 5.53 min in the chromatogram of Figure 2.10. The base peak of the spectrum corresponds to the calculated protonated monomer **1** (*m/z* 173.0).

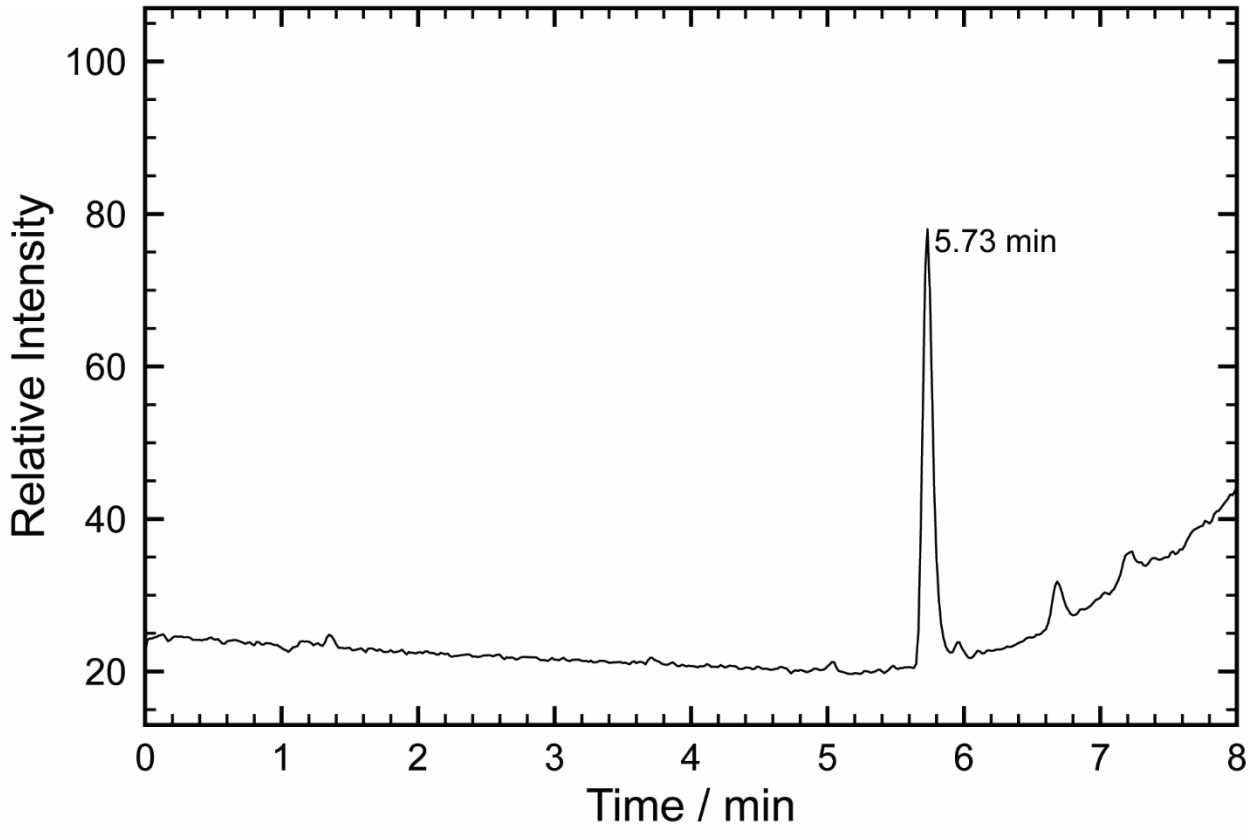

Figure 2.12. Total ion chromatogram of monomer **2**.

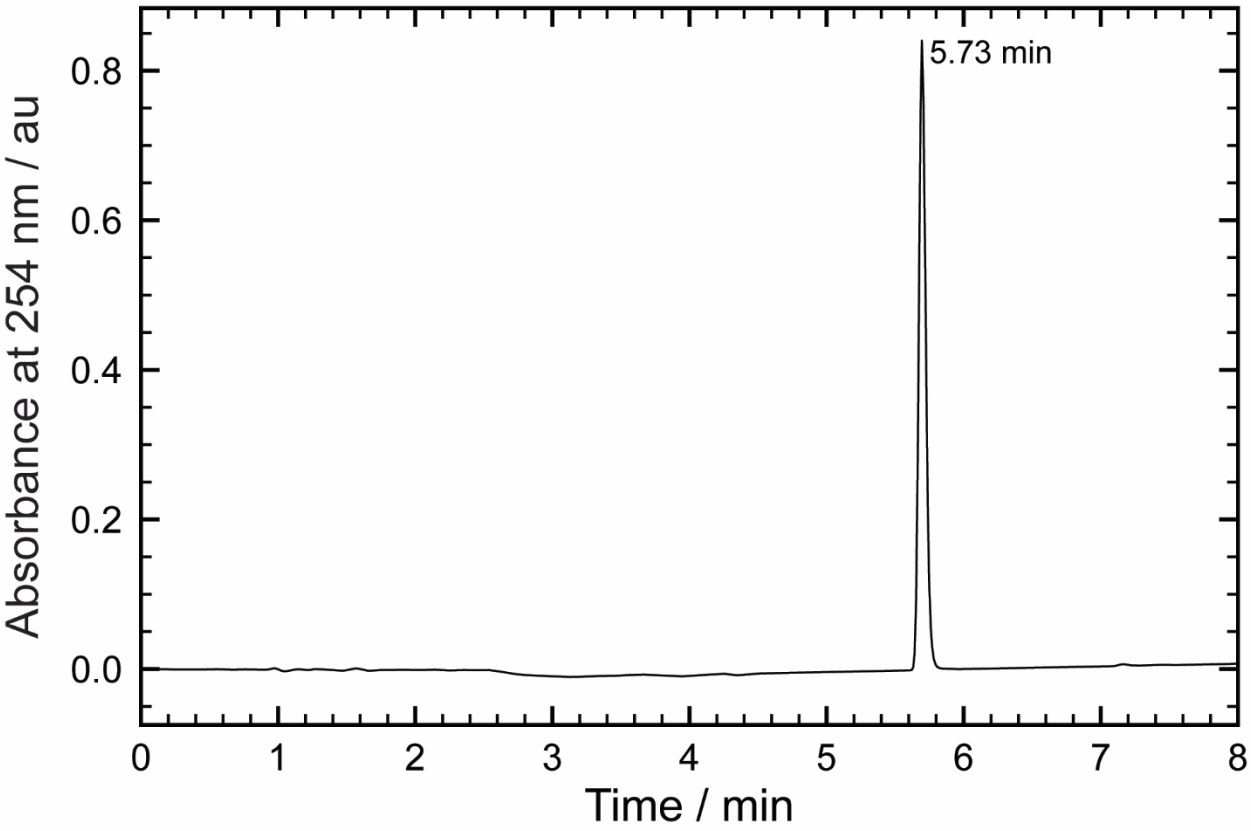

Figure 2.13. The liquid chromatogram of monomer **2**.

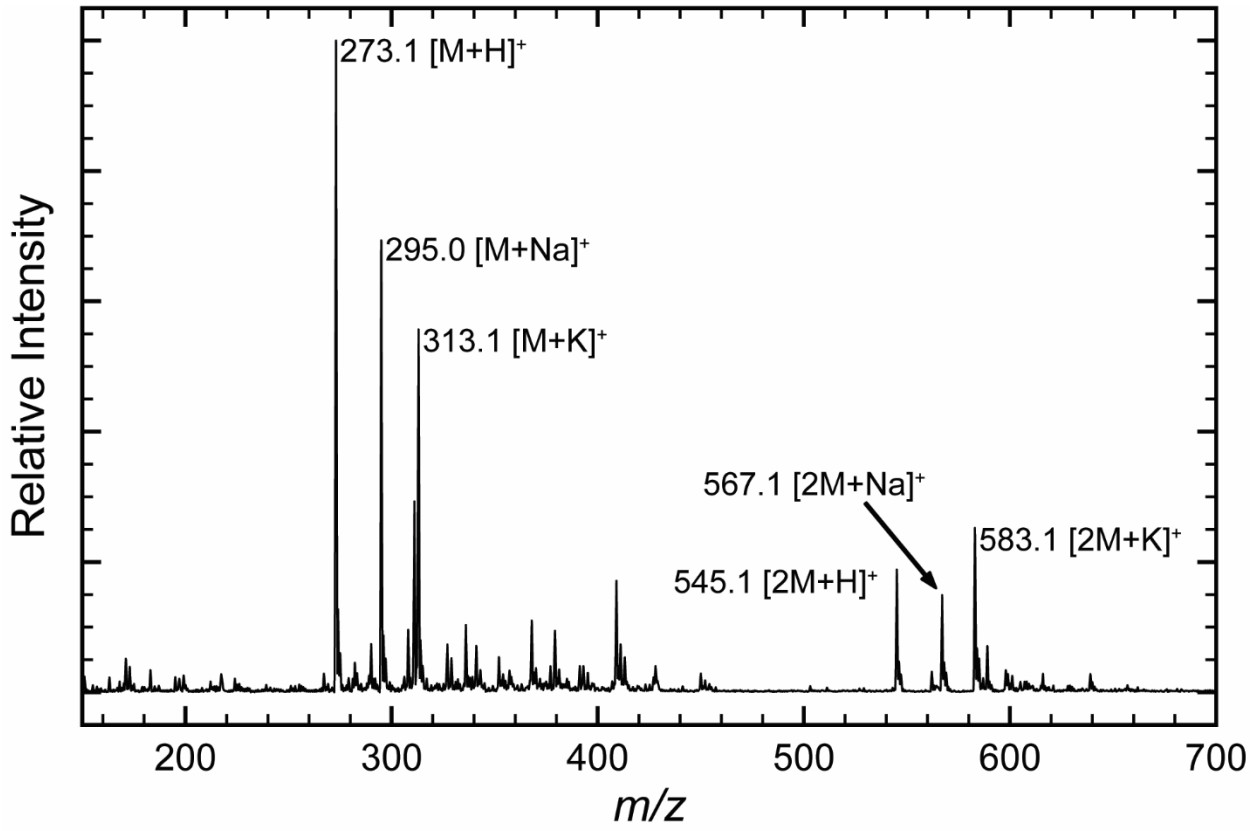

Figure 2.14. The mass spectrum of the peak at 5.73 min in the chromatogram of Figure 2.13. The base peak of the spectrum corresponds to the calculated protonated monomer **2** (*m/z* 273.1). There are a series of additional peaks that are the result of sodiated and potassiated monomers and dimers of **2**.

3. Spatially Directed Functionalization by Co-electropolymerization of Two 3,4-ethylenedioxythiophene Derivatives on Microelectrodes within an Array

Benjamin J. Jones[†], Carol L. Korzeniewski[‡], Jefferson H. Franco[‡‡], Shelley D. Minteer[‡‡], and Ingrid Fritsch[†]*

[†]Department of Chemistry and Biochemistry, University of Arkansas, Fayetteville, AR 72701

[‡]Department of Chemistry and Biochemistry, Texas Tech University, Lubbock, TX 79409

[‡‡]Department of Chemistry, University of Utah, Salt Lake City, UT 84112

3.1 Abstract

Potentiodynamic co-electropolymerization of films in aqueous solutions of thiophene derivatives, (2,3-dihydrothieno[3,4-b]dioxin-2-yl)methanol (**1**) and 4-((2,3-dihydrothieno[3,4-b][1,4]dioxin-2-yl)-methoxy)-4-oxobutanoic acid (**2**), containing 0.02 M total monomer (0, 25, 34, 50, 66, 75, 100 mol% **2)**, 0.05 M sodium dodecyl sulfate, and 0.1 M $LiClO_4$, on gold microband electrodes in an array was investigated. Decreasing monomer deposited (*m)* from 0 to 100 mol% **2** is attributed to a decreasing pH that inhibits electropolymerization. The **2:1** ratio in the films, determined by micro-attenuated total reflectance Fourier transform infrared spectroscopy and X-ray photoelectron spectroscopy, linearly tracks the ratio in the deposition solutions. Capacitances measured from cyclic voltammetry in aqueous buffer and the electron transfer of ferrocyanide at the films are unaffected by comonomer composition, except for the 100 mol% **2** case. The ratios of reverse-to-forward faradaic peak currents at the films suggest that films with high content of **1** expand in the anodic form and contract in the cathodic form and vice versa for films with high content of **2**, where anions and cations dominate counterion transport from solution, respectively. These studies demonstrate capacitance of films that is unimpeded by polymer composition and film formation with predictable numbers of carboxylic acid and hydroxyl functional groups for further modification.

3.2 Introduction

The original driving force behind the development of conducting polymers (CPs) was the need by the electronics industry to have a transparent, thermally stable, vacuum moldable, and intrinsically conductive material as an antistatic coating.[1] Since then their development has grown to many applications including energy storage and environmental remediation,[2] biomedical,[3-10] electrochromic materials,[11] molecular electronics,[12] chemical sensors,[13-16] and electrochemical biosensors.[17-20] This diversity of applications is possible because by changing substituents on the monomers and polymers through organic synthesis, the properties can be altered.

Polythiophenes (PTs) are a unique subset of intrinsic CPs due to their ability to be electrochemically generated, stable in undoped states, mechanically stable, and possible structural modification giving way to new and advantageous chemical characteristics.[21, 22] The electrochemical generation of PTs is strongly dependent upon solvent, electrolyte, electrochemical technique used, electrode material and geometry, and local environment (temperature and atmosphere).[23] PTs have been applied most extensively in amperometric sensing,[24-26] optoelectronics,[27, 28] and energy storage.[29]

To maintain linear polymerization, high conductivity, and stability, researchers at Bayer AG in the mid to late 1980s developed the monomer 3,4-ethylenedioxythiophene (EDOT), (Figure 3.1) to form poly(3,4-ethylenedioxythiophene) (PEDOT) upon chemical or electrochemical oxidation. Initial insolubility in aqueous conditions was overcome by pairing with the polyelectrolyte poly(styrenesulfonate) (PSS) as the counterion. This resulted in very stable and conductive films in an aqueous environment. The stable and transparent (in the oxidized state) polymer was initially used as an antistatic coating for photographic film. Aqueous

polymerization of PEDOT can be accomplished using a microemulsion technique by adding a solubilizer, such as sodium dodecyl sulfate (SDS) or beta-cyclodextrin, sulfated sodium (β-CDSS), to aqueous solutions to dissolve the insoluble monomer.[1, 30-32]

Due to the success of PEDOT, researchers set out to develop synthetic routes to further functionalize EDOT to expand its chemical properties.[1, 33] However, direct functionalization of EDOT is not possible and therefore a new EDOT derivative was synthesized with a hydroxymethyl group, (2,3-dihydrothieno[3,4-b]dioxin-2-yl)methanol (**1**) (Figure 3.1).[34, 35] The addition of the hydroxymethyl group improves solubility in aqueous solutions, does not interfere with the conductivity along the polymer backbone, does not shift the oxidation potential much from that of EDOT, and allows for further functionalization. Due to these advantages, it has become commercially available.[36]

During the research and development of CPs in general, two rules of thumb emerged: a spacer group was needed between the π-conjugated backbone and the desired functional group, and any functional group used should not be oxidized at potentials lower than the monomer itself. These rules serve to avoid disruptions in conductivity, steric effects that could inhibit successful polymerization, and undesired oxidation of the functional group rather than the desired polymer formation.[35] Carboxylic acid functional groups tethered to EDOT are desirable because of their known reactivity, established conjugation protocols and have been synthesized.[37] These derivatives have been used in DNA detection,[38] cell engineering and capturing,[9, 39] glucose sensing,[40] nanomaterial synthesis,[41] surface engineering,[42, 43] and chemical sensing.[44]

An early EDOT carboxylic acid derivative was first synthesized and separated by Mouffouk, 4-((2,3-dihydrothieno[3,4-b][1,4]dioxin-2-yl)-methoxy)-4-oxobutanoic acid (**2**)

(Figure 3.1).[45] A copolymer film of monomer **2** and EDOT, at a 1:6 molar ratio, was electropolymerized on a 10 µm platinum disk in non-aqueous conditions. The resulting film was then transferred to aqueous media and used for oligonucleotide detection. Ali published an alternative and straight forward synthesis of the carboxylic acid derivative and quantified the conductivity shift of the resulting polymer based on the pH of aqueous buffers.[36] A majority of the work involved single monomer films[46] or copolymers with EDOT. Luo electropolymerized this carboxylic acid derivative, along with others of differing spacers between the EDOT monomer base structure and the carboxylic acid functional group for use as a biocompatible nanointerface.[10] Bhagwat conducted similar work and used the resulting copolymer films to immobilize peptides toward biocompatible neural electrodes.[47, 48]

Considerable effort has been given to the combination of different derivatives of EDOT to generate CPs with a wider variety of properties. A stable copolymer of ferrocene derivatized EDOT was formed electrochemically with hexaethylene glycol bis((2,3-dihydrothieno[3,4-b][1,4]dioxin-2-methyl) ether in nitrobenzene under potentiostatic conditions.[49] Valuable conditions were realized during this work such as the selection of a proper solvent for full incorporation of both monomers into the copolymer and choosing substituents with appropriate redox conditions such that it does not interfere with the oxidative polymerization along the conjugated thiophene backbone. In another work, aqueous microemulsions, generated by the addition of 0.1 M SDS, were used to copolymerize **1** with other derivatives. Both electrochemical and chemical oxidative polymerizations were performed on selected monomers to generate ultra-smooth copolymers with low cytotoxicity as a platform for biosensors.[50] The wettability of copolymer surfaces was found to be switchable by adjusting both pH and the applied voltage by Darmanin et al. when they co-electropolymerized two derivatives of

monomer **1**. One monomer contained a carboxylic acid and the other a dodecyl group, and the two were electropolymerized at various molar ratios (0.1 M total monomer concentration), in dry acetonitrile, under potentiostatic conditions. Immediately after electropolymerization all copolymers were found to be superhydrophobic, but upon electrochemical reduction, the copolymers with molar ratios between 25 – 75 mol% **2** of the carboxylic acid monomer in the deposition solution, were found to have switched to being hydrophilic (contact angle < 90˚). They also demonstrated reproducible reversibility after repeated electrochemical and chemical treatments of the copolymers.[51] Despite these two examples, and many others not discussed here, demonstrating an effective change of copolymers' overall properties by varying substituent functional groups, there has been less consideration given to quantifying and comparing the relative amount of each respective monomer in the copolymer film compared to that in the deposition solution.

A quantitative assessment of the molar ratios between monomers in a formed copolymer compared to that in the solution from which they were deposited is of interest to further adjust and vary properties of resulting films. Doherty et al. used spectroelectrochemistry to determine relative reactivity ratios of the copolymers of EDOT and monomer **1** based on their concentration in the deposition solution and their measured molar absorptivity. They were able to calculate significantly different reactivity ratios for the monomers and thus demonstrate that monomer **1** was preferentially incorporated in the copolymer despite the fact that the solution ratio being 50:50 between the two monomers.[52] A following paper by researchers of the same group found that for copolymers of monomer **1** and 6-(2,3-dihydrothieno[3,4-b]-1,4-dioxin-2-yl methoxy)hexanoic acid (a derivative of monomer **1** with a 5 carbon chain terminated by a carboxylic acid) deposited in acetonitrile at a 50:50 molar ratio incorporated more of the acidic

derivative into the copolymer.[53] They followed monomer concentrations in solution both before and after copolymerization. They also used X-ray photoelectron spectroscopy (XPS) and Fourier transform infrared (FTIR) spectroscopy of the films for further characterization.[54] There are some details to note regarding their reported interactions of monomers during electrochemical copolymerization and how the resulting copolymer compositions compare to the monomer compositions in solution. The first is that the electropolymerization was carried out in polar solvents (acetonitrile and a 10% v/v aqueous methanol) without the addition of surfactants. The second is that depletion studies of the monomers after polymerization required low concentrations of monomers (1×10^{-3} – 5×10^{-5} M) to be deposited on large electrodes (12.9 – 0.78 cm^2).

Herein we report the co-electropolymerization of monomers **1** and **2** from aqueous solutions containing a solubilizer at various molar ratios, while maintaining a total monomer concentration of 0.02 M, on microband electrodes in arrays by cyclic voltammetry (CV). Unlike prior studies of co-electropolymerization of EDOT and its derivatives, ours were performed in aqueous solutions with SDS as a solubilizer. Also, the microelectrodes allow for deposition without affecting the bulk concentration. The overall electropolymerization strategy is shown in Figure 3.2. Microelectrodes were characterized electrochemically before and after electropolymerization in supporting electrolyte and solutions containing a faradaic model compound to measure their charging and electron transfer responses. For each deposition solution, the monomer oxidation onset potential (Eonset), the total charge passed, and the amount of monomer deposited were determined. Film densities were estimated from average cross-sectional areas measured by profilometry. The techniques of XPS and micro-attenuated total reflectance FTIR (μATR-FTIR) spectroscopy were used to determine the amount of each

monomer incorporated into the copolymer films for comparison to the molar ratios of monomer in the depositon solutions.

3.3 Experimental

3.3.1 Chemicals and materials. All chemicals were reagent grade and used as received unless otherwise specified. The microelectrode arrays were fabricated by standard photolithographic methods on silicon wafers (125 mm diameter, 600 – 650 µm thick, with a 2 µm layer of thermally grown oxide on the surface) acquired from Silicon Quest International (Santa Clara, CA, USA). A chromium-plated tungsten rod, gold coin (Canadian Maple Leaf, 99.99%), and molybdenum boat (Kurt J. Leskar Company, Clairton, PA, USA) were used for thermal vapor deposition of metals using an Auto 306 (BOC Edwards, West Sussex, UK). Positive photoresist (AZ 4330) and developer (AZ400K) were procured from EMD Performance Materials (Somerville, NJ, USA). Gold etchant (GE8148) was purchased from Transene (Danvers, MA, USA) and chromium etchant CEP-200 was obtained from Microchrome Technology (San Jose, CA, USA). Cyclotene 4024-40 (benzenecyclobutene, BCB), adhesion promoter (AP3000), and developer (DS2100) were used to insulate the chip-based electrode leads and were obtained from Dow Corning Company (Midland, MI, USA). Photoplot masks for metal and insulating layers were purchased from Fine Line Imaging (Colorado Springs, CO, USA). Electrical connection between the chip and potentiostat was made using an edge connector (solder contact, 20/40 position, 0.5 in pitch) from Sullins Electronics Corporation (San Marcos, CA, USA). The chip was kept in contact with the edge connector using a 0.99 mm thick folded plastic shim. Aqueous solutions were prepared using ACS reagent grade water, ASTM Type I, ASTM Type II (H_2O) from RICCA Chemical Company (Arlington, TX, USA). Succinic anhydride (SA), 4-(dimethylamino)pyridine (DMAP), triethylamine (Et_3N), sodium phosphate

dibasic anhydrous, sodium phosphate monobasic anhydrous, and **1** were purchased from Sigma-Aldrich (St. Louis, MO, USA). Sodium dodecyl sulfate (SDS), potassium ferrocyanide trihydrate ($K_4Fe(CN)_6 \bullet 3H_2O$), and lithium perchlorate ($LiClO_4$) were obtained from Amresco (Solon, OH, USA), J.T. Baker (Phillipsburg, NJ, USA), and Alfa Aesar (Tewksbury, MA, USA), respectively. Concentrated hydrochloric acid (HCl), dichloromethane (DCM), and alumina (Neutral, Brockman Activity I) were purchased from Fisher Scientific (Pittsburg, PA, USA). Sodium chloride (NaCl), magnesium sulfate ($MgSO_4$), and acetonitrile (MeCN) were acquired from EMD Chemicals (Billerica, MA, USA). Deuterated chloroform ($CDCl_3$) was purchased from Cambridge Isotopes Labs (Tewksbury, MA, USA).

3.3.2 Chip design and microelectrode array fabrication. Figure 3.3 shows design schematics and a fabricated example of the electrode array chip. It is 2.54 cm × 2.54 cm in outer dimensions and has 20 individually-addressable electrodes, 16 of which are microband electrodes within an array. The nominal geometric area of each microelectrode is 2×10^{-3} cm^2 (2000 µm × 100 µm), and each one is separated from its neighboring electrode(s) by a 100 µm gap. The length of each microelectrode is defined by the edges of the insulating BCB layer.

The chip fabrication procedure has been detailed in previously published work.[55] The following describes slight modifications to the procedure and chip design. The silicon wafers were cleaned of organic residue and particles using the first step (SC-1) of the procedure developed by the Radio Corporation of America (RCA, New York, NY, USA).[56] A 10 nm thick adhesion layer of chromium was deposited by thermal evaporation onto the silicon wafers, followed by a 250 nm thick layer of gold without breaking vacuum. A spin-rinse-dry cycle was performed on the wafers, followed by a dehydration bake at 150 ˚C for 30 min. Then, a 2.8-µm thick layer of positive photoresist was spin-coated onto the wafers to define the electrode

features from the photoplot mask. A soft bake at 90 ˚C for 120 s was performed and followed by a second bake at 40 ˚C for 30 s to remove residual solvent directly before exposure. Immediately following exposure through the mask, the resist was developed by immersing in AZ400K for 120 s and both gold and chromium were etched. The protective layer of the resist was then exposed and developed in the same manner described above. A small amount of AP3000 was applied to the wafers before a 7.4 µm thick layer of BCB was spin-coated onto the wafers. This was followed by a soft bake at 80 ˚C for 90 s followed by an additional bake at 45 ˚C for 30 s. The BCB was then exposed, developed, and soft baked at 90 ˚C for 60 s and then at 45 ˚C for 30 s. A hard cure of the BCB was performed under N_2 at 250 ˚C for 60 min. Then, trace resist remaining on the wafers was removed by reactive ion etching (SLR 720, PlasmaTherm, St. Petersburg, FL, USA) using an etch recipe of 32 sccm and 8 sccm of O_2 and SF_6, respectively, at 250 mtorr and 200 W for 30 s followed by a stability step of the same gasses, flow rates, and pressure, but at 0 W for 10 s. The wafers were then cut using a dicing saw (K&S 982-10, Kulicke & Soffa Industries, Singapore) to produce the individual chips.

3.3.3 Synthesis and characterization of monomer 2. SA was used to derivatize monomer **1** with the desired terminal carboxylic acid group to form monomer **2** based on a previously reported procedure.[36] DCM was dried over alumina before use. Briefly, 452.7 mg of monomer **1** was dissolved in 25 mL DCM by stirring in a three-neck round-bottom reaction flask under N_2. A mixture of 562.7 mg SA, 28.6 mg DMAP, and 0.527 mL Et_3N was prepared in 10 mL DCM and stirred for 1 h at room temperature to dissolve, then added dropwise to the reaction flask. The reaction was stirred under N_2 overnight. The product was extracted with 10% HCl and rinsed with a saturated NaCl solution until the discarded rinse was the same pH as the saturated NaCl solution. The product was dried over $MgSO_4$ and remaining solvent evaporated under

vacuum to yield monomer **2** (669.9 mg, 93.6% yield). To ensure the reaction was successful, characterization of the product, as well as the starting materials, by proton nuclear magnetic resonance spectrometry (^{1}H NMR), attenuated total reflectance Fourier transform infrared spectrometry (ATR-FTIR), and liquid chromatography coupled to electrospray ionization and mass spectrometry (LC-ESI-MS).

^{1}H NMR (400 MHz, $CDCl_3$): δ 6.37 (2 H, dd, *J* = 3.6, 3.6 Hz), 4.06 (1 H, dd, *J* = 11.7, 6.9 Hz), 4.24 (2 H, dd, *J* = 11.7, 1.9 Hz), 4.30 – 4.44 (3 H, m), 2.66 – 2.78 (4 H, m). ATR-FTIR (cm^{-1}): 1735 ($\nu C{=}O_{ester}$), 1699 ($\nu C{=}O_{carboxylic\ acid}$), 1483 (combination of stretching and bending modes of the C=C, C-C, and C-H bonds of thiophene ring), 1174 ($\nu C\text{-}O\text{-}C_{ring}$, $\nu C{=}C_{thiophene}$), 913 ($\nu C\text{-}S\text{-}C_{thiophene}$), 750 ($\delta$ C-$H_{thiophene}$). LC-ESI-MS (*m/z*): $[M+H]^+$ calcd for $C_{11}H_{12}O_6S$, 273.043, found 273.1. The ^{1}H NMR, ATR-FTIR, and LC-ESI-MS results of the starting materials and products can be found in the Supporting Information, Figures 3S-1 - 3S-7.

3.3.4 Electrochemical studies. A three-electrode electrochemical cell, platinum flag or wire counter electrode, Ag/AgCl (saturated KCl) reference electrode, CHI 650A with a picoamp booster and faraday cage (CH Instruments, Austin, TX, USA) were used for all electrochemical procedures. Before the chips were used for any electrochemistry (initial characterization and electropolymerization of films) they were rinsed with H_2O, dried with Ar, and cleaned of residual trace organics by oxygen plasma (6.8 W applied to RF coil for 15 min at 60 mtorr, PDC-32G, Harrick Plasma, Ithaca, NY, USA) and stored in H_2O until use.

A 0.2 M sodium phosphate buffer, pH 6.5, was prepared by first dissolving 14.24 g sodium phosphate dibasic anhydrous in a 0.5 L H_2O volumetric flask. Then 12.04 g sodium phosphate monobasic anhydrous was dissolved in 0.5 L H_2O in another volumetric flask. The pH of the sodium phosphate dibasic solution was continuously monitored while enough of the

sodium phosphate monobasic solution was added to adjust the pH to 6.5. Electrodes were characterized before (designated as bare gold) and after electropolymerization of films by CV in two solutions: a 0.2 M sodium phosphate buffer, pH 6.5, and the buffer containing 0.001 M $K_4Fe(CN)_6$. Area-normalized capacitance, *C*, of each electrode was determined from the charging current, i_c, measured from the CV response both before and after film modification, using Equation 1,

$$C = \frac{i_c}{vA} \quad [1]$$

where *v* is the scan rate of the cycle and *A* is the geometric area of the electrode (metal thickness was assumed to be a negligible contribution to A). Electrodes were swept from -0.1 - +0.700 V to avoid the risk of oxidizing the gold and over-oxidizing the polymer films. The i_c of the CV response in the buffer alone was obtained by dividing the current difference between the forward and reverse sweeps at +0.400 V by two. The i_c for the buffer containing $Fe(CN)_6^{4-}$ was measured directly from the forward sweep current at 0.000 V to avoid contributions from faradaic current in the return sweep.

To ensure that enough monomer **2** was available for the full set of depositions, a cell (Figure 3.4) was designed such that only 0.7 mL was needed and placement of the reference and counter electrodes could be controlled for each deposition. The cell was machined from Delrin® and has two main parts: the bottom bulk of the cell, where mounts for the edge connector and the solution well are located, and the top of the cell, which holds the counter and reference electrodes in place. The top is fixed to the bottom by machine screws. For all electrochemical procedures other than polymer depositions, a small 15 mL glass cell was used.

3.3.5 Electropolymerization of films. Films were electropolymerized from aqueous solutions containing 0.1 M $LiClO_4$, 0.05 M SDS and a total monomer concentration of 0.02 M.

For electropolymerization by CV, the working electrode was cycled from -0.100 to +1.20 V at a scan rate of 0.1 V s^{-1} for a total of three cycles, with a 2 s quiet time at -0.100 V between each cycle. Each polymer was generated in triplicate by modifying three microband electrodes within the same array on a given chip; each chip was dedicated to a specific mol% **2** of the two monomers. In cases of inadequate polymer adhesion, the surfaces of the working electrodes were refreshed by swabbing the array first with 1 M sodium hydroxide, followed by rinses of ethanol and H_2O, and finally dried with Ar. Once the depositions were concluded for a given chip, it was carefully removed from the cell and placed in another cell containing the sodium phosphate buffer for 5 min. Five sequential CV cycles were then performed from -0.100 to +0.700 V at a scan rate of 0.050 V s^{-1} to stabilize the electrodeposited polymer, one modified electrode at a time. The chips were subsequently stored under H_2O overnight before further characterization. The capacitance of each film was measured and characterized with an electroactive model compound in the same manner as described for electrodes before modification.

3.3.6 Determination of E_{onset}. Because there are no resolved oxidation peaks during the electrodeposition cycles, a reproducible method was developed to determine E_{onset} when monomer oxidation becomes visibly significant over the charging current during the electropolymerization cycles. The average background current, between 0.000 and +0.500 V, was determined and subtracted for each electrodeposition cycle. Then the first derivative was approximated using the software accompanying the CHI 650A. The local minimum of the first derivative plot corresponding to the inflection point was used to extrapolate a tangent line, with proper slope and position, to locate the potential value at zero current of the deposition voltammogram. The process was only performed for the anodic sweep of each deposition cycle

and average values with standard deviation are listed in Table 3.1. Further detail can be found in the Supporting Information and a schematic of this process is shown in Figure 3S-8.

3.3.7 Determination of Q_T and m for electrodeposited films. The total charge passed (Q_T) and total monomer deposited (m) were determined from the electrodeposition voltammograms. Each deposition cycle was separated into forward and reverse sweeps and the average background current, for each sweep, was determined and subtracted as described earlier. The area of the curve to background-subtracted zero current was integrated for both segments of each cycle and added. Because the anodic current is defined as negative in this work, the absolute value was the amount of charge passed for that cycle. The process was repeated for the subsequent cycles and the sum of the charge passed for each of the cycles is Q_T, and given by Equation 2,

$$Q_T = Q_1 + Q_2 + Q_3 \quad [2]$$

where Q_1, Q_2, and Q_3 are the average charge passed for the first, second, and third deposition cycles, respectively, across the modified electrodes of a given mol% **2**. The values of Q_T, with standard deviation, for each of the seven different films, are listed in Table 1. The total number of moles that were electrodeposited, m, was calculated directly from Q_T, using Equation 3,

$$m = \frac{Q_T}{nF} \quad [3]$$

where n is the number of electrons per monomer deposited, assumed to be 2.3,[37] and F is the Faraday constant. These values are reported in Table 3.1. See Supporting Information for more detail.

3.3.8 Profilometry. Profilometry of each film was carried out on a Dektak 3030 surface profiling measuring system (Sloan Technology Corporation, Santa Barbra, CA, USA). Each

array was scanned with a medium speed and stylus force setting of 20 mg, which correlates to a force of 0.2 mN. To ensure a representative average of the films' profile, each electrode was scanned across its width three times: once near each of the two ends of the microband and once in the middle, about halfway between the two ends. The printout of each measurement was scanned as digital images and digitized with GetData Graph Digitizer software (www.getdata-graph-digitizer.com) to generate tabulated data for analysis. A line was drawn from the base of one side to the base on other of each electrode profile, above which the cross-sectional area was determined. To obtain the average cross-sectional area of a given type of film, the average cross-sectional area of the unmodified electrodes on the same chip was subtracted from the average cross-sectional area of the modified electrodes. For the chip with the 0 mol% **2** films, the measurement was completed using six scans, instead of three, because of larger distances between modified electrodes. Also, difficulty obtaining a suitable background resulted in only two 0 mol% **2** modified electrodes were used in the final calculation of the average cross-sectional area. A schematic showing the order and direction of measurements is shown in Figure 3S-9 of the Supporting Information.

3.3.9 Characterization by μATR-FTIR. The composition of the modified microelectrodes was analyzed by μATR-FTIR sampling using a Vertex 70v FTIR spectrometer equipped with a HYPERION 2000 infrared microscope (Bruker Optics, Billerica, MA, USA). The spectrometer bench was mainteined under vacuum, and radiation from the interferometer was passed to the microscope through a KBr window. The microscope was kept under a dry N_2 gas purge and secured to the spectrometer bench through a purge tube. All samples dried under ambient conditions before analysis. Electrodeposited polymer on the 100 μm wide microelectrodes was analyzed using the diamond ATR probe (32 μm diameter) on the

microscope objective (20×, 0.6 NA). The probe sampled within the center region of each electrode. The knife-edge apertures on the microscope were set to isolate the electrode and ensure against sampling regions on the chip beyond the electrode of interest. The probe-electrode force was adjusted as recommended for polymers (~ 0.5 N). The microscope was operated with a mid-range liquid nitrogen cooled mercury-cadmium-telluride (MCT) detector. Immediately prior to measurements on the modified electrodes, the ATR crystal was cleaned by gently passing ethanol-soaked lens tissue over the probe surface, and a background spectrum was collected with the probe suspended in air. All interferograms were recorded at 4 cm^{-1} resolution with 64 scans averaged and processed using the Blackman-Harris three-term apodization function before Fourier transformation. Spectra are displayed in units of pATR,

$$pATR = -\log \frac{I_{sample}}{I_{background}} \quad [4]$$

where I_{sample} and $I_{background}$ represent the sample and background single beam spectra, respectively.

3.3.10 Characterization by XPS. XPS measurements were carried out on a Kratos Axis Ultra DLD spectrometer (Kratos Analytical Ltd., Manchester, UK) using a monochromated aluminum source (Al Kα 1486.6 eV). An X-ray gun with an emission current of 0.01 A, anode voltage of 15 kV, and a bias voltage of 125 V was used. The aperture size and iris position were both 110 µm centered on the 100 µm wide modified microelectrodes. High-resolution scans of the C(1s) core electrons were obtained using a pass energy of 40 eV and step size of 0.1 eV. Copper tape was used to short the contact pads of the chip and ground it to the sample stage. A charge neutralizer gun was used to compensate for any charge accumulation during the measurement. All XPS data were analyzed, deconvoluted, and fitted using CasaXPS software (Casa Software, Ltd., Teignmouth, UK). A linear background and line shapes of a Gaussian-

Lorentzian sum form were used. Constraints were forced on the peak area, full-width at half maximum (FWHM), and binding energy position of the synthetic components. A more detailed explanation of the deconvolution and fitting process can be found in the Supporting Information.

3.4 Results and Discussion

3.4.1 Electropolymerization of monomers. Electropolymerization was performed from aqueous solutions containing 0.05 M SDS, 0.1 M $LiClO_4$, and monomers **1** and (or) **2** at a total concentration of 0.02 M. The mol% **2** represents the molar ratio of monomer **2** to all monomers in the deposition solution, given by Equation 5.

$$mol\% = \left[\frac{mol\ \mathbf{2}}{mol\ \mathbf{1}+mol\ \mathbf{2}}\right] \times 100\% \quad [5]$$

Figures 3.5a through 3.5g present the electropolymerization voltammograms obtained at 0.1 V s^{-1} for each mol% **2**. Each of the three consecutive cycles (1^{st}, 2^{nd}, 3^{rd}) in the figures is the average current response for that cycle number from three electrodes. Error bars that represent one standard deviation are reported at ten selected potentials in both the forward and reverse sweeps. In all but one case (100 mol% **2**), the average voltammograms were from a single set of electrodes (N=3). The 100 mol% **2** results are from two sets of electrodes (N=6). Figure 3.3c shows an optical microscopy image of an array with polymer films on three electrodes, after the three cycles of deposition from the 50 mol% **2** solution. The films change color from dark blue or purple to colorless, as they transition from reduced to oxidized states. Additional color is caused by the diffraction of white light that varies with film thickness. All deposition voltammograms are shown in Figure 3S-10, and optical microscopy images for all films are shown in Figure 3S-11 in the Supporting Information. The general shapes of the CV responses for electrodeposition from pure and comonomer solutions are similar to each other and consistent with those reported previously for EDOT and other derivatives.[36, 45, 57-59] They exhibit a

characteristic relatively constant charging current between -0.100 V and 0.850 V and a significant increase in anodic current at potentials more positive than 0.850 V where polymer formation occurs.

A more detailed analysis of each CV cycle is given here to investigate possible differences induced by the two monomers and their mixtures. During the first, forward anodic sweep (red) for all monomer solution compositions, the current remains relatively constant due to double-layer charging at the bare gold surface until the potential nears +0.9 V. Beyond +0.9 V, the anodic current increases dramatically due to the oxidation of the monomers in solution that subsequently form polymer films on the electrode. Monomer oxidation and polymer deposition continue during the reverse sweep past +0.9 V because of the lower oxidation potentials of longer oligomers that were not present in solution during the initial anodic sweep. This hysteresis in the first electrodeposition voltammogram is characteristic in solutions of all monomer compositions studied herein. Figure 3S-12 in the Supporting Information can be used to explain this behavior for monomers **1** and **2**. It shows an electropolymerization mechanism modeled from the "oligomer approach" described in the literature for thiophene and pyrrole.[60] The mechanism highlights the difference between initial monomer oxidation and deposition of larger chain, insoluble oligomers, on the electrode surface. The first step is the oxidation of two monomers at the electrode surface resulting in monomeric radical cations. These remain in solution and react with each other forming a dimer in the diffusion layer. The first dimerization between two monomers, during the first anodic sweep, occurs at a larger E_{onset} than subsequent dimerization steps throughout the mechanism. The following steps include successive dimerization reactions at decreasing overpotentials leading to the formation of an octamer. The

decreasing solubility of increased oligomer length leads to the deposition of the polymers on the electrode surface through instantaneous nucleation and 3D polymer growth.

Although the shapes of the deposition voltammograms in Figure 3.5 are similar, a comparison of the anodic sweeps for each mol% **2** reveal different E_{onset} values of monomer oxidation and are listed in Table 3.1. For all three deposition cycles, the 100 mol% **2** E_{onset} values are greater than those for the 0 mol% **2**. The values for the first cycle differ by 0.08 ± 0.02 V. The lowest E_{onset} value for the 100 mol% **2** (Cycle 3, 0.969 ± 0.004 V) is greater than the highest E_{onset} value for the 0 mol% **2** (Cycle 1, 0.946 ± 0.003 V). These results suggest that monomer **1** is easier to oxidize than monomer **2** at the electrode. Because the anodic sweep of the first cycle is primarily the oxidation of the monomers to their radical cations at a bare gold electrode, the difference in oxidation potentials is most likely due to steric effects. The side chain of monomer **2** introduces a conformational barrier to the electrode surface for oxidation. A similar effect was observed between monomers differing in structure by even just a single hydroxymethyl group, as is the case for EDOT and monomer **1** reported in the literature, albeit at a much smaller difference.[53] The E_{onset} values for the first deposition cycle of the different mixed monomer solutions are different from each other. Still, they do not follow a consistent trend with the relative monomer composition in solution. However, the E_{onset} value does decrease consistently for a given solution composition from cycle 1 to cycle 3.

The fast dimerization rate constant for monomeric radical thiophenes (10^9 M^{-1} s^{-1}) in Figure 3S-12, [60] and observed difference in oxidation overpotentials for solutions of pure monomer studied here (0 mol% **2** and 100 mol% **2**), lead us to speculate that the dimers formed during the initial step most likely consist of one type of monomer, not a combination of the two. We do not attempt an in-depth analysis of the deposition mechanism here beyond the previously

proposed Figure 3S-12. This is because of the complexity of the mixed monomer solutions and the potentiodynamic conditions where the potential passes in and out of the monomer oxidation range as well as between charge states during each deposition cycle.[60]

Evidence for growth of the polymer, layer by layer, from one cycle to the next can be seen in the increasing charging current with each cycle for all monomer solutions. The anodic current due to oxidative electropolymerization of the monomer also increases by a similar amount due to this. This behavior has been observed previously with EDOT and EDOT derivatives.[36, 45, 57]However, for a larger mol% **2** in the deposition solutions, the magnitude of both the maximum anodic and background currents are smaller, suggesting less electropolymerization occurs when monomer **2** is present.

To quantify this observation, integration of the background-subtracted current with respect to time during the oxidative deposition portion of the voltammograms was performed. This yields a charge, *Q*, that is proportional to the amount of monomer deposited. Figure 3.6a shows how the dependence of the total charge, Q_T, added over the three cycles, and averaged from multiple electrodes, varies with the composition of the solution. Figures 3.6b-c illustrate how and where the integration of each voltammogram was performed. As seen in Figure 3.6a Q_T decreases with increasing mol% **2** in the deposition solution. These values can be directly converted to the amount of monomer deposited, *m*, assuming 2.3 moles of electrons per mole of monomer deposited[37] using Equation 2. Each deposition solution resulted in films with unique values of *m*. Although the trend exhibits a relatively weak fit to a linear model ($R^2 = 0.9889$), there is a distinctive dependence of *m* on the mol% **2**. This dependence is most likely a consequence of the decreasing pH of the deposition solution caused by the increasing concentration of monomer **2**. The pH of the deposition solution affects proton elimination, which

is the overall rate limiting step of the electropolymerization mechanism, as the nucleation and growth happen simultaneously (Figure 3S-12). Therefore, the rate of proton elimination and thus the amount of oligomer formation from solutions comprised mostly of the acid, monomer **2,** are expected to be lower than in solutions comprised mostly of monomer **1**.

Table 3.1 shows the measured pH values of each deposition solution, along with a monomer-less solution containing only 0.1 M $LiClO_4$ and 0.05 M SDS. The pH of the solutions decreases from 5.42 to 2.96 as the mol% **2** increases from 0 to 100 mol% **2**. Although a pK_a value for monomer **2** could not be found in the literature, it is likely to be similar to the pK_a value of succinic acid, 4.16.[61] This is because succinic acid is nearly identical to the side chain of monomer **2**. The pH of all deposition solutions containing monomer **2** are below this estimated pK_a value, and thus, the majority (> 78%) of carboxylic acid moieties remain protonated. The acidity of monomer **2** is the main contributor to the pH values of the deposition solutions, but the presence of monomer **1** in the solution, also has an effect. The higher pH value of the 0 mol% **2** solution (5.42) compared to that of the monomer-less solution (5.31) demonstrates the basicity effect of monomer **1**. The presence of SDS does not affect the pH of the solutions. Although the pH of the deposition solution can predict the extent of the electropolymerization, and thus *m*, it does not provide information regarding the relative amounts of monomer incorporated into the film.

In addition to pH, there is another possible explanation for the trend observed for mixed monomer deposition solutions in Figure 3.6a. Previously reported co-electropolymerizations of EDOT and monomer **1** in aqueous solutions, for example, show a preference for the deposition of EDOT, over monomer **1**, up to equimolar ratios of the monomers in the deposition solution.[53] Thus, one could argue that in our case, the decreasing *m* with increasing mol% **2** suggests that

monomer **1** is the one that is predominately deposited. Note, however, that our solution conditions are substantially different (an aqueous solution of 0.1 M $LiClO_4$ and use of a solubilizer) than in the other report (methanol, diluted with aqueous 0.1 M $LiClO_4$). Therefore, the ratio of monomers in our deposited films could also be different. Therefore, an analysis of the ratio of monomers incorporated into the films was performed using μATR-FTIR and XPS, and is described in a subsequent section below.

3.4.2 Thickness and monomer density in polymer films. The packing of oligomers on the electrode surface could affect the electrochemical behavior of the films, including access to counter ions migrating in and out of the polymer network, as well as the path that the electrons travel from one oligomer to the next. Given the proposed mechanism of Figure 3S-12 in the Supporting Information, we do not expect the side chain of monomer **2** to play a major role in the initial electropolymerization. Like EDOT, polymerization of the monomers **1** and **2** is linear through α-α' coupling of the thiophene rings, and the ethylenedioxy ring blocks coupling at the 3 and 4 positions. However, due to steric effects, monomers with a bulkier side chain, as is the case for monomer **2**, should affect the packing of the deposited oligomers and produce a less dense polymer film.

To investigate the extent of packing, profilometry was used to measure the average cross-sectional areas of the polymer films. Representative height profiles from which the cross-sectional areas were obtained are shown in the Supporting Information in Figure 3S-9. The profiles give information about how the polymers were deposited on the electrodes. As expected, there is a build-up of polymer along the edges of the electrodes, for all films, due to enhanced mass transport there from radial diffusion during the electrodeposition. Figure 3S-13 in the Supporting Information shows that the average cross-sectional areas for the polymer films from

the mixed monomer solutions do not exhibit a consistent trend. The two extreme cases of the pristine polymers, 0 and 100 mol% **2**, yielded areas of 60 ± 19 μm^2 and 30 ± 13 μm^2, respectively. Assuming a uniform distribution of polymer along the entire 2000 μm length of the microbands, the molar concentrations of monomer units within the space occupied by the polymer are 12 ± 4 mol L^{-1} and 9 ± 4 mol L^{-1}, respectively. Figure 3S-14 in the Supporting Information compares these molar concentrations for all of the films as a function of mol% **2**. There does not appear to be a definitve trend in this quantity, because of the substantial amount of error (as much as ~36% orginating from the cross-sectional area measurements). Although there is some inherent error in the use of the profilometry instrument (± 0.05 μm) and in digitizing the results, a greater error is likely due to inaccurate profiling of the polymer edges given the speed and size of the profilometer probe. Consistent with this hypothesis is that the average cross-sectional area of the bare gold electrodes (29 ± 5 μm^2), which are flat, is within the error of the expected value of 26 um^2 based on the amount of gold and chromium deposited during thermal evaporation.

Another way to evaluate the profilometry data is to avoid the edges and simply compare the thicknesses for the different films based on the height in center portion of the profiles. These results are also reported in Figure 3S-13. The heights also vary, where films deposited from solutions of 0 and 100 mol% **2** measured 0.27 ± 0.05 and 0.15 ± 0.13 μm,, respectively. There is no discernable trend among the films formed from the mixed monomer solutions.

3.4.3 Relative composition of monomers 1 and 2 in the polymer films determined from μATR-FTIR and XPS analyses. Determining the relative amounts of the two monomers incorporated into the polymer films from the mixed solutions addresses the questions regarding factors affecting the deposition and provides guidance about conditions for preparing films with

desired properties. Quantitative analysis was performed using μATR-FTIR sampling, which can measure spectra from within the 100-μm wide microbands without overlapping with the gaps or other adjacent structures on the chip.

Figure 3.7a shows μATR-FTIR spectra plotted over the 1900 – 750 cm^{-1} range for polymer films electrodeposited from solutions of 100, 66, 50, 25, and 0 mol% **2**. These films had been electrochemically characterized after film formation, thoroughly rinsed and soaked in water and allowed to dry in the air under ambient conditions. Peaks for the films are much broader and some are slightly shifted compared to those for the individual monomers (Figures 3S-3a and 3S-3b in the Supporting Information). The polymer spectra are also similar to those previously reported for poly(**2**) and related polymers and monomers. Table 3.3 summarizes the proposed assignments of vibrational modes of the main peaks highlighted in Figure 3.7a based on spectra reported in the literature. Absorbance bands at 836 and 976 cm^{-1} have been assigned to the stretching of the C-S bond of the thiophene ring.[62-68] Stretching vibrations within the ethyelenedioxy ring absorb at 1062, 1104, 1220 cm^{-1}.[62, 64-66, 68-73] Several IR peaks can be traced to the stretching of the C=C and C-C bonds within the thiophene ring at 1169, 1370, 1477, and 1525 cm^{-1}.[65-67, 69-72, 74] The bending vibration of H_2O molecules retained within the film and the stretching of the C=O bond within the ester of monomer **2** absorb at 1642 and 1739 cm^{-1}, respectively.[46, 75]

Carbonyl group stretching modes within esters exhibit some of the more distinct absorbances in IR spectroscopy, and in the present studies, provide a unique marker for monomer **2**. Figure 3.7b shows an overlay of spectra in the expanded region of 1800 – 1580 cm^{-1} to enable comparison of changes in the ester carbonyl band for polymers formed from varying compositions of deposition solutions and in the bending vibration for the retained H_2O. Although

two carbonyl groups are present on the side chain of monomer **2,** each with distinct vibrational bands in IR spectroscopy, only the C=O stretching vibration of the ester group is evident in spectra of the electropolymerized films. Because the carboxylic acid groups neutralize during the electrochemical characterization of the films in the sodium phosphate buffer, the characteristic band for the carboxylic acid stretch is replaced by lower wavenumber carboxylate group vibrations near 1400 cm^{-1}. Figure 3.7b shows the expected increase in $pATR_{1739}$ for films formed from deposition solutions with increasing mol% **2**. Interestingly, $pATR_{1649}$ displays the opposite trend, decreasing with increasing deposition mol% **2**. The response indicates the electropolymerized films become more resistant to wetting with increasing monomer **2** content, possibly a result of the side-chain hydrophobicity.

A plot of the $pATR_{1739}$ versus the mol% **2** of the deposition solution is shown in Figure 3.7c. The background $pATR_{1739}$ derived from the 0 mol% **2** sample has been removed by subtraction. The near linear calibration relationship ($pATR_{1739} = (9.1\times10^{-4} \pm 0.7\times10^{-4}$ mol% $\mathbf{2}^{-1})$ $x_{\text{mol\% }\mathbf{2}} - 4\times10^{-3} \pm 4\times10^{-3}$ ($R^2 = 0.9800$)) demonstrates the content of monomer **2** in the electropolymerized films can be directly estimated from the deposition solution composition. These data also support the notion that the decreased quantity of electropolymerized monomer that occurs with increasing mol% **2** in solution is due to a change in pH and not the idea that the deposition is dominated by monomer **1**. The fact that the ratio of the two monomers in the polymers tracks their ratio in the deposition solutions, regardless of the total quantity of polymer electrodeposited, suggests that our conditions involve a factor that normalizes the monomer deposition behavior. We attribute this behavior to the solubilizing agent, SDS, which can surround the monomers and create similar chemical nanoenvironments around them. Thus,

encounters of the monomers with each other and with the electrode are also similar, irrespective of side chain structure and composition.

Further confirmation of the chemical composition of the films was obtained by XPS. Because the spot size (110 μm) was slightly larger than the microelectrode width (100 μm), some of the survey spectra (not shown) measured peaks for silicon from the SiO_2-coated silicon substrate. Thus, the analysis of the XPS data here focuses on the C(1s) peaks and does not include the O(1s) peaks. Figure 3.8 shows C(1s) narrow scans of the 0, 25, 34, 50, 66, and 100 mol% **2** films. Deconvolution and fitting of the spectra were performed to confirm contributions of the different carbons and, therefore, the relative amounts of the two monomers toward the spectra. A careful balance between mathematical overfitting and reasonable assessment of the spectra considering the expected chemistry was the overall goal. Figure 3.8a is the deconvolution and fit of the 0 mol% **2** film to four synthetic components, one for each type of carbon and one for the contribution from π-π* shake-up within the thiophene; for Figures 3.8b–f there are eight total synthetic components. See the color-coded carbons in the structure shown in Figure 3.8g as a guide. The first and second components (cyan and black, respectively) are from the carbons that are in-between the ester and carboxylic acid and present only in monomer **2** (284.1 ± 0.4 eV) and the carbons adjacent to the sulfur in the thiophene ring that are present in both monomers (284.62 ± 0.11 eV). The third component (red) is attributed to the other two carbons in the thiophene ring at 285.44 ± 0.08 eV. One carbon in the ethylenedioxy bridge and the methylene carbon have been designated as equivalent and contribute to the fourth component (orange) at 286.3 ± 0.3 eV. The other carbon in the ethylenedioxy bridge is accounted for in the fifth component (blue) at 287.4 ± 0.3 eV. The sixth and seventh components are only present in films containing monomer **2** and are due to the carbons of the ester (green) and carboxylic acid

(purple). They give rise to peaks at 288.6 ± 0.3 and 289.0 ± 0.4 eV, respectively. Despite the synthetic components and their specific position, there is an increase in signal corresponding to carbons with a higher binding energy as the films were produced from deposition solutions with increasing mol% **2**. Therefore, the XPS C(1s) spectra support the μATR-FTIR data and show an increase in the ester content of the films as the mol% **2** in the deposition solution increases. Because XPS is a surface analysis technique (depth of ~10 nm), these results also suggest there is not a major difference between the surface and the bulk composition of the films.

3.4.4 Electrochemical characterization of the polymer films. Figure 3S-15 in the Supporting Information shows CV responses of polymer films obtained in two different solutions: 0.2 M sodium phosphate buffer and 0.2 M of the buffer containing 0.001 M $K_4Fe(CN)_6$. The shapes of the voltammograms in buffer alone are similar to those observed for PEDOT in aqueous supporting electrolytes, where the current is relatively flat across the entire voltage range of -0.100 to +0.700 V.[57] This behavior is similar to the charging of a capacitor. Such behavior is also observed for CV in buffer containing ferrocyanide during the forward sweep at potentials negative of the E° value and before the faradaic current becomes pronounced. The capacitances (*C*) obtained from CV in both of these characterization solutions are shown in Figure 3.9 and listed in Table 3.2 for the polymer films as a function of the mol% **2** of their deposition solutions. The *C* values obtained from the redox solution are within error of or slightly larger than those obtained in solutions of buffer alone. The small increase in *C* could be due to the increased ionic strength from the additional $K_4Fe(CN)_6$.

The average *C* of the bare gold microelectrodes (0.0650 ± 0.0004 mF cm^{-2}, N=17) before modification has the expected magnitude for these conditions. Interestingly, it is indistinguishable from that for the films resulting from the 100 mol% **2** deposition solution

(0.065 ± 0.004 mF cm^{-2}, N=3). Yet, a purple color, a substantial amount of charge passed during electrodeposition, and the μATR-FTIR and XPS data confirm the presence of a 100 mol% **2** film. Although the electropolymerization in the 100 mol% **2** solution deposited as much as half of the number of monomers that were deposited from the 0 mol% **2** solution (Figure 3.6a), it is as if those sites are inaccessible in the polymer for oxidation and re-reduction and therefore the only contribution to the background current is the charging of the double layer at the polymer/solution interface.

The incorporation of increasing amounts of monomer **2,** however, does not adversely affect the measured capacitances for the mixed polymers. For the range of 0 to 75 mol% **2**, the decrease in capacitance (Figure 3.9, slope = $-5.1\times10^{-3} \pm 6\times10^{-4}$ mol% $\mathbf{2}^{-1}$, normalized to the 0 mol% **2** value) is the same as the decrease in the quantity of monomers deposited (Figure 3.6, slope = $-5.2\times10^{-3} \pm 3\times10^{-4}$ mol% $\mathbf{2}^{-1}$, normalized to the 0 mol% **2** value). Another way to illustrate this point is by plotting $C_{normalized}$ vs. $m_{normalized}$ as shown in Figure 3S-16 of the Supporting Information. This comparison assesses whether changes in capacitance are simply proportional to the quantity of polymer (expecting a linear relationship and slope of unity) or influenced more by the relative composition of **2:1** in the polymer (expecting a nonlinear relationship and a slope not equal to one). Least squares analysis for points 0 to 75 mol% **2** in Figure 3S-16 yields: $C_{normalized} = (1.01 \pm 0.09\ C_{normalized}\ (m_{normalized})^{-1})\ x_{m_{normalized}} - 0.01 \pm 0.07\ C_{normalized}$ ($R^2 = 0.9672$). The R^2 value suggests a fairly linear relationship, although not strong. However, the slope is indeed unity, confirming that it is the quantity of monomer deposited that determines the capacitance and not the relative composition of monomers **2** and **1** in the polymer films. Interestingly, the y-intercept of the linear regression, which ideally represents the double layer capacitance when there is no film (a bare electrode) is within error of the measured double

layer capacitance of the bare electrodes (0.0650 ± 0.0004 mF cm^{-2} / 3.65 ± 0.06 mF cm^{-2} = 0.0178 ± 0.0003).

This retained electrochemical activity suggests that the bulkier side group of monomer **2** does not disrupt the conductivity between neighboring oligomer groups within the polymer network. In addition, it appears that the negative charge of monomer **2** due to deprotonation of the carboxylic acid groups, as is supported by the μATR-FTIR data, does not impede counter ion compensation that is needed for the polymer to oxidize and reduce. The presence of carboxylate anions within the polymer likely contribute toward ion compensation themselves, requiring cations to enter the films because the carboxylates are tethered, transferring the role of charge compensation from anions to cations, as is known to occur in polymers of PEDOT formed with polystyrenesulfonate (PSS).[76] It should also be noted that the rinsing, electrochemical cycling in the buffer, and storage in water after the electropolymerization step remove residual SDS. This is supported by the lack of absorption bands specific to SDS in the μATR-FTIR data. Thus, the normalizing effect that SDS has on the different side chains of the monomers during electropolymerization no longer applies to the monomer units within the polymer after the films are formed.

Investigation of the faradaic electrochemistry of $[Fe(CN)_6]^{4-}$ in buffer using CV at electrodes modified with the conducting polymer films was intended to establish the facility to electron transfer across the polymer/solution interface. The shapes of the resulting CV responses (see Figure 3S-15 in Supporting Information) for all films at 0.100 V s^{-1} are consistent with mass transport that is dominated by planar, diffusion-limited behavior. The diffusion length is estimated to be approximately 80 μm by the Einstein equation, which is on the same order of magnitude as the width of the electrodes and suggests that there may be some minor contribution

from hemicylindrical diffusion as well. The background-subtracted forward peak currents, i_{pa}, reverse peak currents, i_{pc}, their ratio, i_{pc}/i_{pa}, and peak separations, ΔE_p are listed in Table 3.2.

The faradaic peak currents (background-subtracted) from the CV responses at the different polymer films can be compared. The Randles-Sevcik equation predicts the forward peak current to be 0.43 μA at a planar electrode with dimensions of the microband electrodes (100 μm × 2000 μm, assuming the height 0.025 μm provides a negligible contribution), at 23 °C, and for $[Fe(CN)_6]^{4-}$ (n = 1 mole of electrons/mole of molecules) using a diffusion coefficient of 0.65×10^{-5} cm^2 s^{-1}.[77] This predicted value is within the error of the i_{pa} obtained for the bare gold electrodes. The i_{pa} values for the polymer films range from 22 to 93% larger than this, with a median of 31%, and do not appear to follow any particular trend with the mol% **2**. The higher current could result from the higher surface area of the polymer films. The variation in i_{pa} could derive from polymer growth that is affected by a combination of planar and hemicylindrical diffusion during each deposition sweep that builds on the morphology of the previous deposition, producing nonuniform films. This is consistent with cross sectional areas and nonuniform profiles measured by profilometry (Figure 3S-9 in Supporting Information).

The ratio of the reverse peak current to that of the forward peak (i_{pc}/i_{pa}) is expected to be unity for a reversible electron transfer with a stable anodic product. This ratio also allows comparisons of electrochemical behavior between different films by normalizing out the varying i_{pa} values. The ratio appears to follow a trend from the largest of 1.32 ± 0.04 for the 0 mol% **2** film to the smallest of 0.89 ± 0.02 for the 100 mol% **2** film. A ratio greater than unity is consistent with films that exhibit an expansion during oxidative excursions to accommodate the incorporation of anions to compensate charge. The film is most expanded in its anodic state, as has been observed thick films of PEDOT as described previously.[57] A growing film can oxidize

increasingly more ferrocyanide in the forward sweep past the anodic peak and possibly push through the diffusion layer to access fresh solution. As the potential passes E° in the return sweep, a larger peak occurs because of a higher ferricyanide concentration, than would have been produced had the film not increased size. Ratios less than unity for films with high mol% **2** suggest that the least expanded film is in its anodic state, when tethered carboxylate anions internally compensate for the positive charge along the backbone. The oxidation peak of ferrocyanide appears with diminishing oxidation in the forward sweep as the film contracts. It is during the reductive excursions that the film expands, when cations must enter the polymer to compensate for the immobilized negative charges of the carboxylates, but there is less ferricyanide available to reduce than if the film had not changed size. A smaller faradaic peak for in the return sweep of films of high mol% **2** could also be partially explained by more repulsion of the anionic redox species, whereas in the forward anodic sweep, $[Fe(CN)_6]^{4-}$ can also serve as a counter ion for the polymer oxidation. However, the high concentration of supporting electrolyte should shield most of the migration of the redox species in solution.

The separation of the forward and reverse peaks, ΔE_p, is near the ideal value of +0.059 V for n = 1 and 25 °C,[78] with the exception of the film formed from the 100 mol% **2** solution, where $\Delta E_p = + 0.17 \pm 0.03$ V and is within a standard deviation of that for the bare gold electrodes, $\Delta E_p = + 0.14 \pm 0.03$ V. The larger ΔE_p could be due to two reasons, the electron transfer kinetics are slowed because of the surface chemistry or there is substantial uncompensated resistance within the electrode or polymer. The behavior on the bare gold electrodes is most likely due to a slowed oxidation of ferrocyanide. Thus, it stands to reason that the 100 mol% **2** films, which behave like the bare gold electrodes in buffer alone for the proposed reasons described above, should also exhibit similar resistance to electron transfer. For all the other films

containing monomer **1** (0 – 75 mol% **2**), however, the resistivity is both low and electron transfer to the redox species in solution is fast.

3.5 Conclusions

Co-electropolymerization on gold microband electrodes was performed from solutions of varying ratios of monomers **1** and **2** (two derivatives of EDOT) and the properties of the resulting films were investigated by electrochemical methods, profilometry, μATR-FTIR, and XPS. Deposition volumes were conserved and a chip-based, multi-electrode array could be exploited for these studies by using a specialized electrochemical cell designed and built for this purpose.

The more acidic pH of the deposition solutions containing higher mol% **2** decreases the total quantity of monomers deposited, and the presence of SDS appears to equalize the mobility of the monomers, their interaction with the electrode surface and with each other to incorporate **1** and **2** into the films at the same ratio as in the deposition solutions. Polymer films containing increasing amounts of **2** relative to **1** do not exhibit significantly different packing densities. They demonstrate similar charging capacities and electron transfer facility with redox species in solution for a given total number of monomers deposited. It is likely for high mol% **2** polymer films that the carboxylate groups of **2** play a role in the internal charge compensation during oxidative and reductive excursions, reversing the expansion and contraction of films.This is because cation transport from the aqueous solution dominates the charge compensation in those polymers. Additional studies would need to be performed to further investigate this idea. Although for the 100 mol% **2** films, faradaic charging capacity beyond double layer charging appears to be completely shut down.

These studies have demonstrated tunable formation of electropolymerized films with predictable numbers of carboxylic acid and hydroxyl functional groups, without affecting the charging capacity of the films relative to the total monomer deposited. One can take advantage of the COOH and OH moieties to implement subsequent functionalization, selective to one or the other of these groups, and thereby further tailor the films' physical and chemical properties for applications in energy and sensing. The films containing any ratio of **2** to **1**, except 100 mol% **2**, would retain similar charge storage in supercapacitors and fast electron transfer kinetics for mediators, reporters, and analytes in chemical sensing.

The extent to which SDS can normalize the co-electropolymerization of other monomers from aqueous solutions to form films of prescribed composition is an intriguing possibility. It would allow for the option to synthesize and purify monomers with more complex functional groups prior to film formation, which might be too difficult to do and less homogeneously distributed if performed after electrodeposition of the precursors.

3.6 Acknowledgments.

We are grateful for financial support from the National Science Foundation (CBET-1336853 and CMI-1808286), the Arkansas Biosciences Institute, the major research component of the Arkansas Tobacco Settlement Proceeds Act of 2000, as well as Grant Number P30 GM103450 from the National Institutes of General Medicine Sciences of the National Institutes of Health (NIH). We recognize the support of the Arkansas Statewide MS facility staff and their help in obtaining the LC-ESI-MS data of the monomers. We also thank Joel M. Harris for use of the μATR-FTIR instrumentation. This work made use of the University of Utah Surface Analysis Lab shared facility of the Micron Technology Foundation Inc. Microscopy Suite sponsored by the College of Engineering, Health Sciences Center, Office of the Vice President

for Research, and the Utah Science Technology and Research (USTAR) initiative of the State of Utah.

3.7 Supporting Information.

Supporting information includes ^{1}H NMR, ATR-FTIR, and LC-ESI-MS characterization of monomers **1** and **2**, procedure for measuring E_{onset} and fitting of XPS data, electrodeposition voltammograms, optical images of unmodified and polymer-modified gold electrodes in arrays, profilometry data, proposed electropolymerization mechanism, CV responses of polymer-modified electrodes in buffer and buffer plus ferrocyanide, plots showing monomer quantity per volume occupied by polymer and how changes in normalized *C* track normalized *m* for films containing different mol% **2**.

3.8 References

1. L. B. Groenendaal, F. Jonas, D. Freitag, H. Pielartzik, and J. R. Reynolds, *Adv. Mater. (Weinheim, Ger.)*, **12** (7), 481-494 (2000).

2. J. G. Ibanez, M. E. Rincon, S. Gutierrez-Granados, M. h. Chahma, O. A. Jaramillo-Quintero, and B. A. Frontana-Uribe, *Chem. Rev. (Washington, DC, U. S.)*, **118** (9), 4731-4816 (2018).

3. G. Kaur, R. Adhikari, P. Cass, M. Bown, and P. Gunatillake, *RSC Adv.*, **5** (47), 37553-37567 (2015).

4. R. Green and M. R. Abidian, *Adv. Mater. (Weinheim, Ger.)*, **27** (46), 7620-7637 (2015).

5. B. Zhu, S.-C. Luo, H. Zhao, H.-A. Lin, J. Sekine, A. Nakao, C. Chen, Y. Yamashita, and H.-h. Yu, *Nat. Commun.*, **5** 4523 (2014).

6. Y.-S. Hsiao, S.-C. Luo, S. Hou, B. Zhu, J. Sekine, C.-W. Kuo, D.-Y. Chueh, H.-h. Yu, H.-R. Tseng, and P. Chen, *Small*, **10** (15), 3012-3017 (2014).

7. R. Balint, N. J. Cassidy, and S. H. Cartmell, *Acta Biomater.*, **10** (6), 2341-2353 (2014).

8. J. Dapra, K. Kiilerich-Pedersen, N. O. Christiansen, C. R. Poulsen, and N. Rozlosnik, in *Nanomedicine in Diagnostics*, p. 96-119, CRC, (2012).

9. J. Sekine, S.-C. Luo, S. Wang, B. Zhu, H.-R. Tseng, and H.-h. Yu, *Adv. Mater. (Weinheim, Ger.)*, **23** (41), 4788-4792 (2011).

10. S. C. Luo, E. Mohamed Ali, N. C. Tansil, H. H. Yu, S. Gao, E. A. Kantchev, and J. Y. Ying, *Langmuir*, **24** (15), 8071-8077 (2008).

11. R. J. Mortimer, *Annu. Rev. Mater. Res.*, **41** 241-268 (2011).

12. X. Liu, *Small*, **6** (21), 2333-2335 (2010).

13. H. Yoon and J. Jang, *Adv. Funct. Mater.*, **19** (10), 1567-1576 (2009).

14. H. Bai and G. Shi, *Sensors*, **7** (3), 267-307 (2007).

15. J. Janata and M. Josowicz, *Nat. Mater.*, **2** (1), 19-24 (2003).

16. D. T. McQuade, A. E. Pullen, and T. M. Swager, *Chem. Rev. (Washington, D. C.),* **100** (7), 2537-2574 (2000).

17. N. Aydemir, J. Malmstrom, and J. Travas-Sejdic, *Phys. Chem. Chem. Phys.*, **18** (12), 8264-8277 (2016).

18. S. Cosnier, *Analytical and Bioanalytical Chemistry,* **377** (3), 507-520 (2003).

19. A. Kros, R. J. M. Nolte, and N. A. J. M. Sommerdijk, *Adv. Mater. (Weinheim, Ger.),* **14** (23), 1779-1782 (2002).

20. G. Bidan, M. Billon, T. Livache, G. Mathis, A. Roget, and L. M. Torres-Rodriguez, *Synth. Met.*, **102** (1-3), 1363-1365 (1999).

21. T. P. Kaloni, P. K. Giesbrecht, G. Schreckenbach, and M. S. Freund, *Chem. Mater.*, **29** (24), 10248-10283 (2017).

22. E. W. C. Chan, P. Baek, D. Barker, and J. Travas-Sejdic, *Polym. Chem.,* **6** (43), 7618-7629 (2015).

23. P. Blanchard, A. Cravino, and E. Levillain, in *Handbook of Thiophene-Based Materials: Applications in Organic Electronics and Photonics,* Vol. 2, p. 419-453, John Wiley & Sons Ltd., (2009).

24. C. Zanardi, F. Terzi, and R. Seeber, *Anal. Bioanal. Chem.,* **405** (2-3), 509-531 (2013).

25. M. F. Abasiyanik and M. Şenel, *Journal of Electroanalytical Chemistry,* **639** (1-2), 21-26 (2010).

26. M. Hiller, C. Kranz, J. Huber, P. Baeuerle, and W. Schuhmann, *Adv. Mater. (Weinheim, Ger.),* **8** (3), 219-222 (1996).

27. G. Zotti, B. Vercelli, and A. Berlin, *Acc. Chem. Res.*, **41** (9), 1098-1109 (2008).

28. G. Barbarella, M. Melucci, and G. Sotgiu, *Adv. Mater. (Weinheim, Ger.),* **17** (13), 1581-1593 (2005).

29. J. Roncali, *Chem. Rev.,* **92** (4), 711-738 (1992).

30. C. Stromberg, V. Tsakova, and J. W. Schultze, *J. Electroanal. Chem.*, **547** (2), 125-133 (2003).

31. V. Tsakova, S. Winkels, and J. W. Schultze, *Electrochim. Acta,* **46** (5), 759-768 (2000).

32. N. Sakmeche, E. A. Bazzaoui, M. Fall, S. Aeiyach, M. Jouini, J. C. Lacroix, J. J. Aaron, and P. C. Lacaze, *Synth. Met.,* **84** (1-3), 191-192 (1997).

33. H.-B. Bu, G. Goetz, E. Reinold, A. Vogt, S. Schmid, R. Blanco, J. L. Segura, and P. Baeuerle, *Chem. Commun. (Cambridge, U. K.),* (11), 1320-1322 (2008).

34. A. Lima, P. Schottland, S. Sadki, and C. Chevrot, *Synth. Met.,* **93** (1), 33-41 (1998).

35. J. Roncali, P. Blanchard, and P. Frere, *J. Mater. Chem.,* **15** (16), 1589-1610 (2005).

36. E. M. Ali, E. A. B. Kantchev, H.-h. Yu, and J. Y. Ying, *Macromolecules,* **40** (17), 6025-6027 (2007).

37. J. Arias-Pardilla, T. F. Otero, and H.-h. Yu, *Electrochim. Acta,* **56** (27), 10238-10245 (2011).

38. S.-C. Luo, H. Xie, N. Chen, and H.-h. Yu, *ACS Appl. Mater. Interfaces,* **1** (7), 1414-1419 (2009).

39. S.-C. Luo, B. Zhu, A. Nakao, R. Nakatomi, and H.-h. Yu, *Adv. Biomater. (Weinheim, Ger.),* (6), B423-B427 (2011).

40. B. Kannan, D. E. Williams, C. Laslau, and J. Travas-Sejdic, *Biosens. Bioelectron.,* **35** (1), 258-264 (2012).

41. S.-C. Luo, J. Sekine, B. Zhu, H. Zhao, A. Nakao, and H.-h. Yu, *ACS Nano,* **6** (4), 3018-3026 (2012).

42. T. Darmanin and F. Guittard, *Soft Matter,* **9** (25), 5982-5990 (2013).

43. J. Malmstrom, M. K. Nieuwoudt, L. T. Strover, A. Hackett, O. Laita, M. A. Brimble, D. E. Williams, and J. Travas-Sejdic, *Macromolecules (Washington, DC, U. S.),* **46** (12), 4955-4965 (2013).

44. D. Hu, L. Zhang, K. Zhang, X. Duan, J. Xu, L. Dong, H. Sun, X. Zhu, and S. Zhen, *J. Appl. Polym. Sci.,* **132** (9), 41559/41551-41559/41559 (2015).

45. F. Mouffouk and S. J. Higgins, *Electrochem. Commun.,* **8** (2), 317-322 (2006).

46. L. Zhang, Y. Wen, Y. Yao, J. Xu, X. Duan, and G. Zhang, *Electrochimica Acta,* **116** 343-354 (2014).

47. N. Bhagwat, K. L. Kiick, and D. C. Martin, *J. Mater. Res.,* **29** (23), 2835-2844 (2014).

48. N. Bhagwat, R. E. Murray, S. I. Shah, K. L. Kiick, and D. C. Martin, *Acta Biomater.,* **41** 235-246 (2016).

49. H. Brisset, A.-E. Navarro, C. Moustrou, I. F. Perepichka, and J. Roncali, *Electrochem. Commun.,* **6** (3), 249-253 (2004).

50. S.-C. Luo, H.-h. Yu, A. C. A. Wan, Y. Han, and J. Y. Ying, *Small,* **4** (11), 2051-2058 (2008).

51. T. Darmanin and F. Guittard, *ChemPhysChem,* **14** (11), 2529-2533 (2013).

52. W. J. Doherty, III, R. J. Wysocki, Jr., N. R. Armstrong, and S. S. Saavedra, *J. Phys. Chem. B,* **110** (10), 4900-4907 (2006).

53. W. J. Doherty, III, R. J. Wysocki, N. R. Armstrong, and S. S. Saavedra, *Macromolecules,* **39** (13), 4418-4424 (2006).

54. F. S. Marrikar, M. Brumbach, D. H. Evans, A. Lebrón-Paler, J. E. Pemberton, R. J. Wysocki, and N. R. Armstrong, *Langmuir,* **23** (3), 1530-1542 (2007).

55. E. C. Anderson, M. C. Weston, and I. Fritsch, *Anal. Chem. (Washington, DC, U. S.),* **82** (7), 2643-2651 (2010).

56. W. Kern and D. A. Puotinen, *RCA Rev.,* **31** (2), 187-206 (1970).

57. F. Z. Khan and I. Fritsch, *Journal of the Electrochemical Society,* **166** (13), H615-H627 (2019).

58. H. Ayalew, T.-l. Wang, and H.-h. Yu, *Polymers (Basel, Switz.),* **11** (4), 659 (2019).

59. L. Zhang, Y. P. Wen, Y. Y. Yao, J. K. Xu, X. M. Duan, and G. Zhang, *Electrochimica Acta,* **116** 343-354 (2014).

60. J. Heinze, B. A. Frontana-Uribe, and S. Ludwigs, *Chem Rev,* **110** (8), 4724-4771 (2010).

61. D. R. Lide and H. P. R. Frederikse, *CRC Handbook of Chemistry and Physics, 78th Edition*, p. 2512, CRC (1997).

62. T. Bahry, Z. P. Cui, A. Deniset-Besseau, M. Gervais, C. Sollogoub, T. T. Bui, and S. Remita, *New Journal of Chemistry*, **42** (11), 8704-8716 (2018).

63. K. Deshmukh and G. M. Joshi, *Rsc Adv*, **4** (71), 37954-37963 (2014).

64. S. Golba, M. Lezniak, J. Gabor, and F. Tomasz, *Synth. Met.*, **199** 310-318 (2015).

65. C. Kvarnstrom, H. Neugebauer, S. Blomquist, H. J. Ahonen, J. Kankare, and A. Ivaska, *Electrochim. Acta*, **44** (16), 2739-2750 (1999).

66. C. Li and T. Imae, *Macromolecules*, **37** (7), 2411-2416 (2004).

67. Y. Yao, Y. Wen, L. Zhang, Z. Wang, H. Zhang, and J. Xu, *Anal. Chim. Acta*, **831** 38-49 (2014).

68. L. Zhan, Z. Song, J. Zhang, J. Tang, H. Zhan, Y. Zhou, and C. Zhan, *Electrochimica Acta*, **53** (28), 8319-8323 (2008).

69. S. Ghosh, H. Remita, L. Ramos, A. Dazzi, A. Deniset-Besseau, P. Beaunier, F. Goubard, P.-H. Aubert, F. Brisset, and S. Remita, *New J. Chem.*, **38** (3), 1106-1115 (2014).

70. Y. Lattach, A. Deniset-Besseau, J.-M. Guigner, and S. Remita, *Radiat. Phys. Chem.*, **82** 44-53 (2013).

71. S. Rattan, P. Singhal, and A. L. Verma, *Polym Eng Sci*, **53** (10), 2045-2052 (2013).

72. A. Szkurlat, *Electrochimica Acta*, **48** (24), 3665-3676 (2003).

73. F. Tran-Van, S. Garreau, G. Louarn, G. Froyer, and C. Chevrot, *Journal of Materials Chemistry*, **11** (5), 1378-1382 (2001).

74. P. Damlin, C. Kvarnström, and A. Ivaska, *Journal of Electroanalytical Chemistry*, **570** (1), 113-122 (2004).

75. S. Khan, M. Ul-Islam, W. A. Khattak, M. W. Ullah, and J. K. Park, *Carbohyd Polym*, **127** 86-93 (2015).

76. N. J. Yang and C. G. Zoski, *Langmuir*, **22** (25), 10338-10347 (2006).

77. M. Vonstackelberg, M. Pilgram, and V. Toome, *Z. Elektrochem.*, **57** (5), 342-350 (1953).

78. A. J. Bard and L. R. Faulkner, *Electrochemical methods : fundamentals and applications*, p. xxi, 833 p., Wiley, New York (2001).

3.9 Tables

Table 3.1. Measured pH values of deposition solutions and electropolymerization results.

Mol% 2	pH[a]	Q_T (μC)[b]	m (nmol)	E_{onset}[b]		
				Cycle 1 (V)	Cycle 2 (V)	Cycle 3 (V)
0	5.42	310 ± 5	1.38 ± 0.02	0.946 ± 0.003	0.8836 ± 0.0007	0.8685 ± 0.0009
25	3.29	270 ± 8	1.22 ± 0.04	0.958 ± 0.001	0.8951 ± 0.0003	0.886 ± 0.001
34	3.23	250 ± 3	1.12 ± 0.01	0.982 ± 0.003	0.9066 ± 0.0004	0.8952 ± 0.0008
50	3.14	230 ± 3	1.04 ± 0.01	0.971 ± 0.002	0.9121 ± 0.0003	0.9063 ± 0.0006
66	3.05	210 ± 7	0.94 ± 0.03	0.983 ± 0.001	0.930 ± 0.001	0.926 ± 0.002
75	3.01	180 ± 16	0.82 ± 0.07	0.955 ± 0.003	0.899 ± 0.001	0.889 ± 0.003
100	2.96	130 ± 11[c]	0.60 ± 0.05[c]	1.03 ± 0.02[c]	0.97 ± 0.01[c]	0.969 ± 0.004[c]

[a]pH of solution without monomer was 5.31 (aqueous solution containing 0.05 M SDS and 0.1 M $LiClO_4$).

[b]Averages ± standard deviation obtained from the different electrodes on the same chip, except for the 100 mol% **2** case.

[c]Averages ± standard deviation obtained from six different electrodes on the same chip for the 100 mol% **2**.

Table 3.2. Electrochemical and infrared spectroscopy characterization of polymer films.

	Electrochemical Characterization						μATR-FTIR
	C (mF cm^2)		Faradaic Response				pATR
Mol% 2	sodium phosphate[b]	ferrocyanide[b]	ΔE_p (V)[b]	i_{pa} (μA)[b]	i_{pc} (μA)[b]	i_{pc} / i_{pa}[b]	$\bar{\nu}$ = 1739 cm^{-1}
Bare Au	0.0650 ± 0.0004	N/A	0.14 ± 0.03	-0.44 ± 0.05	0.37 ± 0.06	0.8 ± 0.2	N/A
0	3.58 ± 0.02	3.71 ± 0.05	0.064 ± 0.007	-0.63 ± 0.02	0.83 ± 0.01	1.32 ± 0.03	0.0
25	3.20 ± 0.01	3.5 ± 0.2	0.075 ± 0.003	-0.567 ± 0.009	0.615 ± 0.007	1.08 ± 0.02	0.0181
34	2.79 ± 0.02	2.80 ± 0.06	0.074 ± 0.003	-0.57 ± 0.01	0.571 ± 0.006	1.01 ± 0.01	N/A
50	2.70 ± 0.02	2.97 ± 0.06	0.075 ± 0.003	-0.57 ± 0.02	0.628 ± 0.006	1.10 ± 0.01	0.0358
66	N/A	2.5 ± 0.1	0.073 ± 0.003	-0.84 ± 0.04	0.83 ± 0.03	1.00 ± 0.05	0.0511
75	2.17 ± 0.01	2.1 ± 0.1	0.073 ± 0.003	-0.622 ± 0.008	0.58 ± 0.01	0.93 ± 0.03	N/A
100	0.065 ± 0.004[c]	N/A[c]	0.17 ± 0.03[c]	-0.53 ± 0.09[c]	0.47 ± 0.06[c]	0.9 ± 0.2[c]	0.0922

[b]Averages ± standard deviation obtained from the different electrodes on the same chip, except for the 100 mol% **2** case.

[c]Averages ± standard deviation obtained from six different electrodes on the same chip for the 100 mol% **2**.

Table 3.3. Absorption bands of μATR-FTIR of co-electrpolymerized films.

Wavenumber (cm^{-1})	Assignment	References
836, 976	ν(C-S)$_{thiophene}$	62-68
1062, 1104, 1220	ν(C-C), ν(-COROC-)$_{ethylenedioxy\ ring}$	62, 64-66, 68-73
1169, 1370	ν(C-C)$_{thiophene}$	65, 72, 74
1477, 1525	ν(C=C), ν(C-C)$_{thiophene}$	66, 67, 69-71
1642	δ(H_2O)	75
1739	ν(C=O)$_{ester}$	46

v = stretching and δ = bending

3.10 Figures

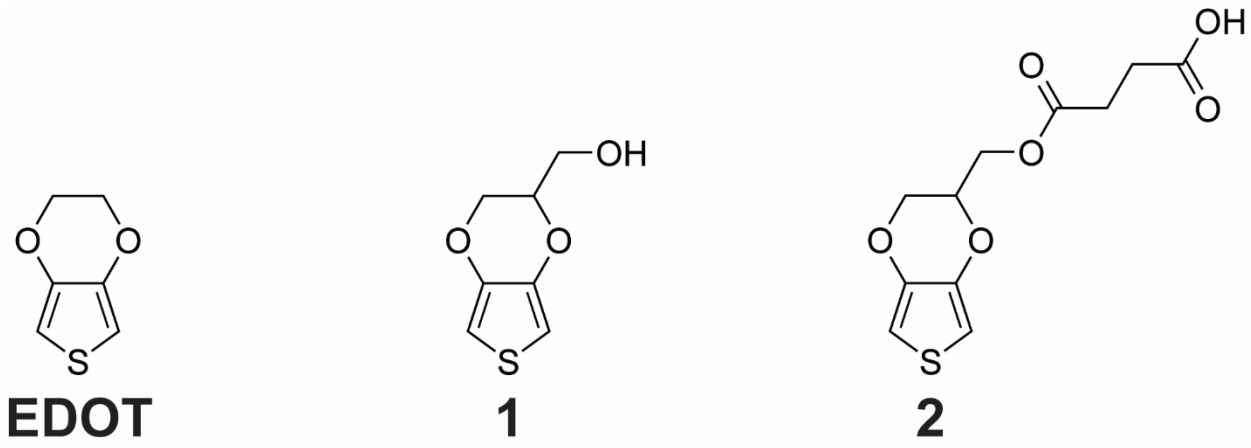

Figure 3.1. Molecular structures of monomers relevant to this work. EDOT, widely reported in the literature, shares the same base structure as **1** and **2**. Monomers **1** and **2** are synthesized independently from EDOT. Monomer **2** is synthesized from **1**.

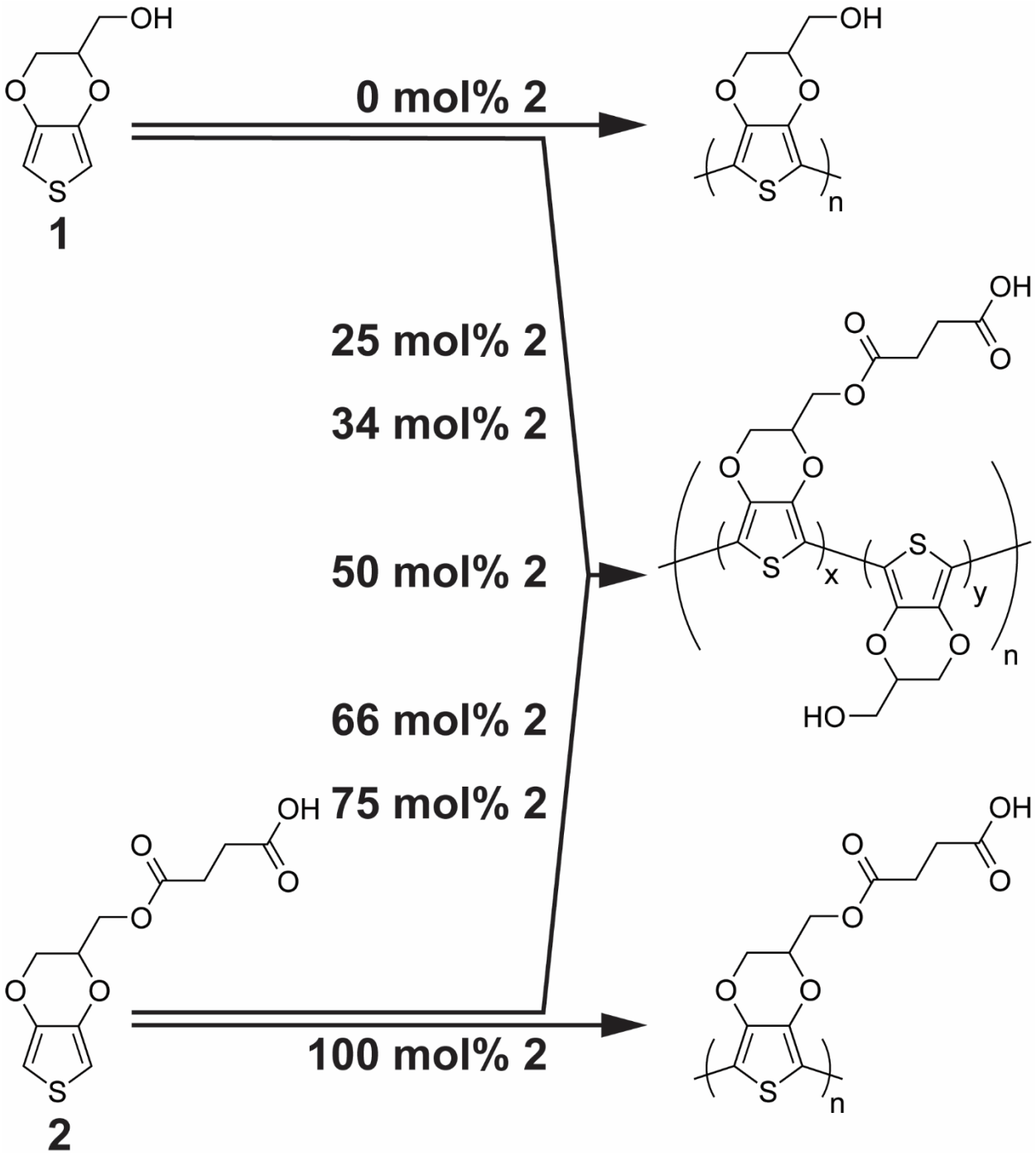

Figure 3.2. Strategy for electropolymerization of monomers **1** and **2** to form copolymer blends. The deposition solutions studied contained the following monomer **2** compositions: 0, 25, 34, 50, 66, 75, and 100 mol% **2**, where mol% **2** = [mol **2** / (mol **1** + mol **2**)] × 100%. The total monomer concentration in the deposition solutions was maintained constant at 0.02 M.

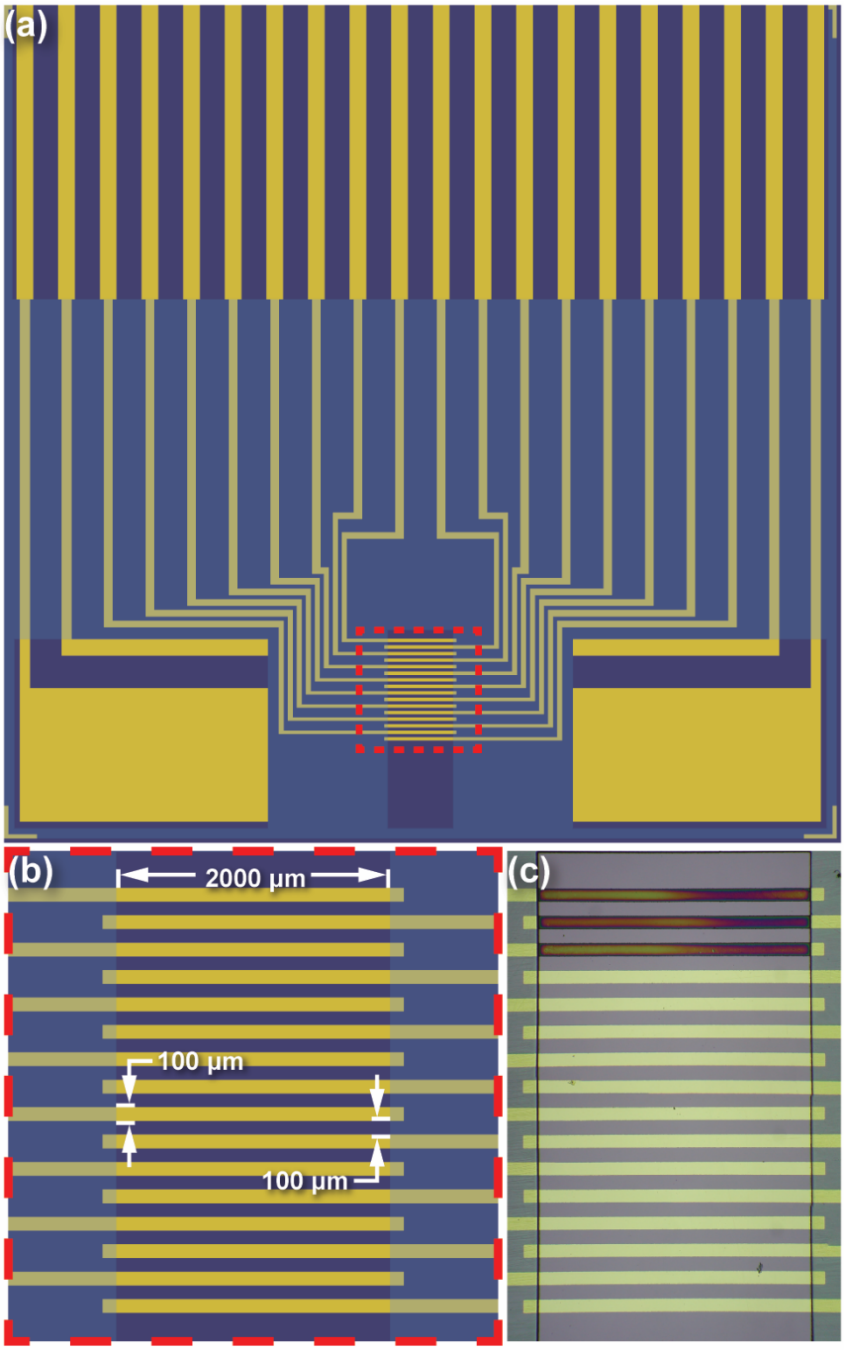

Figure 3.3. The electrode chip. **(a)** Design schematic of the entire 2.54 cm × 2.54 cm chip, showing individually-addressable electrodes and their corresponding contact pads (yellow-gold), and the overlying BCB insulating layer (blue green shading). **(b)** Expanded view of the schematic showing the individually addressable microband electrodes within the array and their corresponding dimensions. The electroactive regions of the microelectrodes are 0.200 cm long as defined by the edges of the BCB, 0.010 cm wide, and separated by 0.010 cm gaps. **(c)** An optical microscopy image of the fabricated electrode array with polymer films on three of the microelectrodes, deposited from a 50 mol% **2** solution

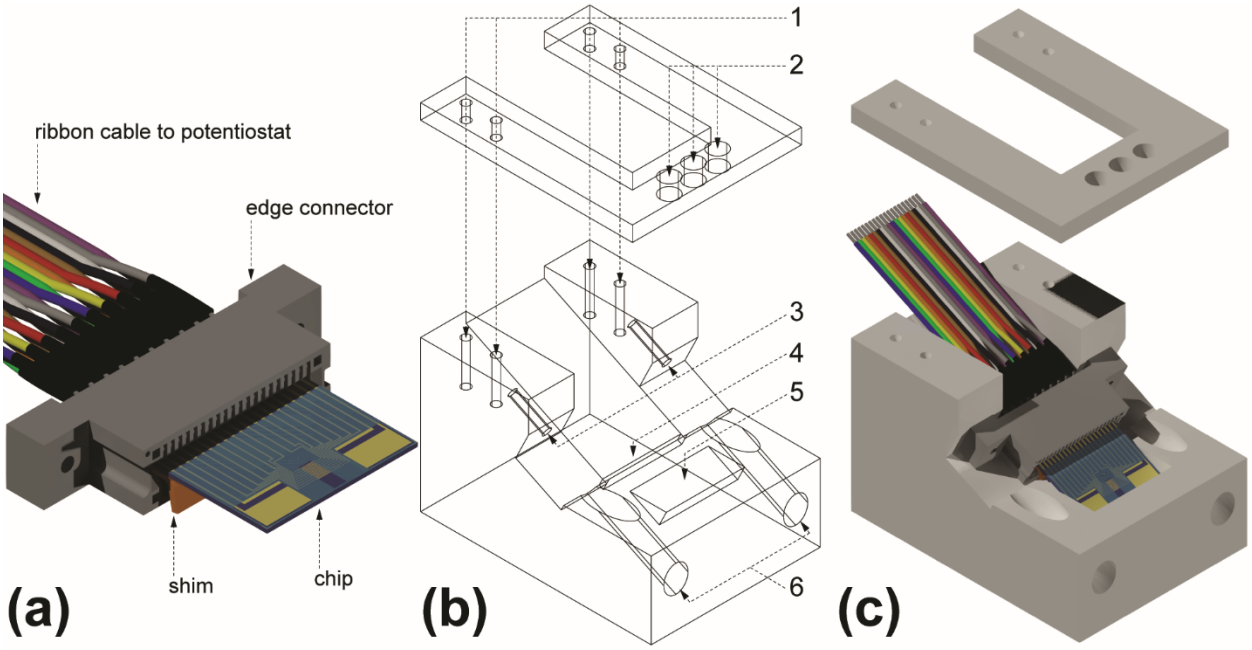

Figure 3.4. Chip/edge connector assembly and deposition cell schematic. **(a)** 3D rendering of the edge connector assembly. **(b)** 2D wireframe projection of deposition cell. **(c)** 3D rendering of the lid and body of the deposition cell. The edge connector assembly consists of three main parts: the edge connector, chip, and shim. The 20-wire ribbon cable is soldered to contact posts at the rear of the edge connector using a plastic shim (thickness: 0.99 mm). The cell consists of two main parts: the lid (on top) and the body (on bottom). The lid is fixed to the body by four machine screws through the inserts labeled by 1. Three holes, 2, provide options for counter and reference electrode placement. The edge connector is fastened to the body of the cell by screws tightened in two holes, 3. The shim sits in a channel, 4, so that the chip/edge connector assembly lies flat against the cell body. The free end of the chip is immersed into the solution contained in the sample well, 5. Paths, 6, for a screwdriver to fasten the edge connector to the cell body.

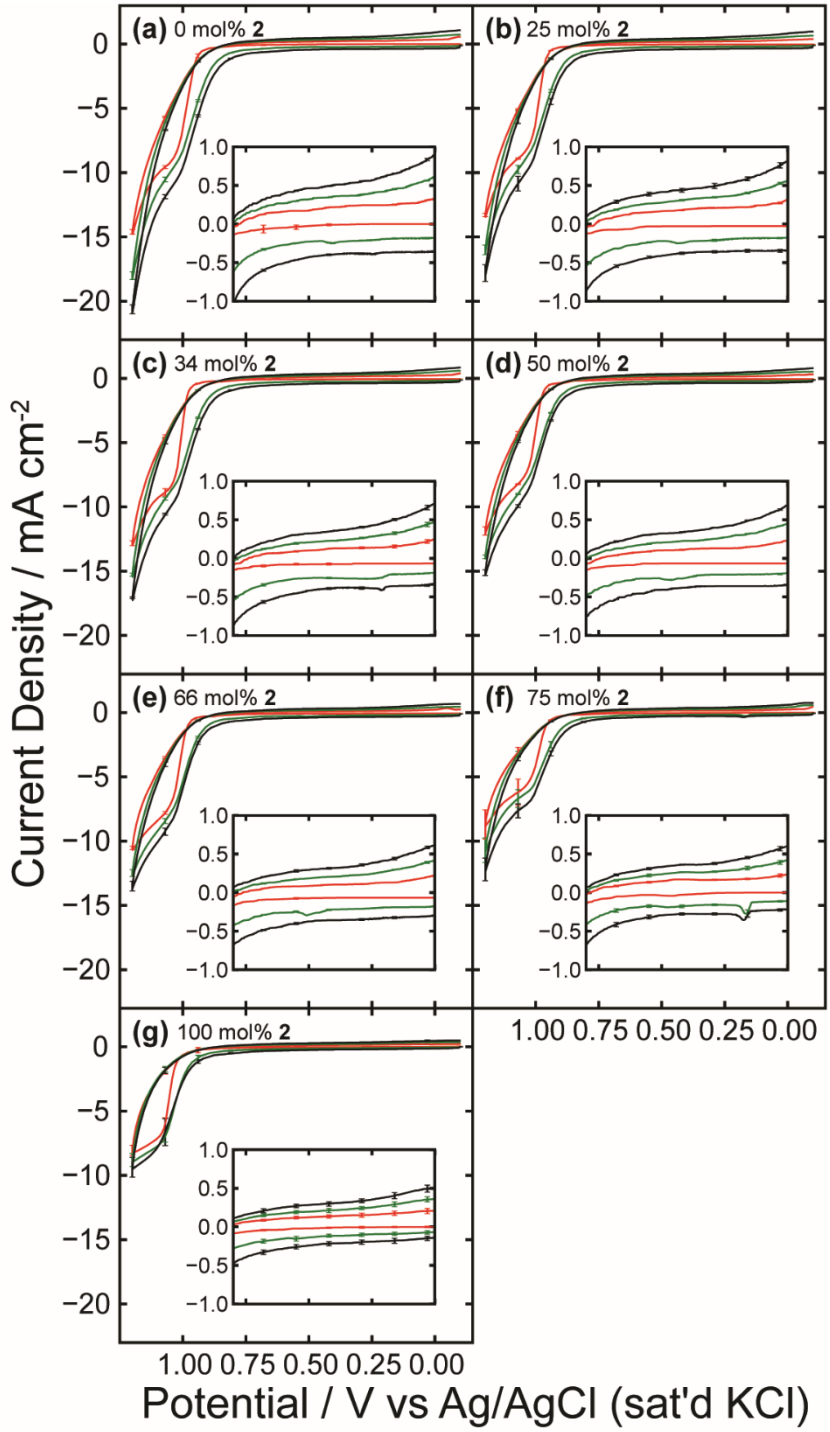

Figure 3.5. Deposition voltammograms for **(a)** 0, **(b)** 25, **(c)** 34, **(d)** 50, **(e)** 66, **(f)** 75, and **(g)** 100 mol% **2**. For each deposition solution, three electrodes on a single chip were modified by cycling a total of three times. The current for each cycle was averaged for the three modified electrodes. The first cycle is shown in red, the second green, and the third black. The standard deviation from the average is reported for ten potential values on both forward and reverse sweeps of each cycle. For all mol% **2** N=1 for sets of depositions, except for 100 mol% **2** (N=2).

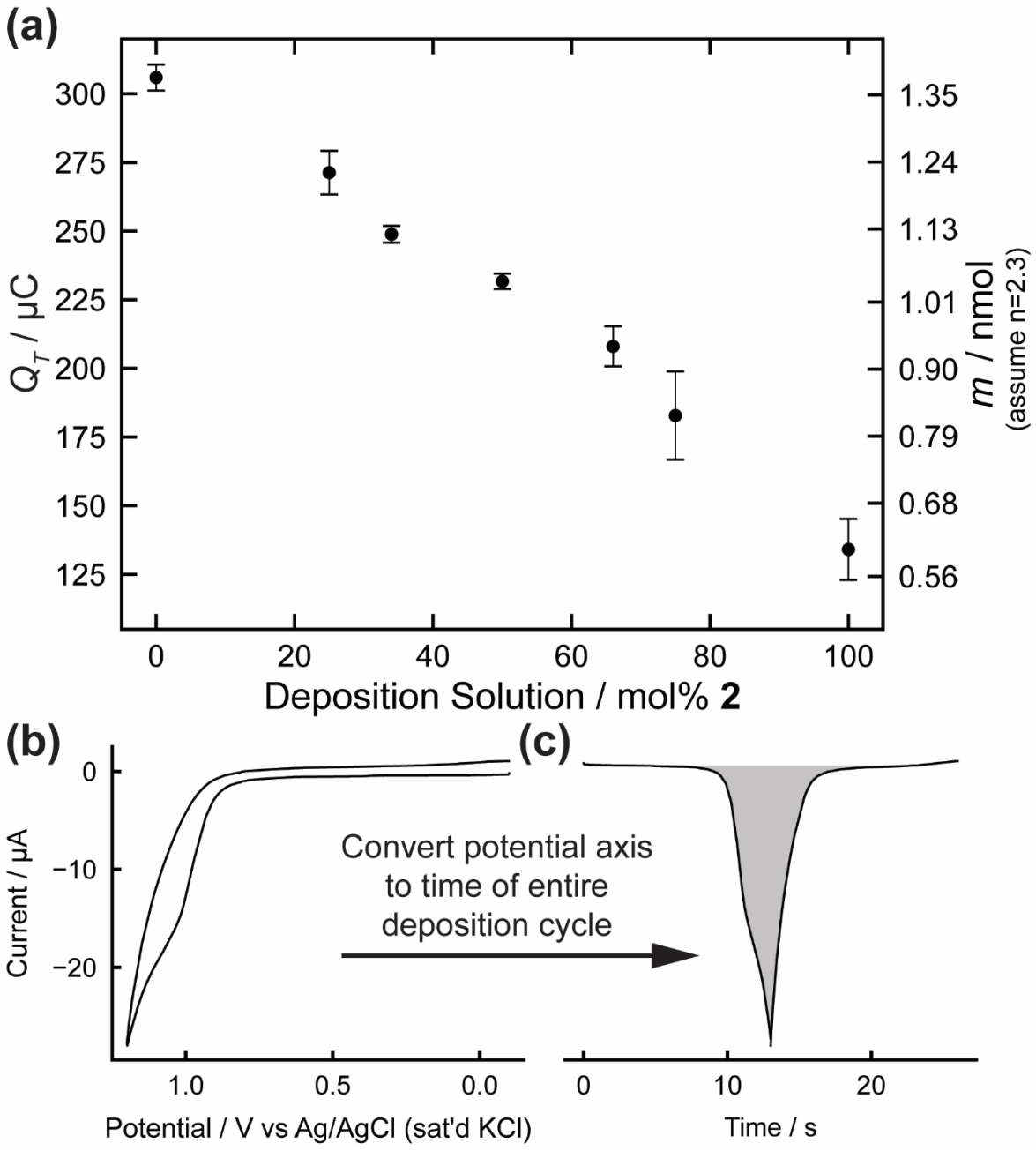

Figure 3.6. (a) Total charge passed, Q_T, during electrodeposition as a function of mol% **2** in deposition solution. As the mol% **2** increases from 0 to 100, Q_T decreases. The amount of monomer deposited, *m*, was calculated using a conversion factor of n = 2.3 moles of electrons per mole of monomer electropolymerized. Q_T was calculated by integrating and adding the three deposition voltammograms. The integration procedure involves converting the potential axis to time of the entire deposition cycle as shown in **(b)** and **(c)**. A least squares linear fit produces the following equations: for points from 0 to 75 mol% **2**, Q_T = (-1.58 ± 0.08 µC mol% $\mathbf{2}^{-1}$) $x_{mol\%\ 2}$ + 310 ± 4 µC; for all points 0 to 100 mol% **2**, Q_T = (-1.69 ± 0.08 µC mol% $\mathbf{2}^{-1}$) $x_{mol\%\ 2}$ + 310 ± 5 µC.

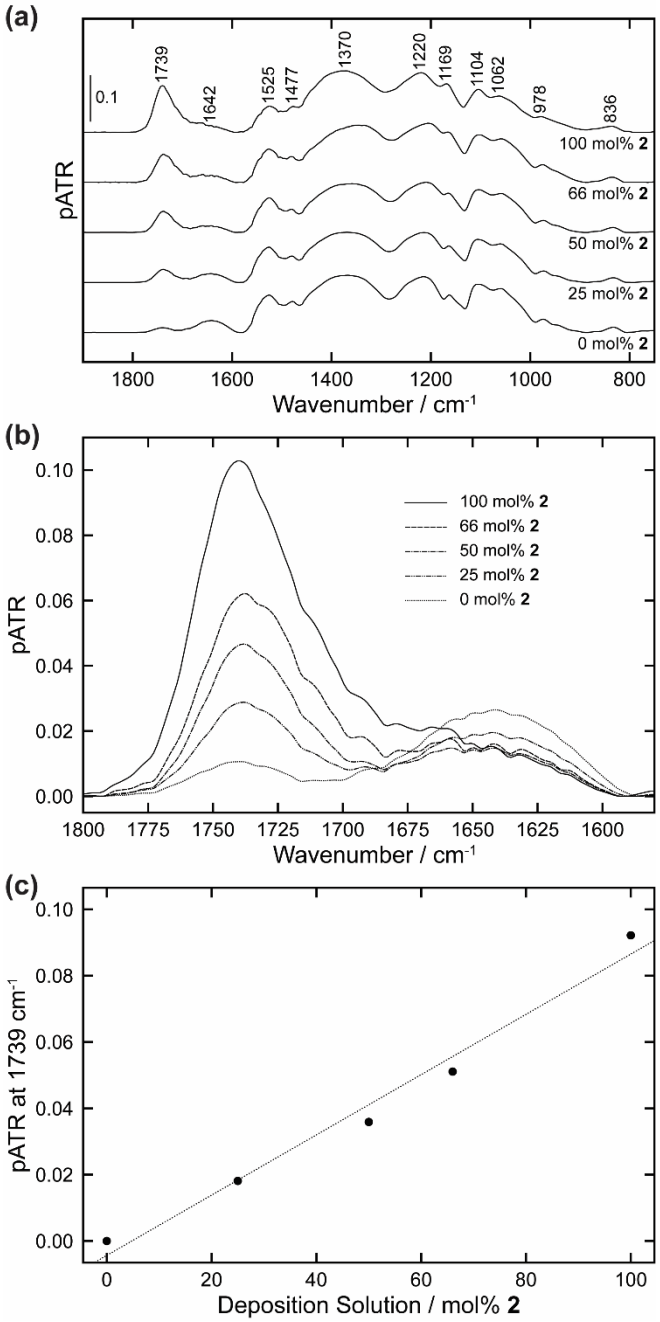

Figure 3.7. (a) μATR-FTIR spectra of polymer films on gold microelectrodes following electrodeposition from solutions containing a total monomer concentration of 0.02 M in a solution containing 0.1 M $LiClO_4$ and 0.05 M SDS. The mol% **2** in the deposition solution is indicated directly below each spectrum. **(b)** Segments between 1800 – 1580 cm^{-1} from the spectra shown in **(a)** are overlaid to highlight the relative intensity changes in the ester C=O stretching (1739 cm^{-1}) and water H-O-H bending (1642 cm^{-1}) peaks. The solid and dashed lines indicate the mol% **2** present in the deposition solution during film preparation. **(c)** Plot of background corrected $pATR_{1739}$ versus the deposition solution mol% **2**. $pATR_{1739} = (9.1\times10^{-4} \pm 0.7\times10^{-4}$ mol% $\mathbf{2}^{-1})$ $x_{\text{mol\% }\mathbf{2}} - 4\times10^{-3} \pm 4\times10^{-3}$ ($R^2 = 0.9800$).

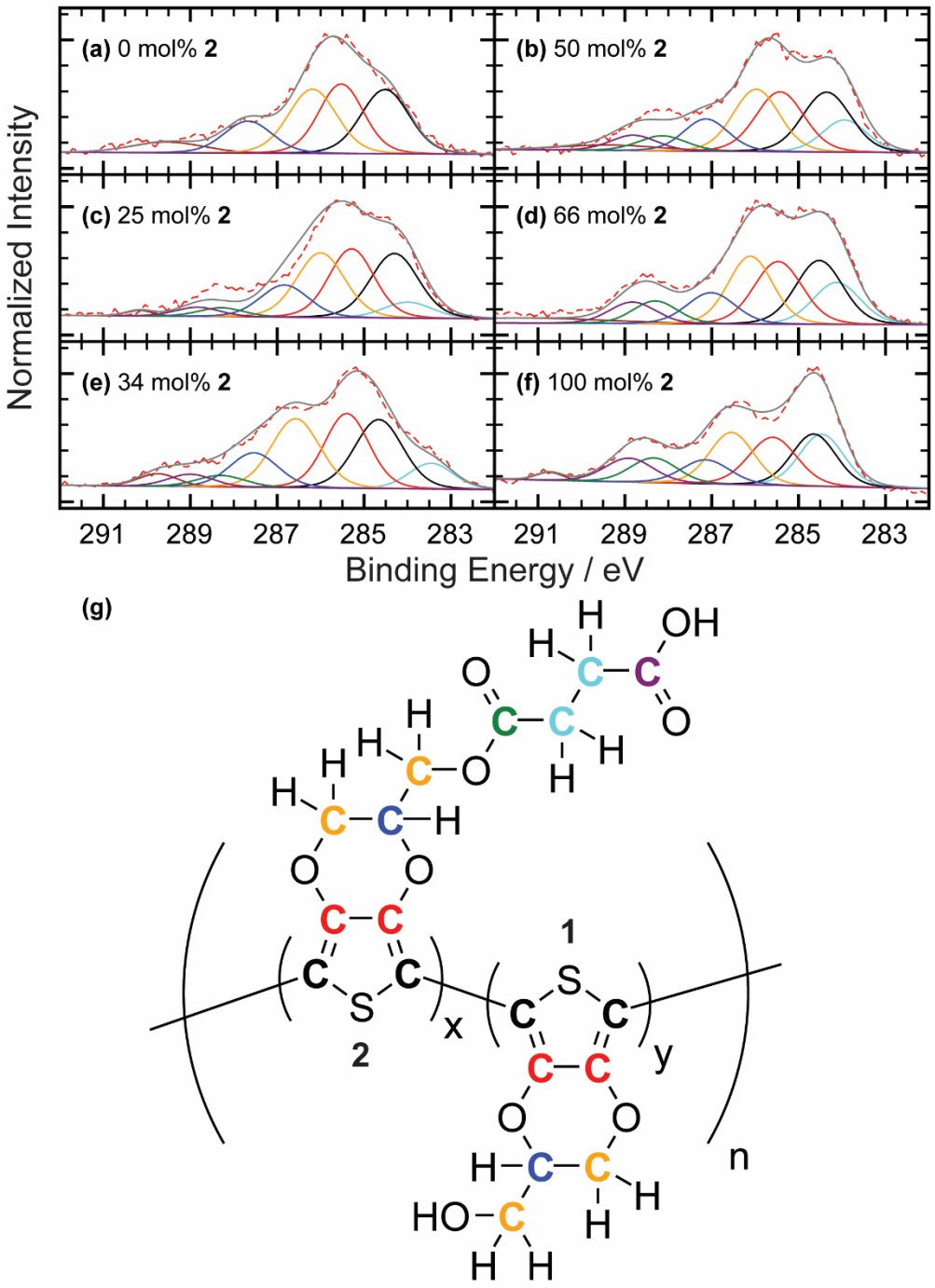

Figure 3.8. Deconvoluted and fitted C(1s) XPS spectra for **(a)** 0, **(b)** 50, **(c)** 25, **(d)** 66, **(e)** 34, and **(f)** 100 mol% **2**films. The raw XPS data is the red dotted line, the overall fit is the solid gray line, and each of the components in the deconvolution corresponds to the color coded carbons shown in **(g)** for both monomers **1** and **2**. All spectra are calibrated to 284.6 eV and additional peaks not attributed to carbon content of the monomers is due to π-π* shake-up. As the carbonyl content of the deposition solution increases the cps around 289 eV increases, which is directly related to the ester and carbonyl content of the films.

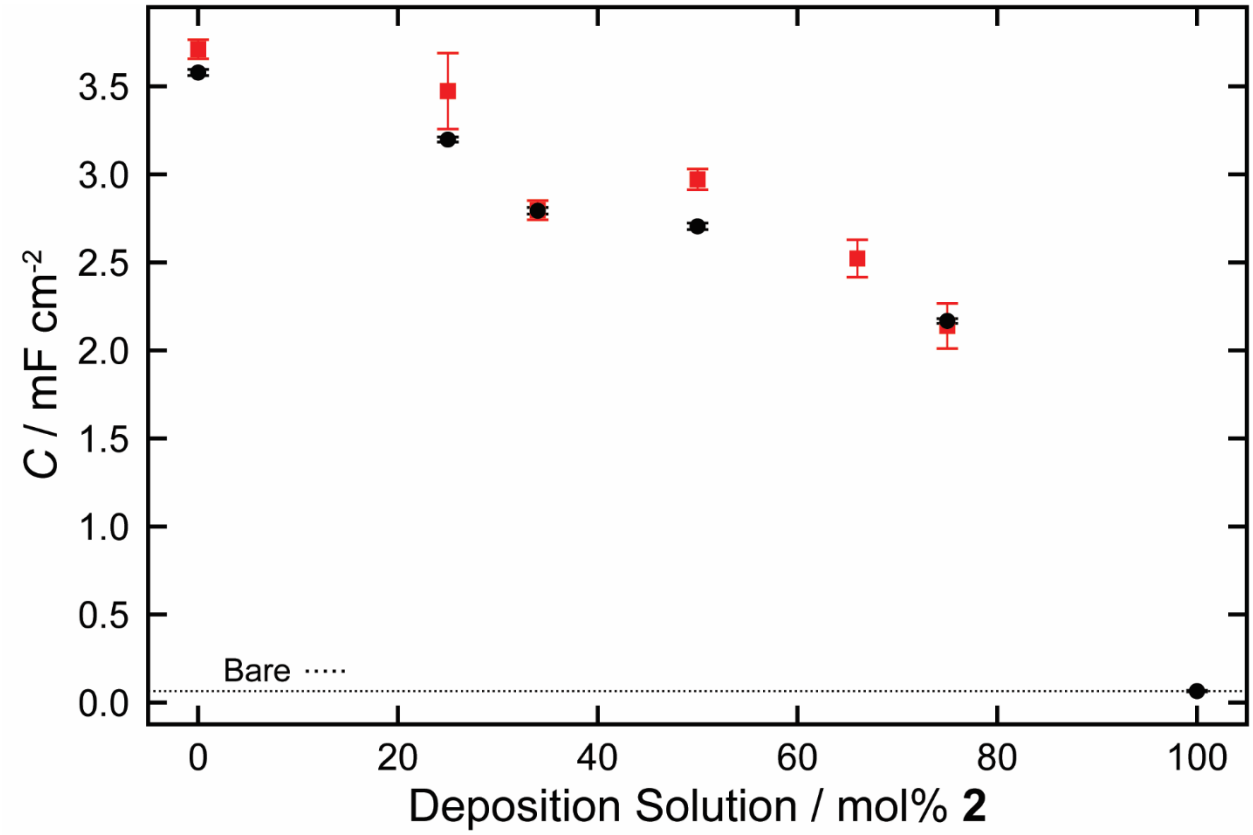

Figure 3.9. Capacitance, *C*, of films calculated using Equation 1 from the background charging current determined by CV in two sets of studies: (●) at 0.4 V in 0.2 M sodium phosphate buffer, pH 6.5, and (■) at 0.0 V in a solution containing both 0.001 M $K_4Fe(CN)_6$ and 0.2 M sodium phosphate buffer, pH 6.5. The dotted line is shown for bare electrodes as a reference of the capacitance before electrodeposition in the 0.2 M sodium phosphate buffer, pH 6.5. A least squares linear fit produces the following equation for points from 0 to 75 mol% **2**, $C = (-1.9\times10^{-2} \pm 2\times10^{-3}$ mF cm^{-2} mol% **2**$^{-1}$) $x_{\text{mol\% 2}} + 3.67 \pm 0.10$ mF cm^{-2} ($R^2 = 0.9007$).

UNIVERSITY OF ARKANSAS
J. WILLIAM FULBRIGHT COLLEGE OF ARTS & SCIENCES

Department of Chemistry and Biochemistry
Chemistry 119 • 1 University of Arkansas • Fayetteville AR 72701-1201
(479) 575-4601 • (479) 575-4049 (FAX)
http://chemistry.uark.edu • cheminfo@uark.edu

July 9, 2020

To Whom It May Concern:

On behalf of members in my research group and investigators at the University of Utah and Texas Tech University who performed scientific studies with Benjamin J. Jones, I confirm that he contributed the majority of the work described in his dissertation.

Sincerely,

Ingrid Fritsch

Professor

3S. Spatially Directed Functionalization by Co-electropolymerization of Two 3,4-ethylenedioxythiophene Derivatives on Microelectrodes within an Array

Benjamin J. Jones†, Carol L. Korzeniewski‡, Jefferson H. Franco‡‡, Shelley D. Minteer‡‡, and Ingrid Fritsch†*

†Department of Chemistry and Biochemistry, University of Arkansas, Fayetteville, AR 72701

‡Department of Chemistry and Biochemistry, Texas Tech University, Lubbock, TX 79409

‡‡Department of Chemistry, University of Utah, Salt Lake City, UT 84112

3S.1 Content of Supporting Information

Supporting information includes ^{1}H NMR, ATR-FTIR, and LC-ESI-MS characterization of monomers **1** and **2**, procedure for measuring E_{onset} and fitting of XPS data, electrodeposition voltammograms, optical images of unmodified and polymer-modified gold electrodes in arrays, profilometry data, proposed electropolymerization mechanism, CV responses of polymer-modified electrodes in buffer and buffer plus ferrocyanide, plots showing monomer quantity per volume occupied by polymer and how changes in normalized *C* track normalized *m* for films containing different mol% **2**.

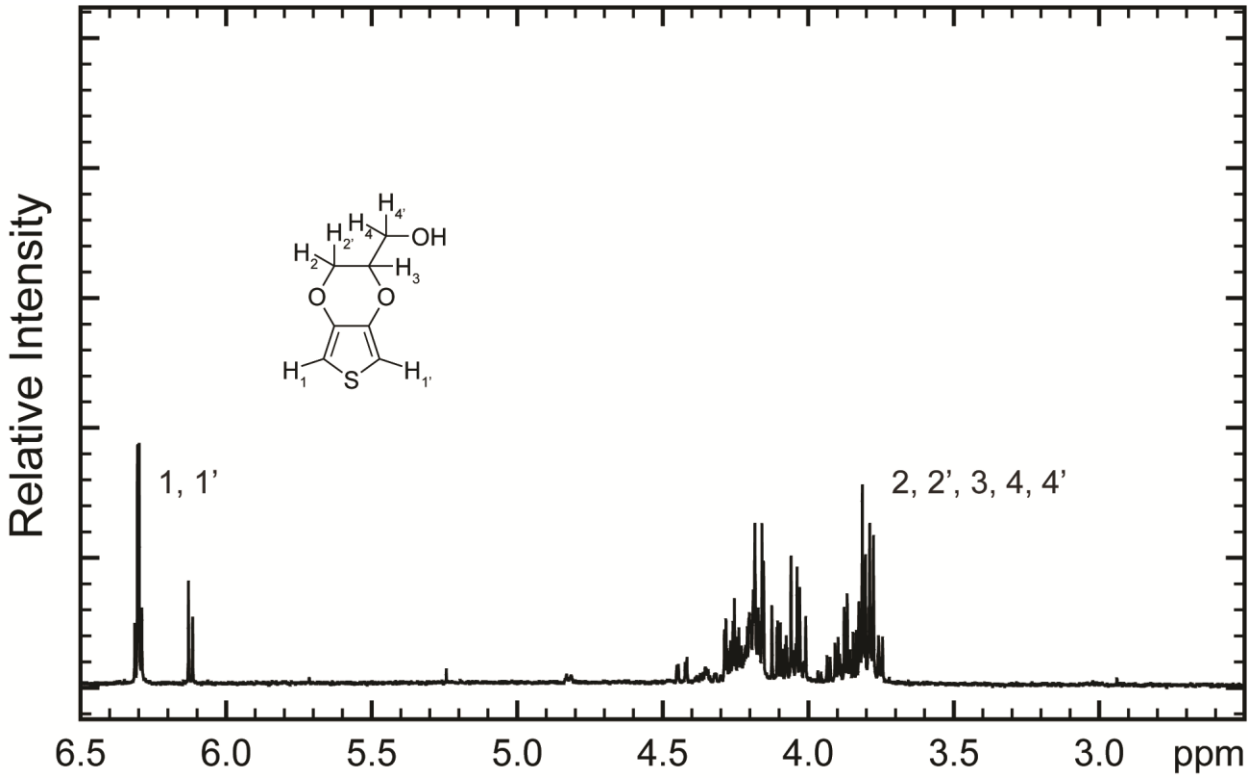

Figure 3S-1. The ^{1}H NMR (400 MHz) spectrum of monomer **1** dissolved in $CDCl_3$. This spectrum is shown to highlight the complex multiplet from δ 3.7 – 4.3, that is the result of H_2, $H_{2'}$, H_3, H_4, and $H_{4'}$. The feature at δ 6.2 is from H_1 and $H_{1'}$.

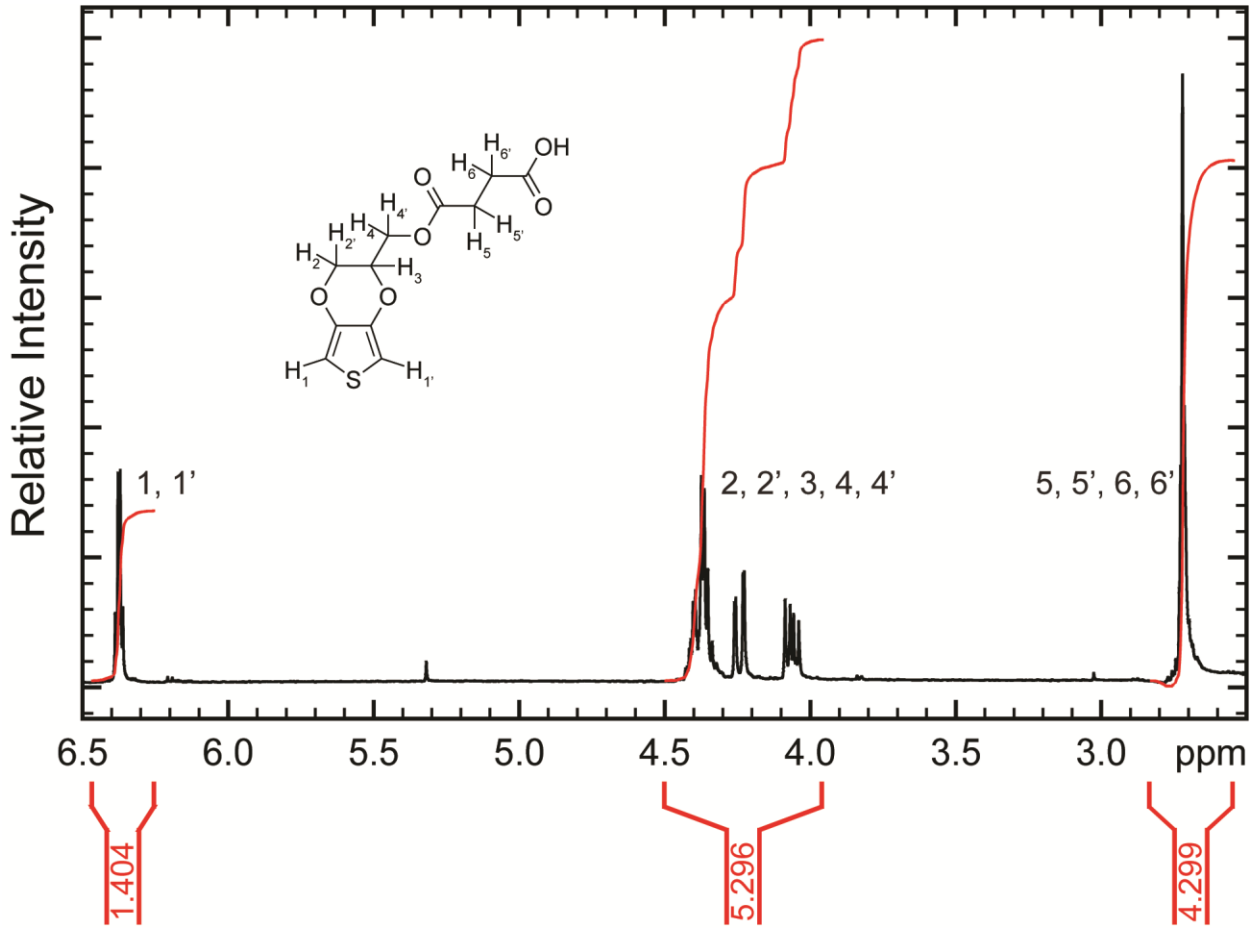

Figure 3S-2. The ^{1}H NMR (400 MHz) spectrum of monomer **2** dissolved in $CDCl_3$. The feature qualitatively identifying monomer **2** in the spectrum is the multiplet from δ 2.7 – 2.74, which is due to H_5, $H_{5'}$, H_6, and $H_{6'}$.

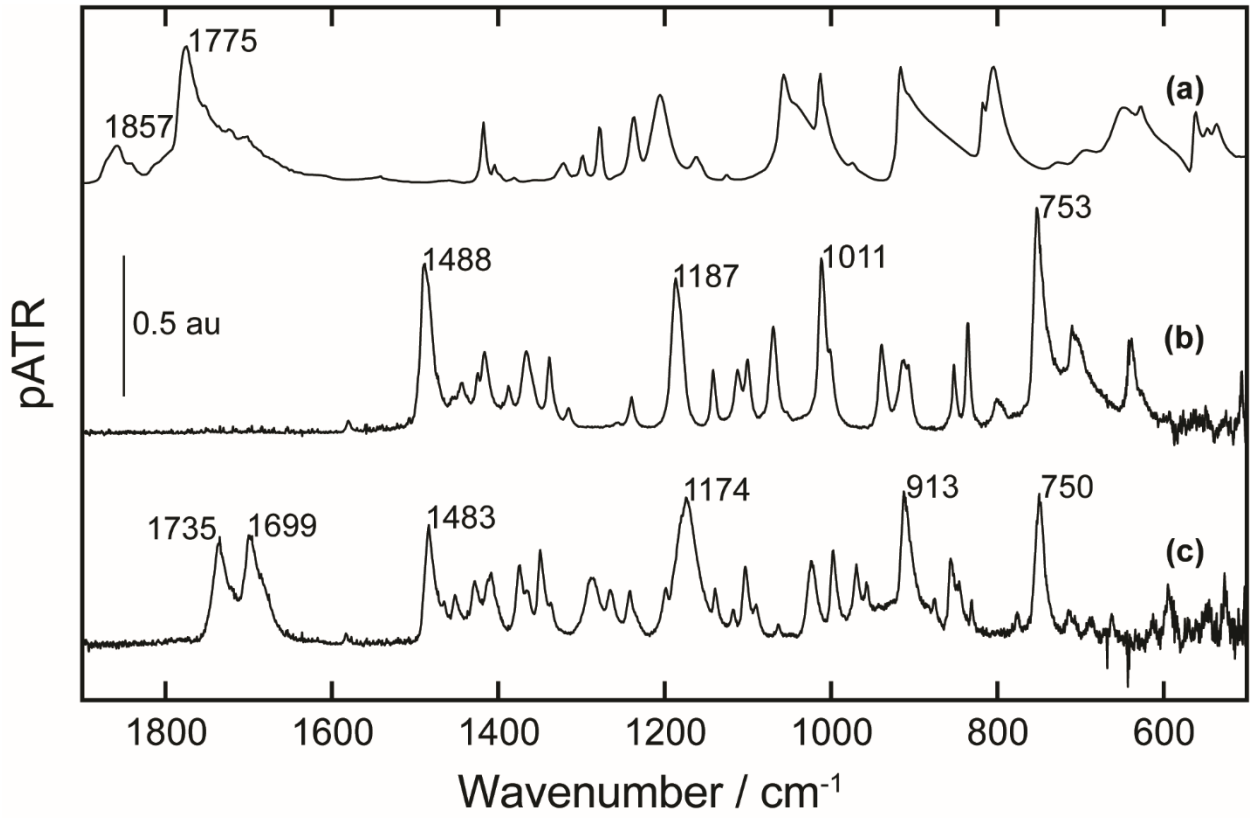

Figure 3S-3. Stacked, ATR-FTIR spectra of **(a)** SA, **(b)** monomer **1**, and **(c)** monomer **2**. Spectra of SA and the monomers were obtained using a Shimadzu (Kyoto, Japan) IRAffinity-1S spectrophotometer fitted with a Specac (Orpington, Kent, UK) Quest ATR accessory and kept on the bench at ambient conditions. Spectra were analyzed with Shimadzu LabSolutions IR software. Prior to, and between measurements, the ATR puck and crystal were cleaned with acetone and enough time was given for them to fully dry. The interferogram of SA was recorded at 4 cm^{-1} resolution with 64 scans averaged and processed using the Happ-Genzel apodization before Fourier transformation. Interferograms of monomers **1** and **2** were recorded at 0.5 cm^{-1} resolution with 40 scans averaged and processed using triangular apodization before Fourier transformation.

3S.2 Liquid Chromatography-Electrospray-Mass Spectrometry of Monomers 1 and 2.

A Shimadzu 8040 triple quadrupole mass spectrometer interfaced with an ultra performance liquid chromatography (UPLC) system and equipped with an electrospray ionization (ESI) source was used to generate spectra of monomers **1** and **2**. The Shimadzu C18 (50 × 4.6 mm, 3 μm particle size) column was kept at 40 ˚C. Samples were prepared for analysis by dissolving approximately 1 mg in a 9:1 v/v MeCN:H_2O solution. All sample volumes were 1 μL and the flow was kept at 0.5 mL min^{-1}. A solvent program consisting of LC-MS grade H_2O and MeCN with 0.1% formic acid were used. In the case of monomer **1**, the solvent program consisted of 10% MeCN for 3 min, a ramp up to 90% MeCN from 3-13 min, held at 90% MeCN for 1 min, and finally brought back to 10% MeCN to clean and equilibrate the column. In the case of monomer **2**, the solvent program consisted of 10% MeCN for 1 min, a ramp up to 80% MeCN from 1-8 min, held for 1 min, and finally brought back to 10% MeCN to clean and equilibrate the column. The desolvation line was kept at 250 ˚C and N_2 was used as the drying (18 L min^{-1}) and nebulizing (3 L min^{-1}) gas. A Q3 scan was used, where the first three quadrupoles are used as ion guides and the last quadrupole is scanned to obtain the spectrum, in positive ion mode. Each scan was 1 s and repeated throughout the entirety of the LC run. For monomer **1** the Q3 was scanned from m/z 140 – 800 and for monomer **2** from m/z 150 – 700.

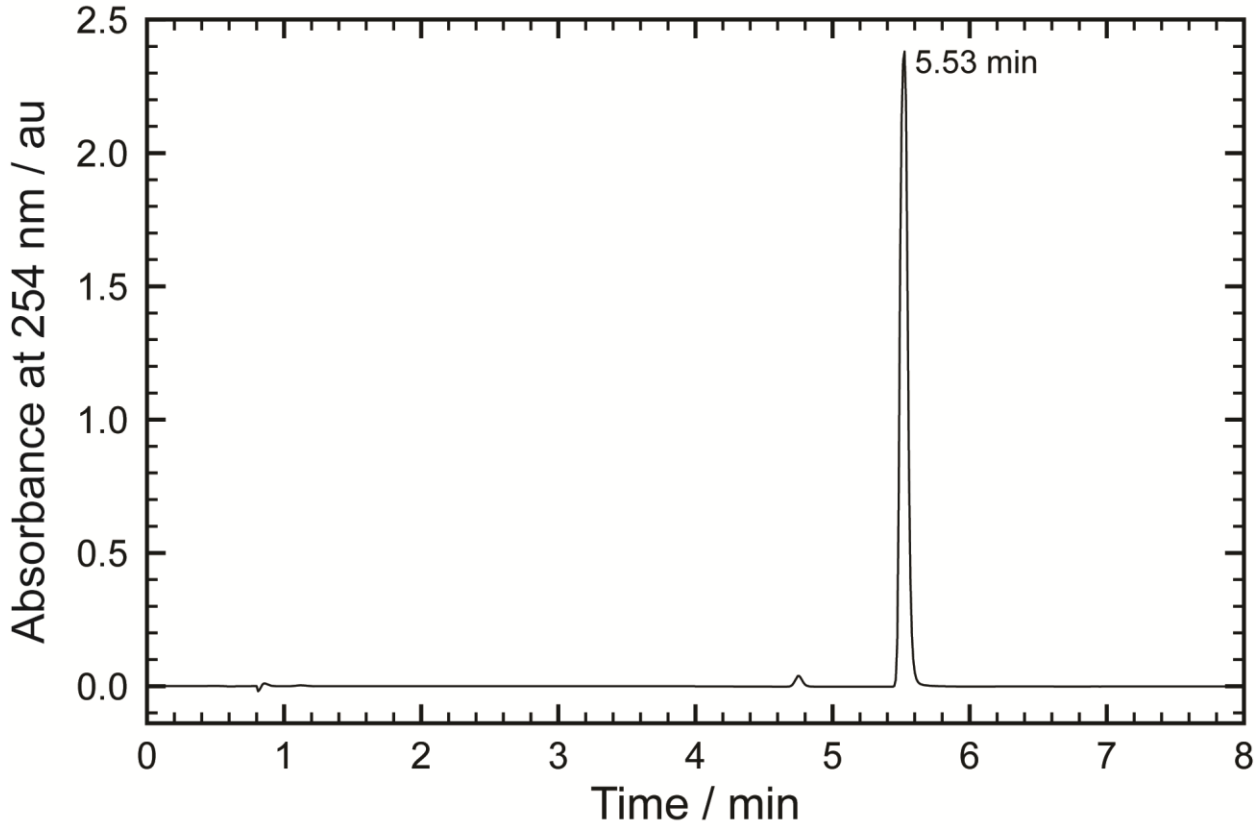

Figure 3S-4. Liquid chromatogram of monomer **1** (as received) in a 9:1 v/v MeCN:H_2O solution.

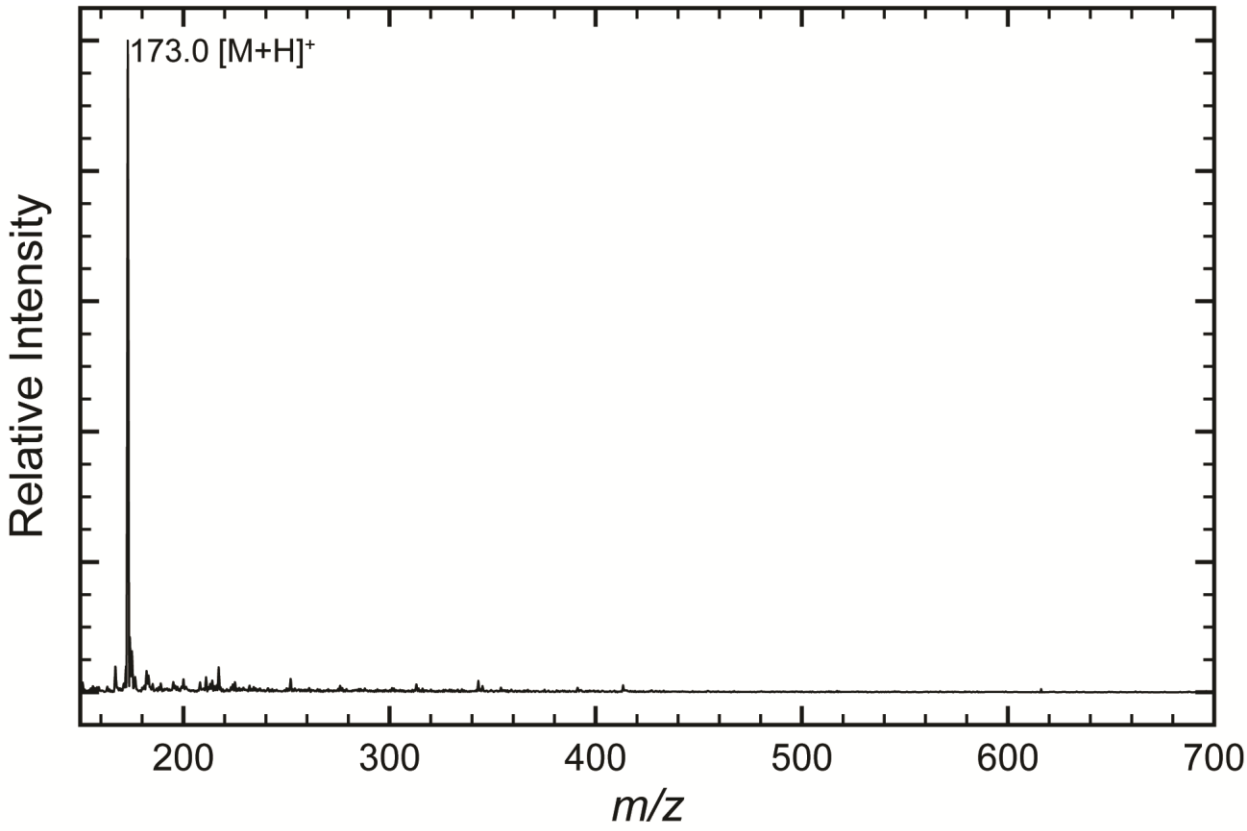

Figure 3S-5. Mass spectrum of the peak at 5.53 min in the chromatogram of Figure 3.S-4. The base peak of the spectrum corresponds to the calculated protonated monomer **1** (m/z 173.0).

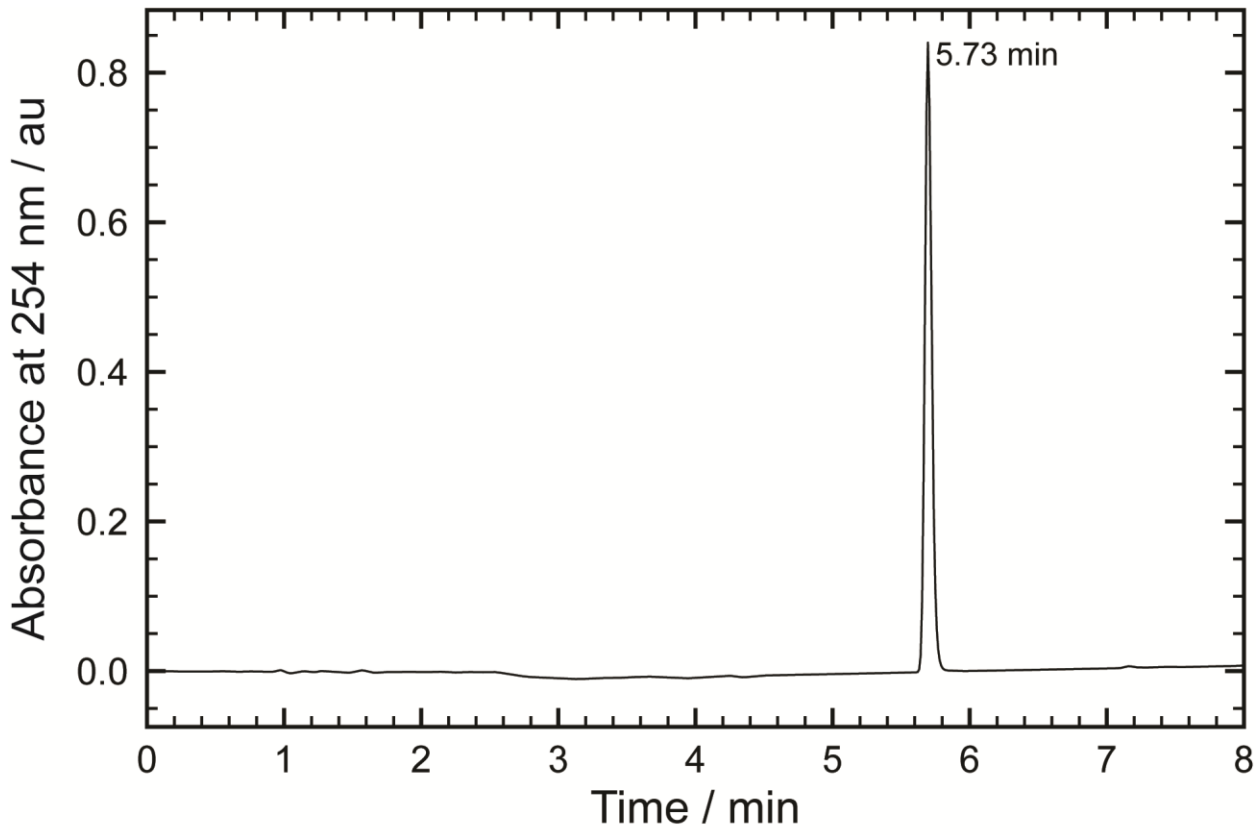

Figure 3S-6. Liquid chromatogram of monomer **2** in a 9:1 v/v MeCN:H_2O solution.

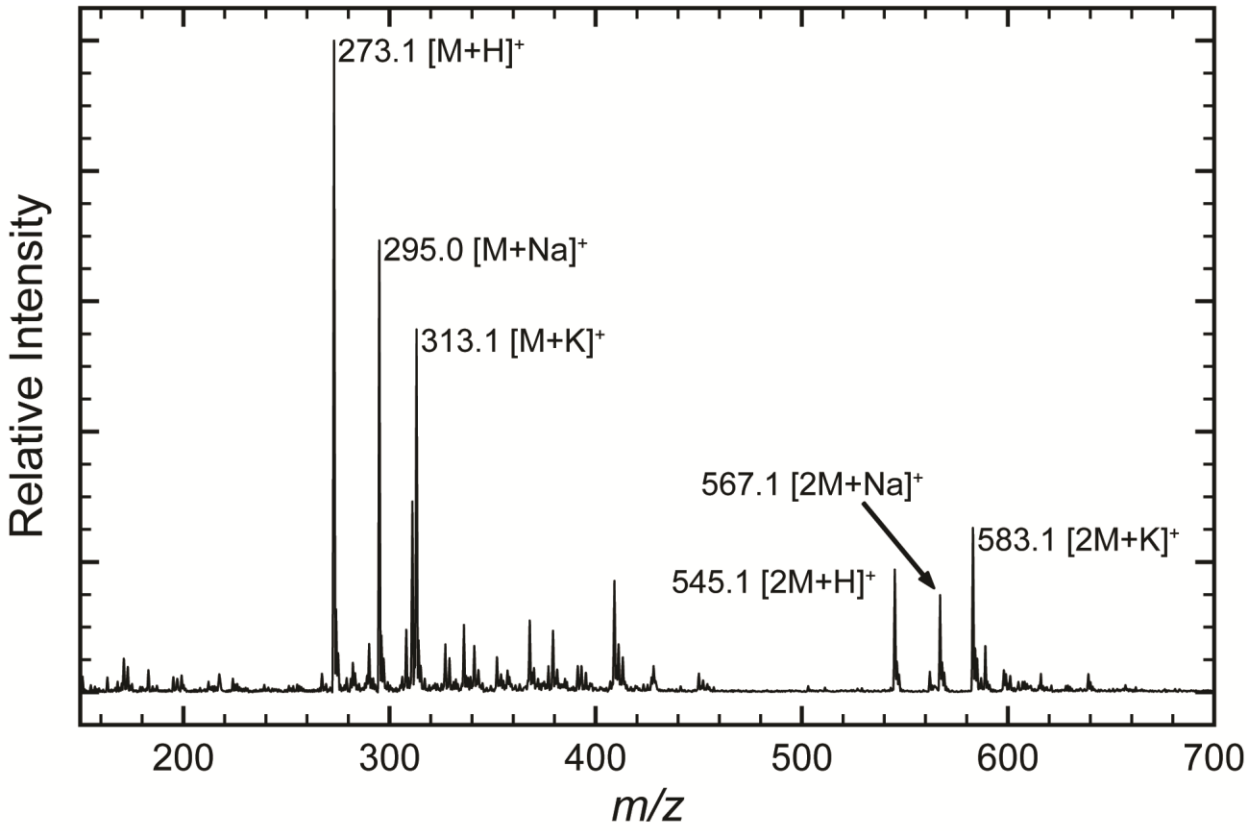

Figure 3S-7. The mass spectrum of the peak at 5.73 min in the chromatogram of Figure 3.S-6. The base peak of the spectrum corresponds to the calculated protonated monomer **2** (m/z 273.1). There are a series of additional peaks that are sodiated and potassiated monomers and dimers of **2** that result from the ionization source.

3S.3 Determination of E_{onset}.

Two commonly used methods to determine E_{onset} are using the potential value between two peaks or plateaus and the other is finding the potential at which the current deviates from the background by a given percent. These methods are suitable when two resolved peaks or plateaus are present, and when there is a flat background current, respectively. In the deposition voltammograms, there were no resolved oxidation peaks before the switching potential and the background current, although relatively flat, shifted slowly enough that a percent deviation was not suitable. Neither of the common approaches are suitable for the deposition voltammograms in this work. To account for the lack of resolved oxidation peaks and flat background, a reproducible method, shown in Figure 3.S-8, was developed that uses the first derivative of the forward sweep of the deposition voltammogram.

The first step is to convert the voltammogram from a potential axis to a time axis. Then the current between 0.0 and 0.5 V can be averaged and subtracted from all current values. The next step is to generate a first derivative plot of the deposition cycle using the software accompanying the CH Instruments potentiostat. From the plot of the first derivative, the local minimum corresponding to the inflection point of the deposition can be located. The x and y position of the local minimum represent the time and slope of the inflection point, respectively. A line tangent to the inflection point can then be extrapolated to the potential value at zero current. This potential value is E_{onset}.

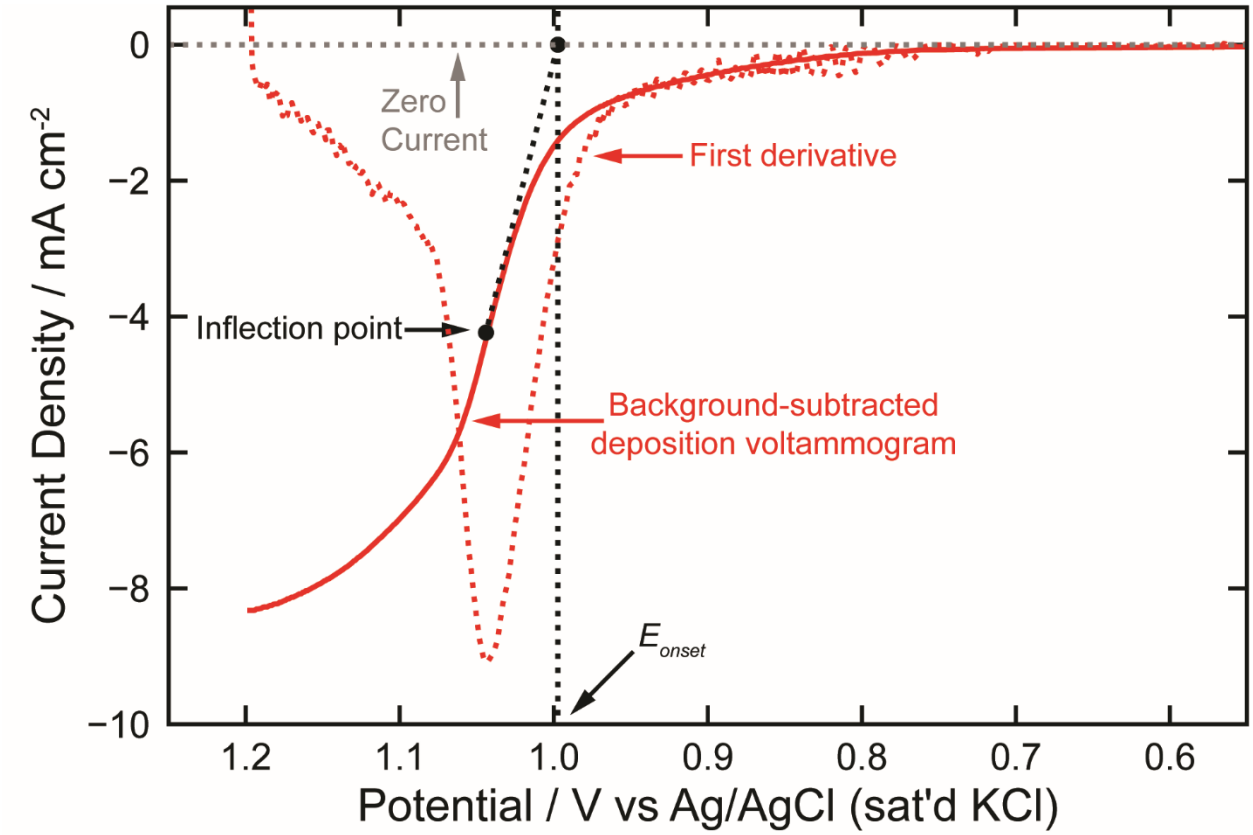

Figure 3S-8. Example of the method used to determine E_{onset} for a single, background-subtracted, deposition voltammogram.

3S.4 Deconvolution and Fitting Parameters for C(1s) XPS Results in CasaXPS.

The seven C(1s) peaks with distinctive chemical shifts in the XPS data obtained for the 100 mol% **2** film were used as the basis of comparison with the C(1s) peaks of all the films. Four of these peaks are common to both monomers and three are unique to monomer **2**. A reference value of 284.6 eV is used to shift the spectra to account for charging in the Spectrum Processing tool of CasaXPS. The C(1s) region from 280 to 296 eV was manually created using the Quantification Parameters tool. A simple linear background type was chosen under the Regions tab in the software. In the Components tab, seven regions were created, one for each type of carbon, and then the components were fit. It was necessary to create additional components to account for π-π* interactions detected in some of the spectra. This first fit is a mathematical approximation and does not reflect the chemistry, but was necessary for generating a Standard Report from the Report Spec. tab and to note the total area of the envelope, which is the summation of all the components. An estimation of the approximate area each type of carbon should occupy in the deconvolution was completed prior to the data analysis and was based on the relative amounts of each carbon present at the ratio of the monomers represented by the deposition solutions. From this estimated area the individual component peaks were adjusted. For each component, the default relative sensitivity factor (R.S.F. = 1.0) and line shape (asymmetric based on the Lorentzian functional form (LA (1.53,243))) were used. The main items that were constrained were area, full-width at half maximum (fwhm), and position. The area for each component was set to the estimated percent of total area of the envelope and constrained to ± 2 area units. The fwhm was also constrained to a range of 1.25 to 1.35. Another fit of the components based on these initial constraints was performed. Based on those results, the relative positions of the peaks were adjusted manually. The relative positions of the

components were arranged, from lowest binding energy to highest, as follows: C-C, C-S, C=C, CH_2-O, CH-O, OC=O, C=OOH. As the component relative positions were manually adjusted, they were also constrained to a ± 0.5 eV range. The adjustments and constraints were continued until the relative standard deviation of the fit was minimized. The components were copied and pasted to the other films' XPS results as a starting point. The areas were then adjusted to the theoretical percentage of the total area of the envelope and the process was repeated. When fitting the 0 mol% **2** results, the area of the C-C, OC=O, and C=OOH components were set to zero as those carbons were not considered to be in the 0 mol% **2** film.

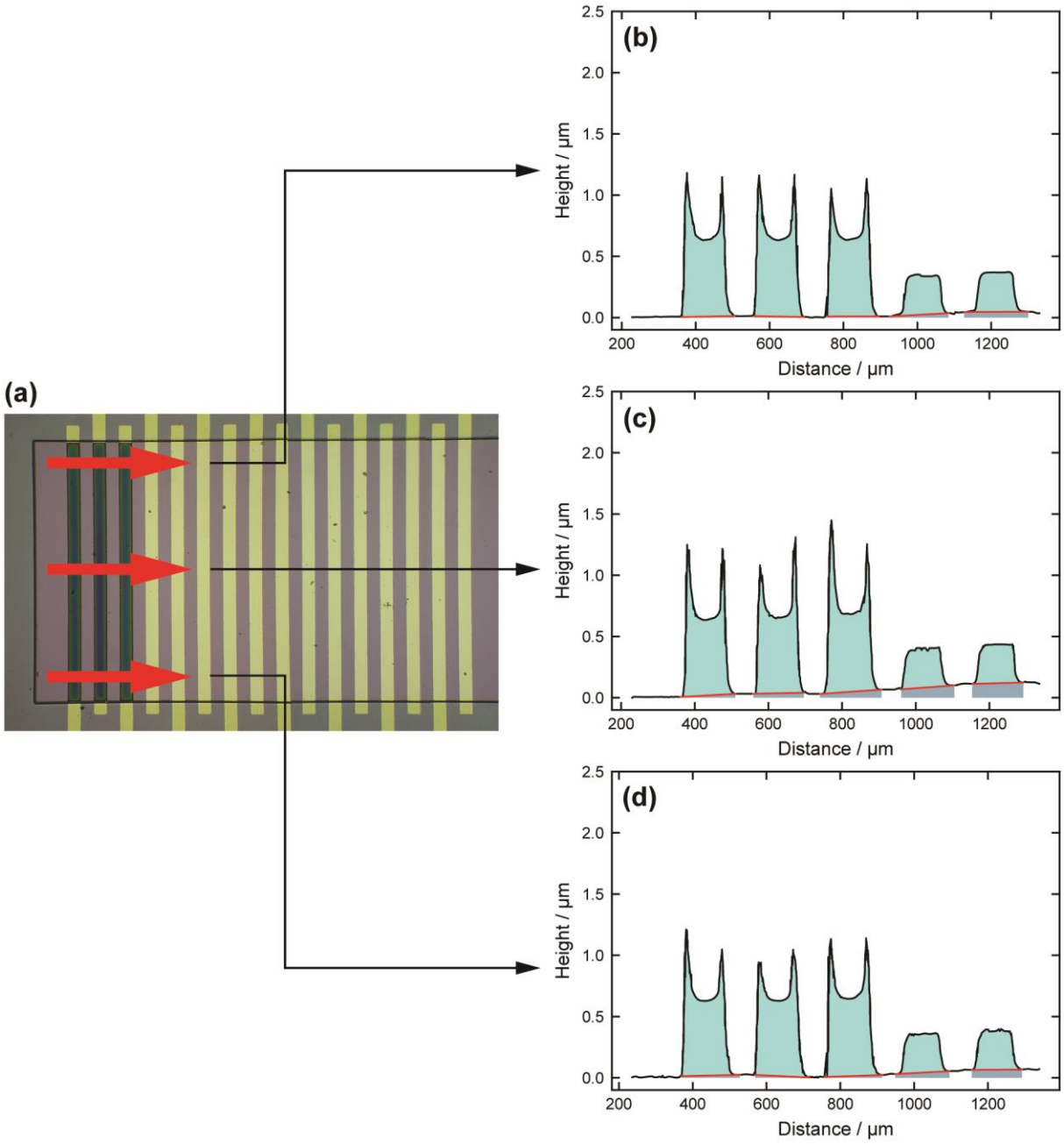

Figure 3S-9. A schematic of the profilometry measurement and the resulting height profiles for polymer films deposited from a 66 mol% **2** solution. The chip **(a)** was positioned perpendicular to the stylus's three measurement paths (red arrows). The height profiles were obtained across **(b)** one end **(c)**, the middle, and **(d)** the other end of the array. The red arrows are show the approximate position of the stylus for these three locations. The modified electrodes are the first three electrodes in each of the scans and the last two are unmodified gold electrodes. The red lines mark the approximate background of the electrode surface. Because the overall background is not completely flat, the area under the red line for each electrode (dark cyan) was subtracted from the overall area of the electrode and the background-subtracted area of the electrode is shown in cyan.

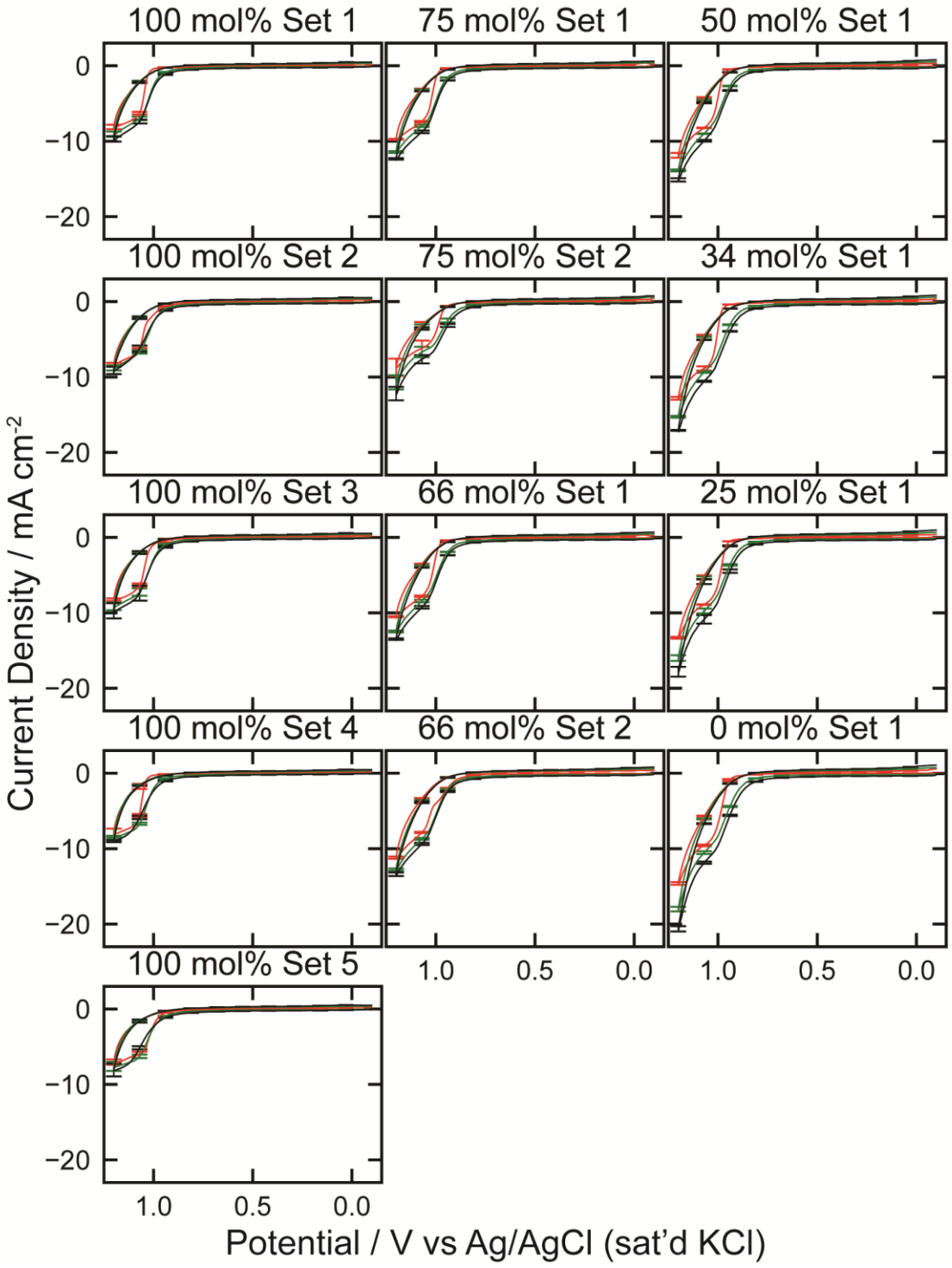

Figure 3S-10. Deposition voltammograms (0.100 V/s) for all attempts, performed in solutions containing 0.1 M SDS, 0.05 M LiClO4, and a total monomer concentration of 0.02 M. The monomer composition of the deposition solution is designated by the mol% **2**. Each voltammogram is the average of that cycle for three microelectrodes on the same chip. Error bars represent ± one standard deviation from the averaged current for each cycle and are shown for ten selected potentials in both the forward and reverse scans.

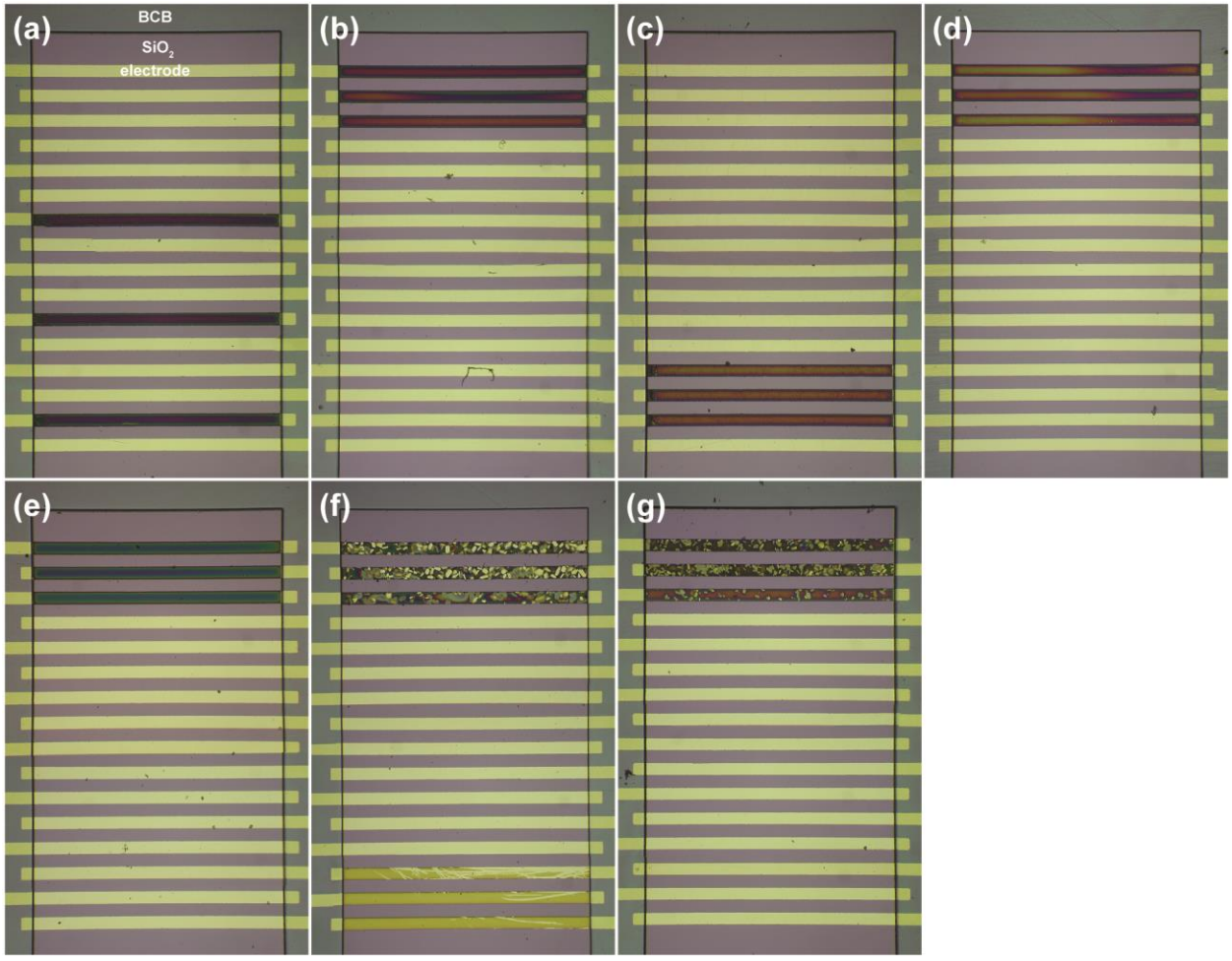

Figure 3S-11. Composite images of each array with three modified electrodes for **(a)** 0, **(b)** 25, **(c)** 34, **(d)** 50, **(e)** 66, **(f)** 75, and **(g)** 100 mol% **2**.

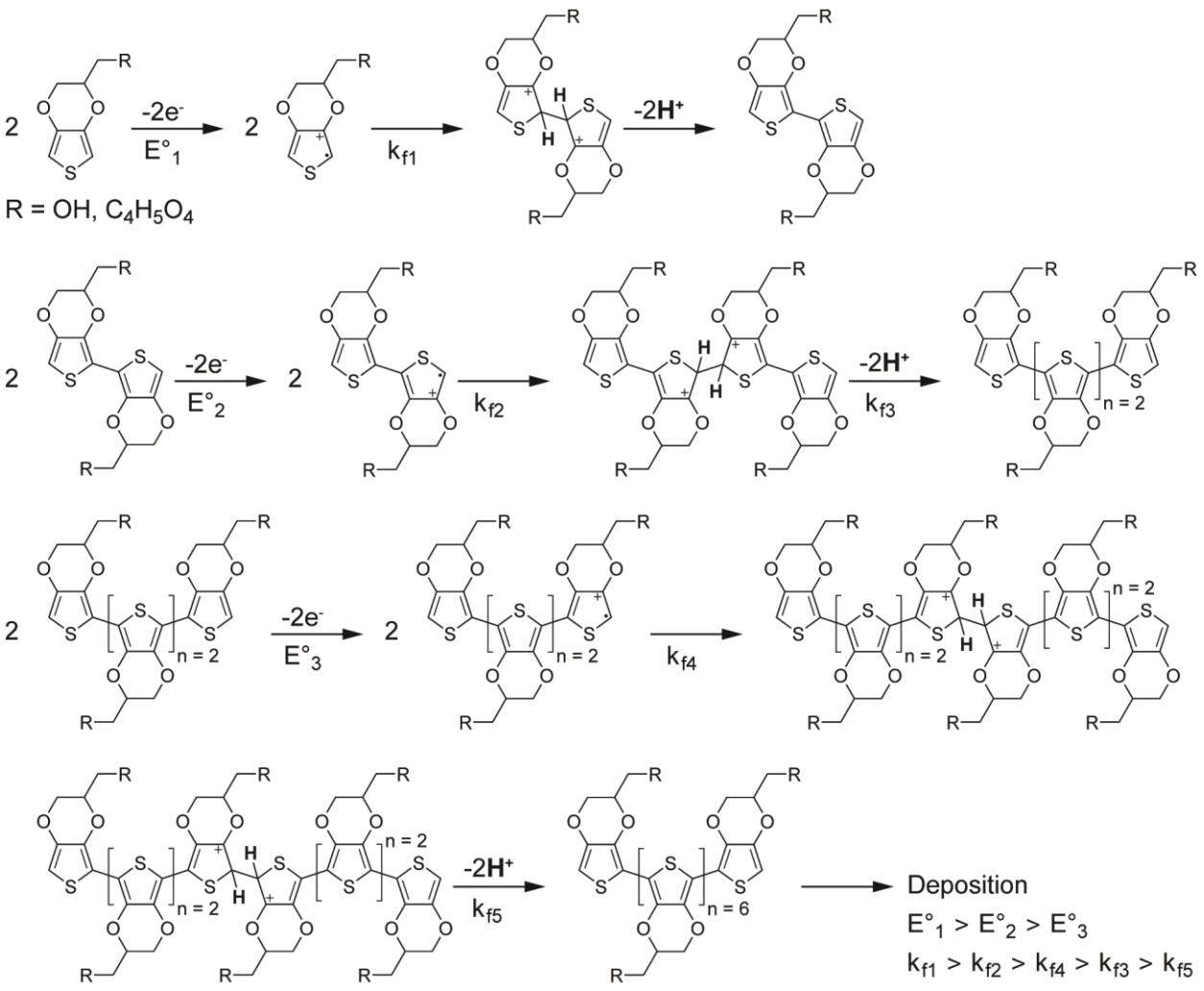

Figure 3S-12. Proposed electropolymerization mechanism of monomers **1** and **2**. The first step is oxidation of the monomer at the electrode surface resulting in a monomeric radical cation that reacts with an identical species forming the initial dimer in the diffusion layer. Successive dimerization steps continue until solubility and reactivity of the oligomers are low enough for instantaneous nucleation and 3D growth of the polymer on the electrode surface. Schematic is based on the mechanism for EDOT proposed by Heinze.[1]

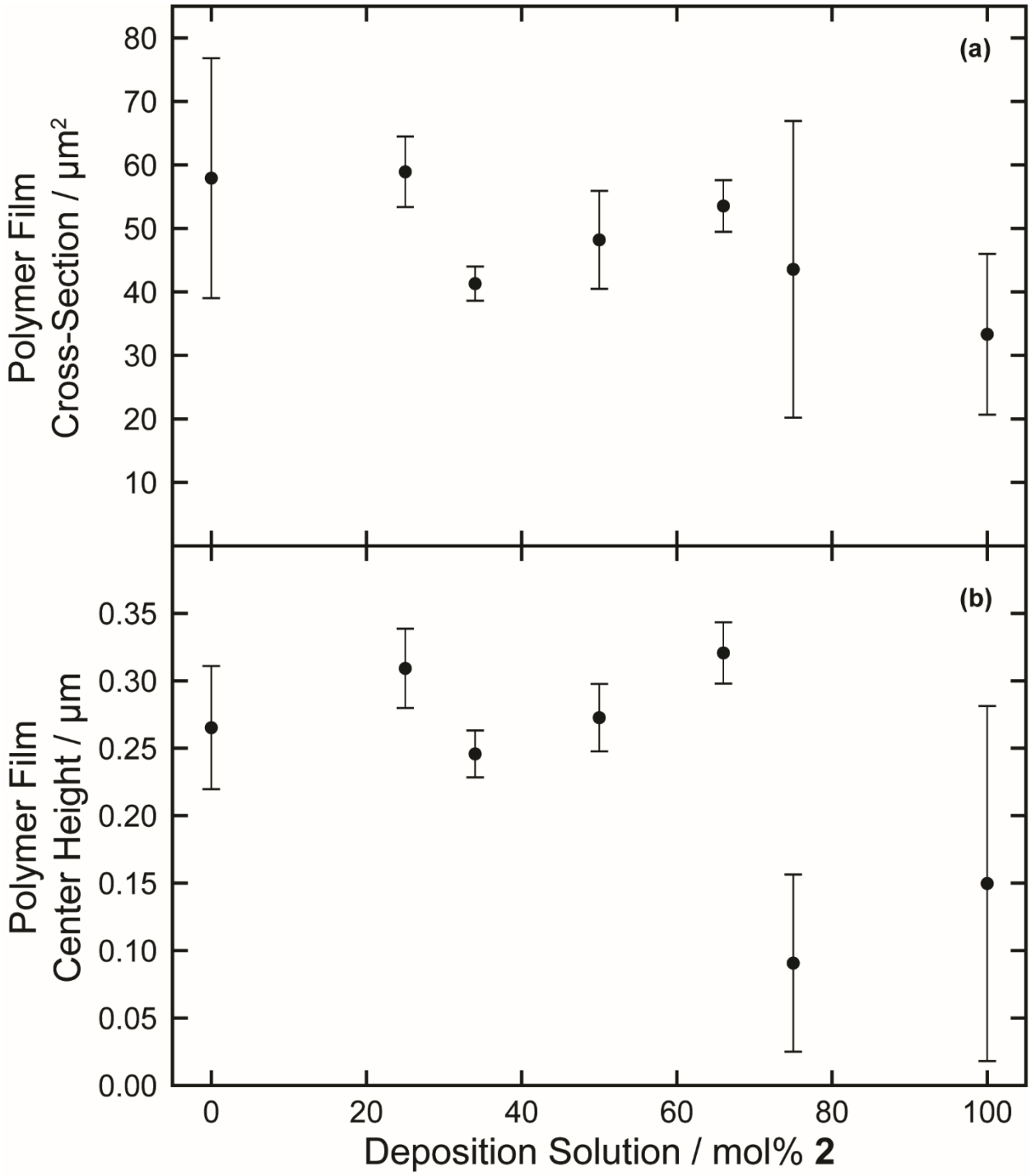

Figure 3S-13. Profilometry measurements yielding **(a)** cross sectional area and **(b)** height for polymer films formed from solutions of different mol% **2**.

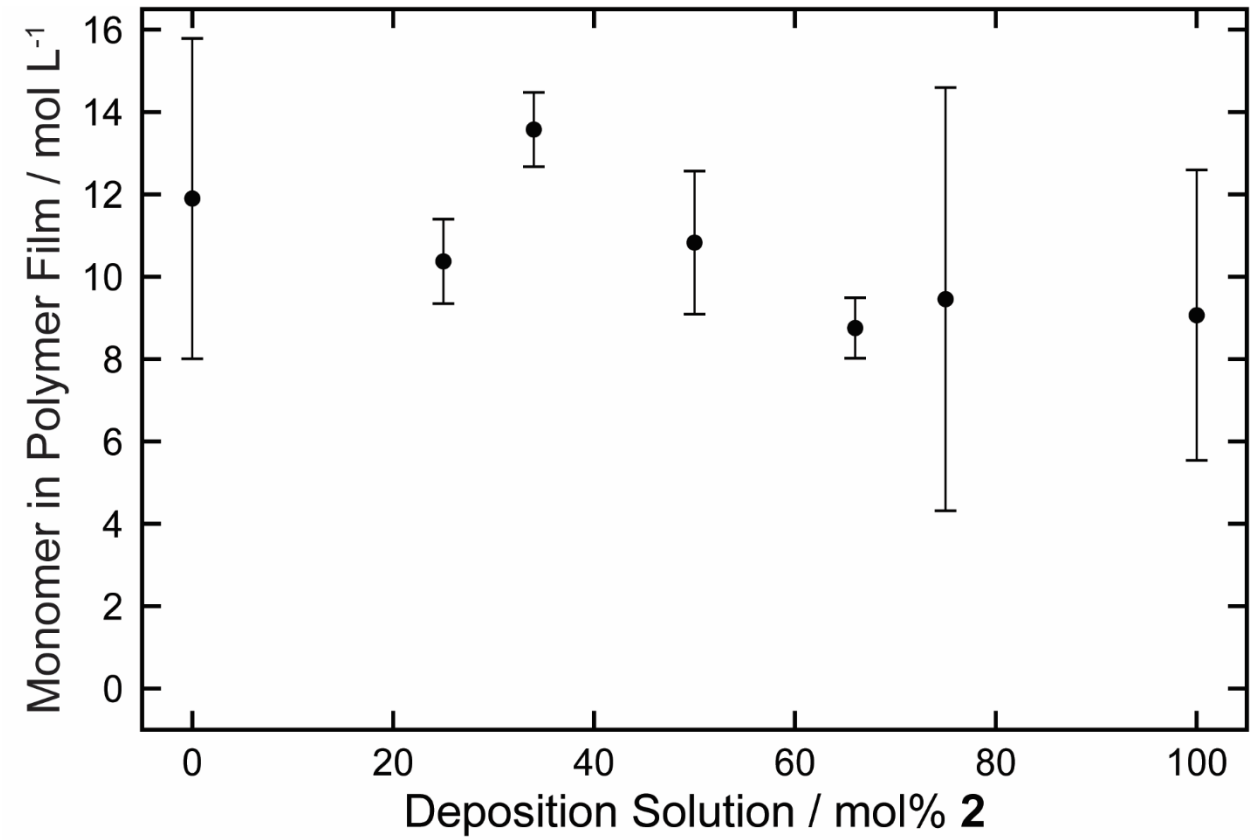

Figure 3S-14. The amount of monomer deposited in the volume occupied by the polymer films formed from solutions of different mol% **2**. The amount of monomer deposited was determined by integration of deposition voltammograms and the volume was obtained from the measured cross-sectional areas of the films and the known length of the electrodes. Error bars represent ± the propagated uncertainty.

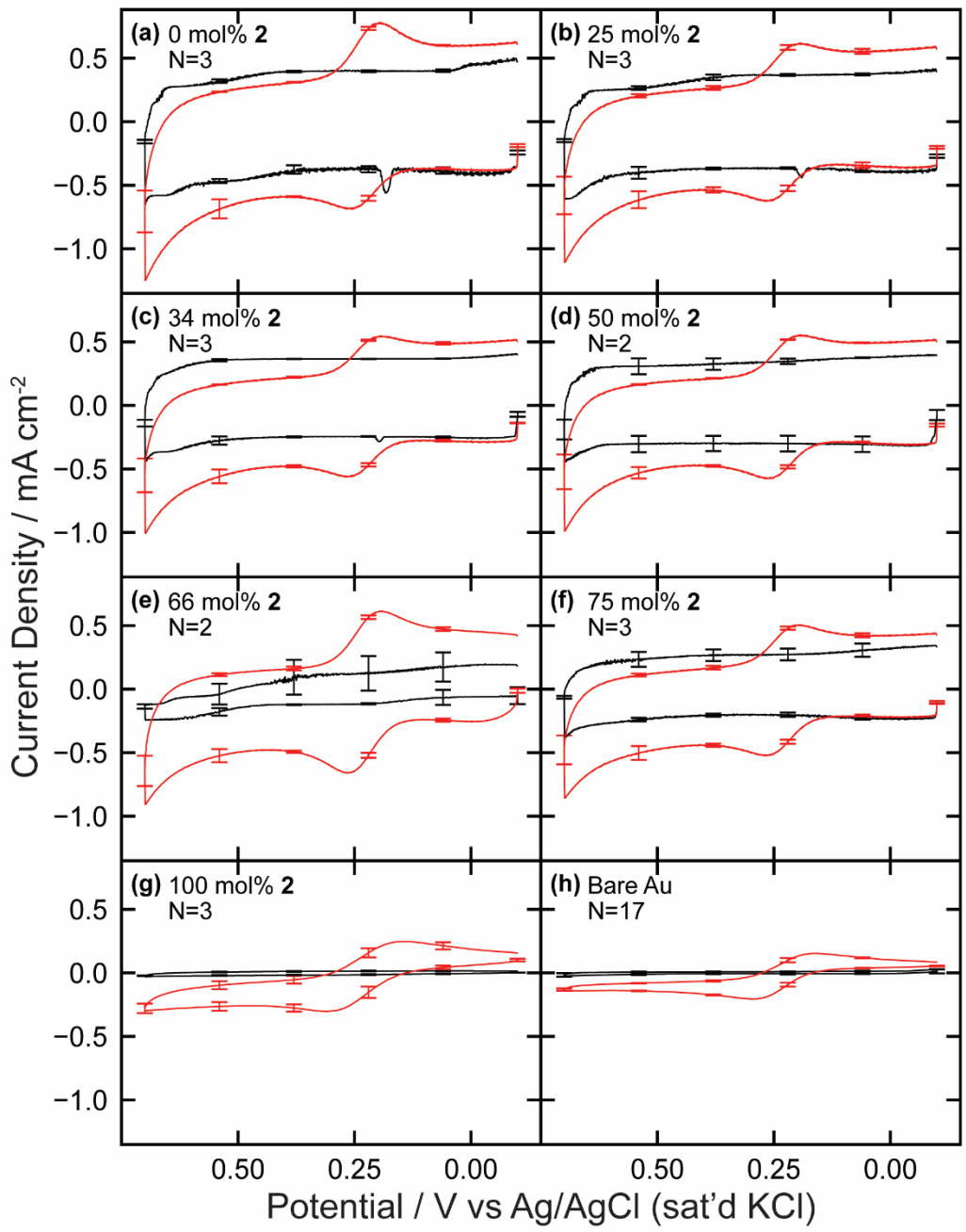

Figure 3S-15. Averaged, electrode area-normalized CV responses (0.100 V s^{-1}) of polymer-modified microbands (N = number of electrodes) in arrays in 0.2 M sodium phosphate buffer, pH 6.5 (black curves) and 0.2 M sodium phosphate buffer containing 0.001 M $K_4Fe(CN)_6$, pH 6.5 (red curves). Error bars represent ± one standard deviation obtained at the selected potentials shown. Two methods using these two sets of CV responses were used to obtain the capacitance values reported in Table 2 of the main document. The first method involved measuring the current difference between the forward and reverse sweeps at 0.4 V for the scans in the phosphate buffer alone (black), The second entailed taking the difference between 0 mA cm^{-2} and the current value at 0.0 V for the scans in the solution containing both $Fe(CN)_6^{4-}$ and the phosphate buffer (red).

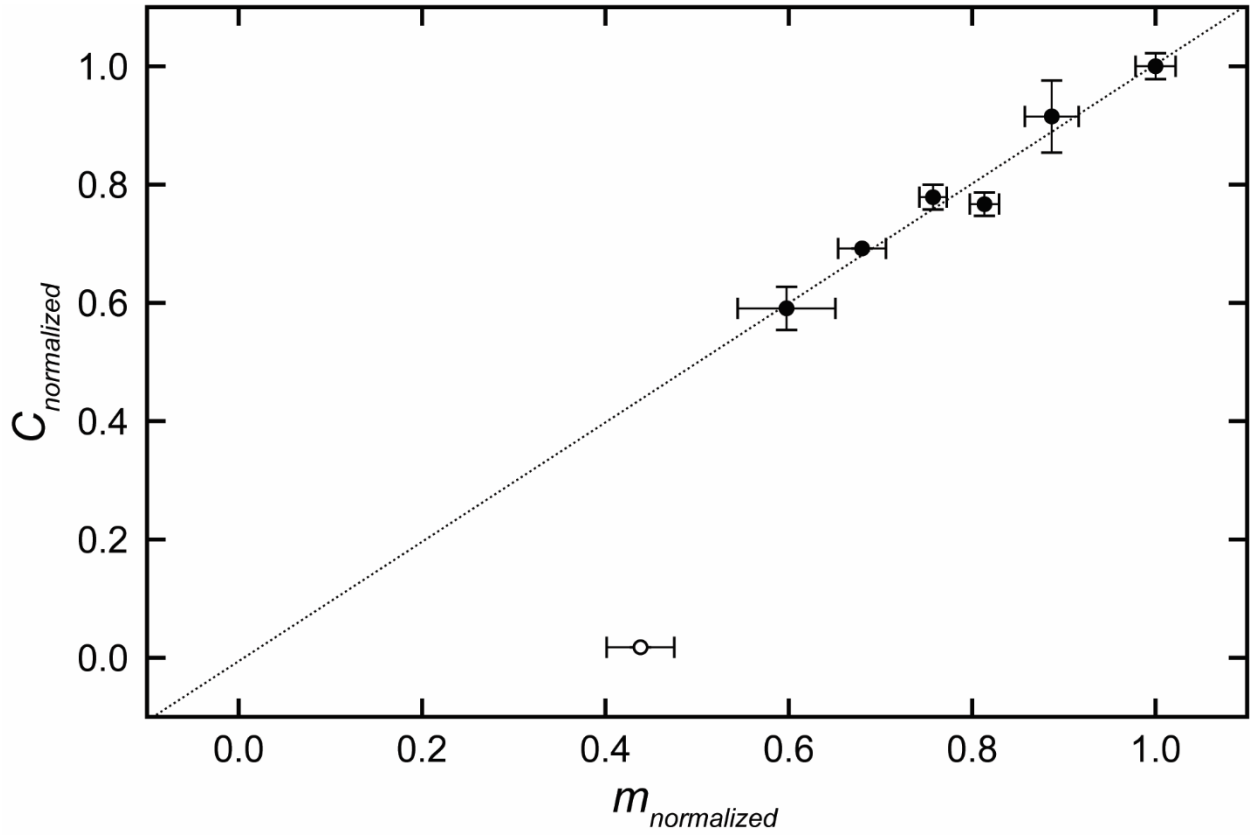

Figure 3S-16. An assessment of how much polymer film capacitance (*C*) depends on the numbers of monomers deposited during film formation (*m*) from each of the seven different solution compositions. *C* and *m* are normalized to the largest *C* and *m*, respectively, measured for films formed from 0 mol% **2**. The normalization allows direct comparison of whether changes in capacitance are simply proportional to the quantity of polymer (expecting a linear relationship) or more influenced by the relative composition of **2:1** in the polymer (expecting a nonlinear relationship). The (●) values are for films formed from deposition solutions of 0 – 75 mol% **2** (from right to left), and the (○) values are for the 100 mol% **2** film (leftmost point, not included in least squares fit). The equation of the resulting line (for points 0 to 75 mol% **2** is: $C_{normalized}$ = (1.01 ± 0.09 $C_{normalized}$ $m_{normalized}^{-1}$) $x_{m_{normalized}}$ – 0.01 ± 0.07 $C_{normalized}$ (R^2 = 0.9672). Error bars represent ± the propagated uncertainty.

3S.5 References

1. J. Heinze, B. A. Frontana-Uribe, and S. Ludwigs, *Chem Rev*, **110** (8), 4724-4771 (2010).

UNIVERSITY OF ARKANSAS
J. WILLIAM FULBRIGHT COLLEGE OF ARTS & SCIENCES

Department of Chemistry and Biochemistry
Chemistry 119 • 1 University of Arkansas • Fayetteville AR 72701-1201
(479) 575-4601 • (479) 575-4049 (FAX)
http://chemistry.uark.edu • cheminfo@uark.edu

July 9, 2020

To Whom It May Concern:

On behalf of members in my research group and investigators at the University of Utah and Texas Tech University who performed scientific studies with Benjamin J. Jones, I confirm that he contributed the majority of the work described in his dissertation.

Sincerely,

Professor

4. X-Ray Photoelectron Spectroscopy of Two Thiophene Derivatives in Both Polymer and Monomer forms on Gold Surfaces

4.1 Abstract

X-ray photoelectron spectroscopy was used to characterize the relative composition of two thiophene derivative monomers, (2,3-dihydrothieno[3,4-b]dioxin-2-yl)methanol (**1**) and 4-((2,3-dihydrothieno[3,4-b][1,4]dioxin-2-yl)-methoxy)-4-oxobutanoic acid (**2**), dropcast on a gold surface as well as a series of electroplymerized films of the two monomers at varying molar ratios, on gold electrode surfaces. For the initial inspection of the monomers survey scans and narrow scans of the C(1s) region were performed. Upon qualitative differentiation between the two monomers in a 50:50 monomer mixture based on the shapes of the peaks within the C(1s) a more quantitative study was performed on a series of electropolymerized copolymers of the two monomers on gold microbands within an array. Survey scans followed by narrow scans of both the O(1s) and C(1s) regions were used to assess the relative mol% **2** composition of the polymer films to compare with the mol% **2** of the deposition solutions. A shift in a shoulder of the O(1s) peak from 530.5 eV to 532.5 eV showed the increasing presence of carboxyl and ester associated oxygen atoms within films produced from deposition solutions with an increasing mol% **2** of the monomer containing both carboxylic acid and ester functional groups. Narrow scans within the C(1s) regions for each of the films showed an increase in higher binding energy carbon atoms associated with carboxylic acid and ester groups. These spectra were deconvoluted and fit with seven synthetic components which correspond to the seven different carbons within the two monomers. These results provide further evidence that the relative composition of the monomers in the electropolymerized films is proportional to their mol% **2** in the deposition solution.

4.2 Introduction

The modification of an electroactive surface by electropolymerization of conductive polymers is an efficient way control its surface chemistry. Depending on the application it may be advantageous for a surface to consist of certain specific moieties at specific molar ratios. This is especially true for implanted biomedical and conductivity based sensor devices.[1-3] The electrodeposition of a mixture of desired conductive monomers in solution at specific molar ratios is an efficient way toward a surface with specific chemical properties. Monomers with contrasting yet simultaneously advantageous properties can be copolymerized, as is the case for the two thiophene derivatives, (2,3-dihydrothieno[3,4-b]dioxin-2-yl)methanol (**1**) and 4-((2,3-dihydrothieno[3,4-b][1,4]dioxin-2-yl)-methoxy)-4-oxobutanoic acid (**2**), shown in Figure 4.1. These two monomers have similar electrochemical properties to that of 3,4-ehthylenedioxythiophene (EDOT) (Figure 4.1) such as low oxidation potentials, stability in ambient and physiological conditions, linear polymerization through α-α' coupling which results in highly conductive films. However, they differ in both solubility and functionality. Monomer **1** is hydrophilic and soluble in aqueous conditions whereas monomer **2** is more hydrophobic and requires pretreatment before dissolution in aqueous environments. Although both monomers have low oxidation potentials and copolymers are readily electrodeposited from solutions containing both monomers, the characteristics of the electropolymerization does not provide information about the physical composition of the copolymer and the relative concentrations of both monomers compared to their molar ratios in solution. There is an interest in a quantitative assessment of the copolymer composition to understand if there is a correlation between the monnomers' molar ratio in solution and in the corresponding copolymer.

X-ray photoelectron spectroscopy (XPS) has been used to analyze the surface of polymers and copolymers of similar structure.[4] In most cases these results indicated the presence of monomers in the film and not their relative concentrations.[5, 6] Previous work involving the copolymerization of EDOT and monomer **1** used spectroelectrochemistry to define the reactivity ratio of the monomers to predict their relative concentration in resulting copolymers under certain conditions. Results showed preference for one monomer over the other up to equal molar ratios in the deposition solution.[7] In a following paper by the same group, XPS and Fourier transform infrared spectroscopy was used to characterize another set of copolymers. They found preference for the monomer 6-(2,3-dihydrothieno[3,4-b]-1,4-dioxin-2-yl methoxy)hexanoic acid, a derivative of monomer **1**, to be incorporated into the film over monomer **1** at a 50:50 molar ratio in acetonitrile.

XPS was used to gain better understanding of how monomers **1** and **2** are incorporated into copolymer films resulting from electropolymerization from deposition solutions of varying molar ratios. Preliminary studies involved the characterization of monomers **1** and **2** independently as well a 50:50 monomer mixture. Based on the qualitative analysis of the monomers a series of six of the seven copolymer films of monomers **1** and **2** shown in Figure 4.2 were quantitatively analyzed using XPS.

4.3 Experimental

4.3.1 Chemicals and materials. All chemicals were reagent grade and used as received unless otherwise specified. Monomer **1** was purchased from Sigma-Aldrich (St. Louis, MO, USA). Dichloromethane (DCM), and alumina (Neutral, Brockman Activity I) were purchased from Fisher Scientific (Pittsburg, PA, USA). DCM was dried over alumina in a glass

chromatography column prior to use. Chip design and fabrication, synthesis of monomer **2**, and the electropolymerization of the copolymer films has been described in chapters 2, 3, and 3S.

4.3.2 Preparation of monomer samples. Monomers were dissolved in dry DCM at a concentration of 0.02 M. For the XPS measurement of each monomer independently, an aliquot of monomer **1** was dropcast on the right large electrode of the chip and an aliquot of monomer **2** was dropcast on the left large electrode. The chip dried in a well-ventilated petri dish to avoid contamination from the surroundings. The 50:50 mixture of monomers was prepared by combining equal volumes of the individual 0.02 M in DCM monomer solutions. On a separate chip an aliquot of the 50:50 mixture was dropcast on the large electrodes and dried in the same way as described above.

4.3.3 Characterization of monomers and monomer mixtures by XPS. XPS measurements of the monomers were performed using a PHI 5000 VersaProbe III (Physical Electronics, Chanhassen, MN, USA) using a monochromatic aluminum source (Al Kα 1486.6 eV). The x-ray power was set to 23.5 W and a neutralizer energy of 1.5 V and current of 20.0 μA was used. The source analyzer angle was set to 45˚. The x-ray beam diameter was 100.0 μm and centered on the large gold chip-based electrode where the samples were dropcast. The chips were ground to the sample stage by applying carbon tape along all contact pads and fixing to the stage. Survey scans and narrow scans of the C(1s) region were performed. Samples of each monomer and a 50:50 mixture were analyzed.

4.3.4 Characterization of polymers by XPS. XPS measurements of the copolymers were carried out on a Kratos Axis Ultra DLD spectrometer (Kratos Analytical Ltd., Manchester, UK) using a monochromatic aluminum source (Al Kα 1486.6 eV). An x-ray gun emission current of 0.01 A, anode voltage of 15 kV, and bias voltage of 125 V was used to bombard the

modified microelectrode surface. The aperture size and iris position were both 110 µm centered on the 100 µm wide modified microelectrodes. High resolution scans of the C(1s) core electrons were obtained using a pass energy of 40 eV and step size of 0.1 eV. Copper tape was used to short the contact pads of the chip and ground it to the sample stage. A charge neutralizer gun was used to compensate for any charge accumulation during the measurement. Survey scans of one electrode per chip was performed along with narrow scans of the C(1s), O(1s), and Au(4f) regions were completed. Samples of each copolymer type were analyzed.

4.3.5 Analysis of XPS results. All XPS data were analyzed using CasaXPS software (Casa Software, Ltd., Teignmouth, UK). A linear background and line shapes of a Gaussian-Lorentzian sum form were used. Spectra were referenced to the C(1s) value of 284.6 eV to compensate for any charging.

XPS data of the dropcast monomers was qualitatively analyzed by observing the main peaks in the survey scans and the comparing number of discernable peaks, and their shifts, in the narrow scan of the C(1s) region. This was done to verify an observable difference between the spectra of the two monomers and a mixture of the two. These preliminary measurements would serve as a starting point for a more in-depth analysis of the composition of the electropolymerized films.

Survey scans of the electropolymerized films were analyzed for major components. The narrow scan of Au(4f) served to verify the presence of some exposed gold on the edges, and in some instances in the center, of the electrodes. The O(1s) region narrow scans were qualitatively analyzed and compared to one another. Because the aperture size and iris position were larger (110 µm) than the width of the electrode (100 µm) some of the O(1s) intensity is due to the SiO_2 on the surface of the chip, in between the electrodes. This makes a quantitative assessment of the

O(1s) content within each film impractical. However, the C(1s) region was quantitatively analyzed, deconvoluted, and fitted using CasaXPS software (Casa Software, Ltd., Teignmouth, UK). A linear background and line shapes of a Gaussian-Lorentzian sum form were used. Constraints were forced on the peak area, full-width at half maximum (FWHM), and binding energy position of the synthetic components.

For the quantitative analysis of the C(1s) region of the polymer films the first film analyzed was the 100 mol% **2**. This is because both monomers, and thus films produced from a combination of them, have the same carbon species. Seven different synthetic components were used to deconvolute the raw data of the 100 mol% **2** and used as the basis of comparison for all other films. A reference value of 284.6 eV was used to shift spectra in the Spectrum Processing tool of CasaXPS. The C(1s) region from 280 to 296 eV was manually created using the Quantification Parameters tool. In the Components tab, seven regions were created, one for each type of carbon, and then the components were fit. It was necessary to create additional components to account for π-π* interactions detected in some of the spectra. This first fit is a mathematical approximation and does not reflect the chemistry, but was necessary for generating a Standard Report from the Report Spec. tab and to note the total area of the envelope, which is the summation of all the components. An estimation of the approximate area each type of carbon should occupy in the deconvolution was completed prior to the data analysis and was based on the relative amounts of each carbon present at the ratio of the monomers represented by the deposition solutions. From this estimated area the individual component peaks were adjusted. For each component, the default relative sensitivity factor (R.S.F. = 1.0) and line shape (asymmetric based on the Lorentzian functional form (LA (1.53,243)) were used. The main items that were constrained were area, full-width at half maximum (fwhm), and position. The area for

each component was set to the estimated percent of total area of the envelope and constrained to ± 2 area units. The fwhm was also constrained to a range of 1.25 to 1.35. Another fit of the components based on these initial constraints was performed. Based on those results, the relative positions of the peaks were adjusted manually. The relative positions of the components were arranged, from lowest binding energy to highest, as follows: C-C, C-S, C=C, CH_2-O, CH-O, OC=O, C=OOH. As the component relative positions were manually adjusted, they were also constrained to a ± 0.5 eV range. The adjustments and constraints were continued until the relative standard deviation of the fit was minimized while maintaining a deconvolution with parameters that reflected the correct estimated chemical and physical nature of the films. The components were copied and pasted to the other films' XPS results as a starting point. The areas were then adjusted to the theoretical percentage of the total area of the envelope and the process was repeated. When fitting the 0 mol% **2** results, the C-C, OC=O, and C=OOH components were removed as those carbons were not considered to be in the 0 mol% **2** film

4.4 Results and Discussion

4.4.1 Qualitative analysis of dropcast monomers 1 and 2, and a 50:50 mixture, on a gold surface by XPS.

A comparison of the survey spectra and C(1s) region of the two monomers independent from one another was done by XPS. Figures 4.3a, 4.3c, and 4.3e are the survey scans of monomer **1**, the 50:50 mixture, and monomer **2**, respectively. In each of the survey scans peaks from O, Au, C, S, and Si are present. The increased background of the survey scan for monomer **1** may be due to increased scan time to produce observable signal. Because the monomers were dropcast on the electrode using a solvent with a high vapor pressure solvent pooling may have occurred, causing the monomer to be spread non-homogenously across the large gold surface with respect to the X-ray spot size.

The narrow scans of the C(1s) region (282 – 292 eV) of monomer **1**, the 50:50 monomer mixture, and monomer **2** are shown in Figures 4.3b, 4.3d, and 4.3f. In Figure 4.3b the large peak at 284.6 eV is from the carbons in the thiophene ring. The shoulder around 286.5 eV is caused by the carbons located in the ethylenedioxy bridge and the methylene adjacent to the hydroxyl group. In the 50:50 mixture of the monomers (Figure 4.3d) the shoulder has become a more pronounced peak at 286.5 eV. The addition of monomer **2** increases the relative concentration of the forms of carbon present in monomer **1** and introduces carbons with higher binding energies adjacent to the ester and carboxylate groups giving rise to a peak at 288.6 eV. These features are observed in the spectra of monomer **2** (Figure 4.3f). The peak at 286.5 eV increased in relative intensity and the highest energy peak has shifted slightly to 289 eV.

These results indicate a reasonable expectation for XPS analysis to assess the relative composition of the monomers in a series of copolymer films based on the content of the different carbon species associated with each monomer.

4.4.2 Relative composition of monomers 1 and 2 in the polymer films by XPS.

Although there is a film formed upon oxidative polymerization resulting from solutions containing monomers, the relative physical composition of the film is not known based on the electrochemistry alone. Confirmation of the chemical composition of the films was obtained by XPS. Because the spot size (110 μm) was slightly larger than the microelectrode width (100 μm), the survey spectra (Figures 4.4a-f) measured peaks for silicon from the SiO_2-coated silicon substrate at 155 and 104 eV, corresponding to Si(2s) and Si(2p), respectively.

Narrow scans of the O(1s) for five electropolymerized films are shown Figures 4.5a-f. The spectra appear to all have approximately the same shape, except for the film electropolymerized from the 50 mol% **2** deposition solution. However, closer inspection reveals

a small shoulder at the base of the peak on the lower binding energy side of the 0 mol% **2** spectra. This small shoulder shifts from a lower binding energy to a higher binding energy with increasing mol% **2** in the deposition solution. This is evidence of an increase in carbonyl and ester associated oxygen atoms.[8] Oxygen atoms associated with alcohols have an approximate binding energy of 532.8 eV and those associated with carbonyl and ester groups generally have a higher binding energy of 533.7 eV. The shift of the shoulder is not clearly observed for the intermediate mol% **2** films but a comparison of the 0 and 100 mol% **2** films shows the slight shift in the shoulder from 530.5 to 532.5 eV. The observed shift is larger than the expected 0.9 eV difference between the two types of oxygens, however it is worth noting the spot size (110 μm) is larger than the polymer film modified electrode width (100 μm). The SiO_2 substrate on either side of the electrode may be contributing to the O(1s) signal and therefore a qualitative, rather than quantitative, assessment was pursued. For this reason a quantitative deconvolution and fit of synthetic components of the C(1s) region was performed.

Figure 4.6 shows C(1s) narrow scans of the 0, 25, 34, 50, 66, and 100 mol% **2** films. deconvolution and fitting of the spectra were performed to confirm contributions of the different carbons and, therefore, the two monomers toward the spectra. A careful balance between mathematical overfitting and reasonable assessment of the spectra considering the expected chemistry was the overall goal. Figure 4.6a is the deconvolution and fit of the 0 mol% **2** film to four synthetic components, one for each type of carbon and one for the contribution from π-π* shake-up within in the thiophene; for Figures 4.6b – 4.6f there are eight total synthetic components. See the color-coded carbons in the structure shown in Figure 4.6g as a guide. The first and second components (cyan and black) are from the carbons that are in-between the ester and carboxylic acid present only in monomer **2** and the carbons adjacent to the sulfur in the

thiophene ring present in both monomers at 284.1 ± 0.4 eV and 284.6 ± 0.1 eV, respectively. The third component (red) is attributed to the other two carbons in the thiophene ring at 285.44 ± 0.08 eV. One carbon in the ethylenedioxy bridge and the methylene carbon have been designated as equivalent and contribute to the fourth component (orange) at 286.5 ± 0.3 eV. The other carbon in the ethylenedioxy bridge is accounted for in the fifth component (blue) at 287.4 ± 0.3 eV. The sixth and seventh components are only present in films containing monomer **2** and are due to the carbons of the ester (green) and carboxylic acid (purple). They give rise to peaks at 288.6 ± 0.3 and 289.0 ± 0.4 eV, respectively. Despite the synthetic components and their specific position, there is an increase in signal corresponding to carbons with a higher binding energy as the films were produced from deposition solutions with increasing mol% **2**. Therefore, the XPS C(1s) spectra support the μATR-FTIR data and show an increase in the ester content of the films as the mol% **2** in the deposition solution increases. Because XPS is a surface analysis technique (depth of ~10 nm), these results also suggest there is not a major difference between the surface and the bulk composition of the film.

4.5 Conclusions

The relative concentration of monomers **1** and **2** were shown to be incorporated into electropolymerized films proportionally to their mol% **2** in the deposition solution by high resolution XPS analysis of the C(1s) region. These results indicate a reliable and reasonable expectation of the number of different functional groups on the surface of the film. Therefore, use of these films for further modification could be carefully designed based on the molar ratios. Future work would include XPS mapping of the surface to provide insight into the distribution of the monomers within the film. This information could also be helpful to better understand the electropolymerization mechanism.

4.6 Acknowledgements

We are grateful for financial support from the National Science Foundation (CBET-1336853 and CMI-1808286), the Arkansas Biosciences Institute, the major research component of the Arkansas Tobacco Settlement Proceeds Act of 2000, as well as Grant Number P30 GM103450 from the National Institutes of General Medicine Sciences of the National Institutes of Health (NIH). We recognize the support of the Arkansas Statewide MS facility staff and their help in obtaining the LC-ESI-MS data of the monomers. We recognize the support of the Arkansas Nano & Bio Materials Characterization Facility and its Director, Dr. Mourad Benamara, in obtaining the XPS data of the monomers. This work made use of the University of Utah Surface Analysis Lab shared facility of the Micron Technology Foundation Inc. Microscopy Suite sponsored by the College of Engineering, Health Sciences Center, Office of the Vice President for Research, and the Utah Science Technology and Research (USTAR) initiative of the State of Utah.

4.7 References

1. E. M. Ali, E. A. B. Kantchev, H.-h. Yu, and J. Y. Ying, *Macromolecules,* **40** (17), 6025-6027 (2007).

2. S. C. Luo, E. Mohamed Ali, N. C. Tansil, H. H. Yu, S. Gao, E. A. Kantchev, and J. Y. Ying, *Langmuir,* **24** (15), 8071-8077 (2008).

3. S.-C. Luo, B. Zhu, A. Nakao, R. Nakatomi, and H.-h. Yu, *Adv. Biomater. (Weinheim, Ger.),* (6), B423-B427 (2011).

4. S. K. M. Joensson, M. P. De Jong, L. Groenendaal, W. R. Salaneck, and M. Fahlman, *J. Phys. Chem. B,* **107** (39), 10793-10800 (2003).

5. N. Bhagwat, K. L. Kiick, and D. C. Martin, *J. Mater. Res.,* **29** (23), 2835-2844 (2014).

6. S. A. Spanninga, D. C. Martin, and Z. Chen, *J. Phys. Chem. C,* **114** (35), 14992-14997 (2010).

7. F. S. Marrikar, M. Brumbach, D. H. Evans, A. Lebrón-Paler, J. E. Pemberton, R. J. Wysocki, and N. R. Armstrong, *Langmuir,* **23** (3), 1530-1542 (2007).

8. G. P. López, D. G. Castner, and B. D. Ratner, *Surface and Interface Analysis,* **17** (5), 267-272 (1991).

4.8 Figures

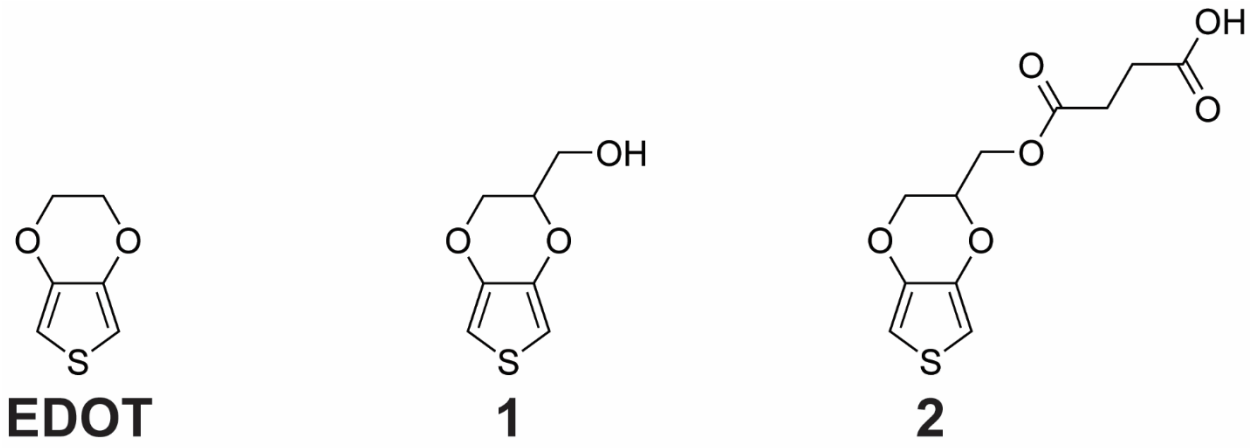

Figure 4.1. Molecular structures of monomers relevant to this work. EDOT, widely reported in the literature, shares the same base structure as **1** and **2**. Monomers **1** and **2** are synthesized independently from EDOT. Monomer **2** is synthesized from **1.**

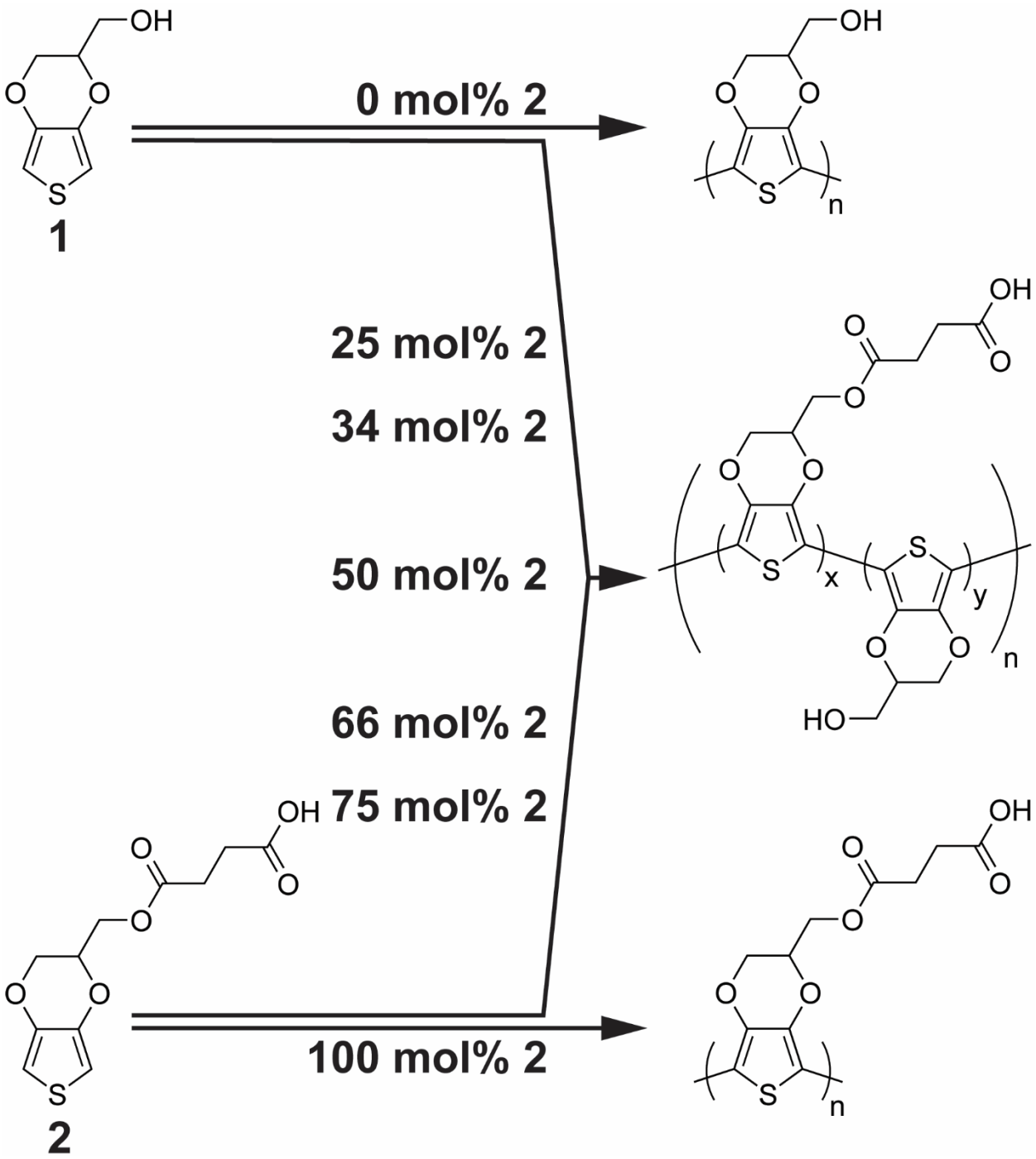

Figure 4.2. Strategy for electropolymerization of monomers **1** and **2** to form copolymer blends. The deposition solutions studied contained the following monomer **2** compositions: 0, 25, 34, 50, 66, 75, and 100 mol% **2**, where mol% **2** = [mol **2** / (mol **1** + mol **2**)] × 100%. The total monomer concentration in the deposition solutions was maintained constant at 0.02 M.

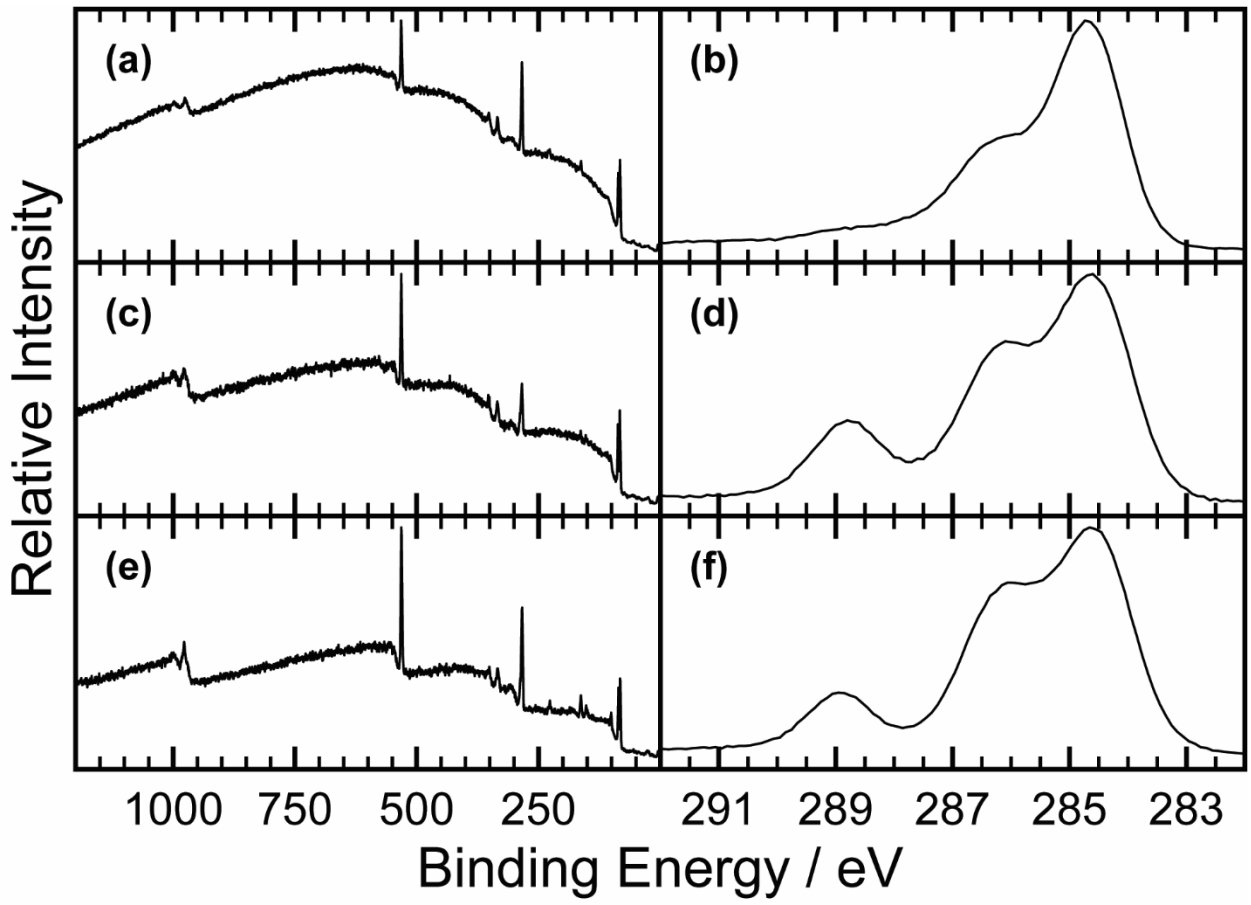

Figure 4.3. Survey scans of **(a)** monomer **1**, **(c)** 50:50 monomer mixture, and **(e)** monomer **2** alongside narrow scans of the C(1s) region for **(b)** monomer **1**, **(d)** 50:50 monomer mixture, and **(f)** monomer **2**.

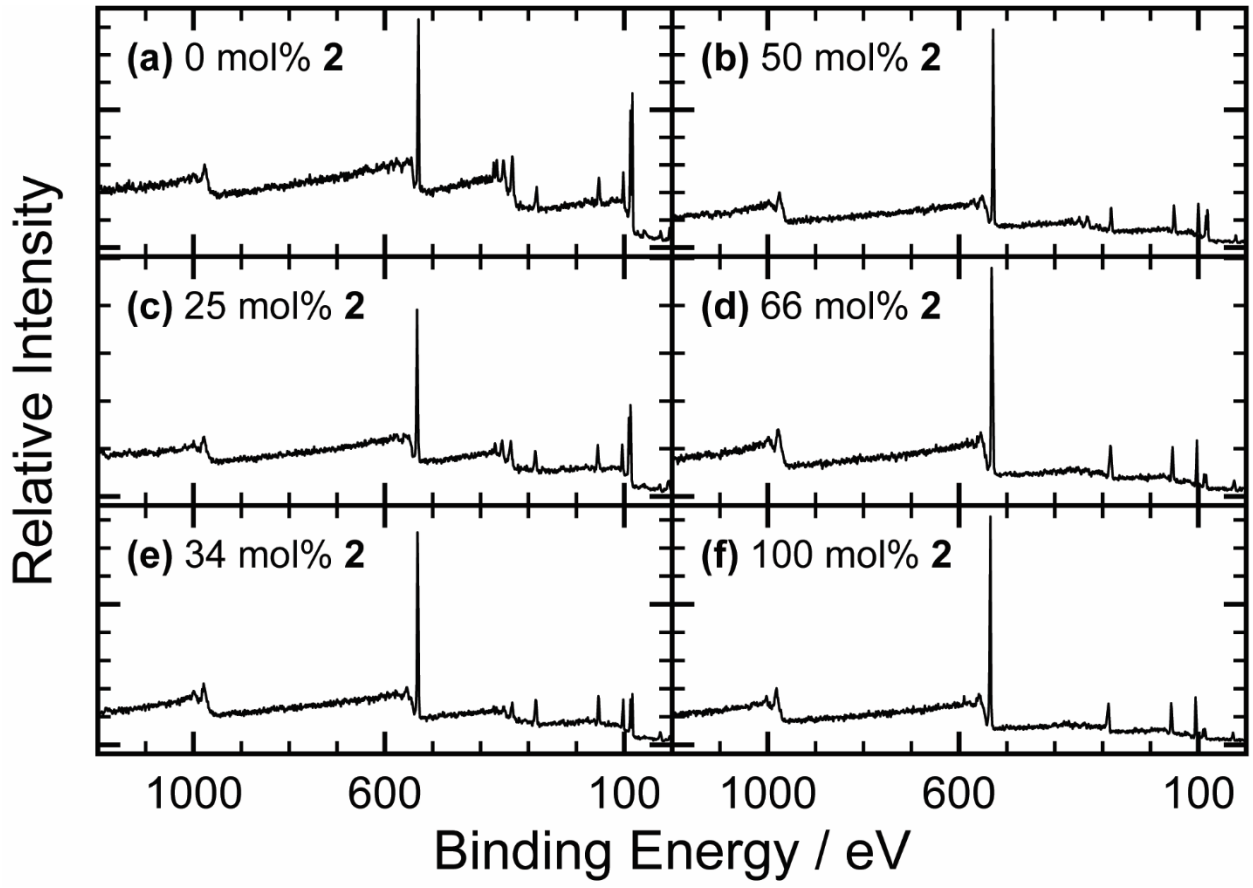

Figure 4.4. Survey scans of the electropolymerized polymers from deposition solutions containing **(a)** 0, **(c)** 25, **(e)** 34, **(b)** 50, **(d)** 66, and **(f)** 100 mol% **2**. Prominent peaks corresponding to O(1s) (532 eV), C(1s) (284.6 eV), Si (2s and 2p) (155 and 104 eV, respectively), and Au(4f) (90 and 87 eV) are observed in the survey scans of each polymer film.

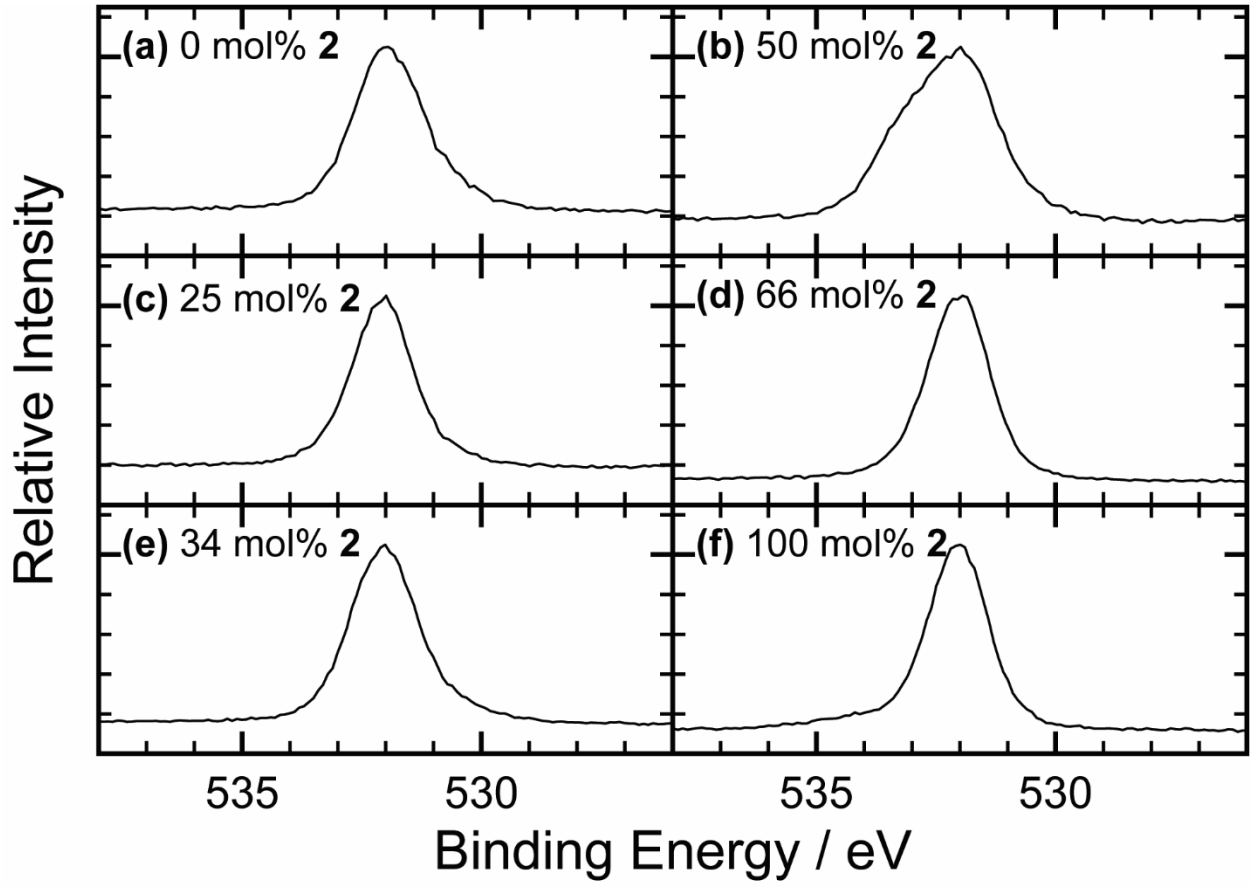

Figure 4.5. Narrow scans of the O(1s) region for electropolymerized films from deposition solutions containing **(a)** 0, **(c)** 25, **(e)** 34, **(b)** 50, **(d)** 66, and **(f)** 100 mol% **2**.

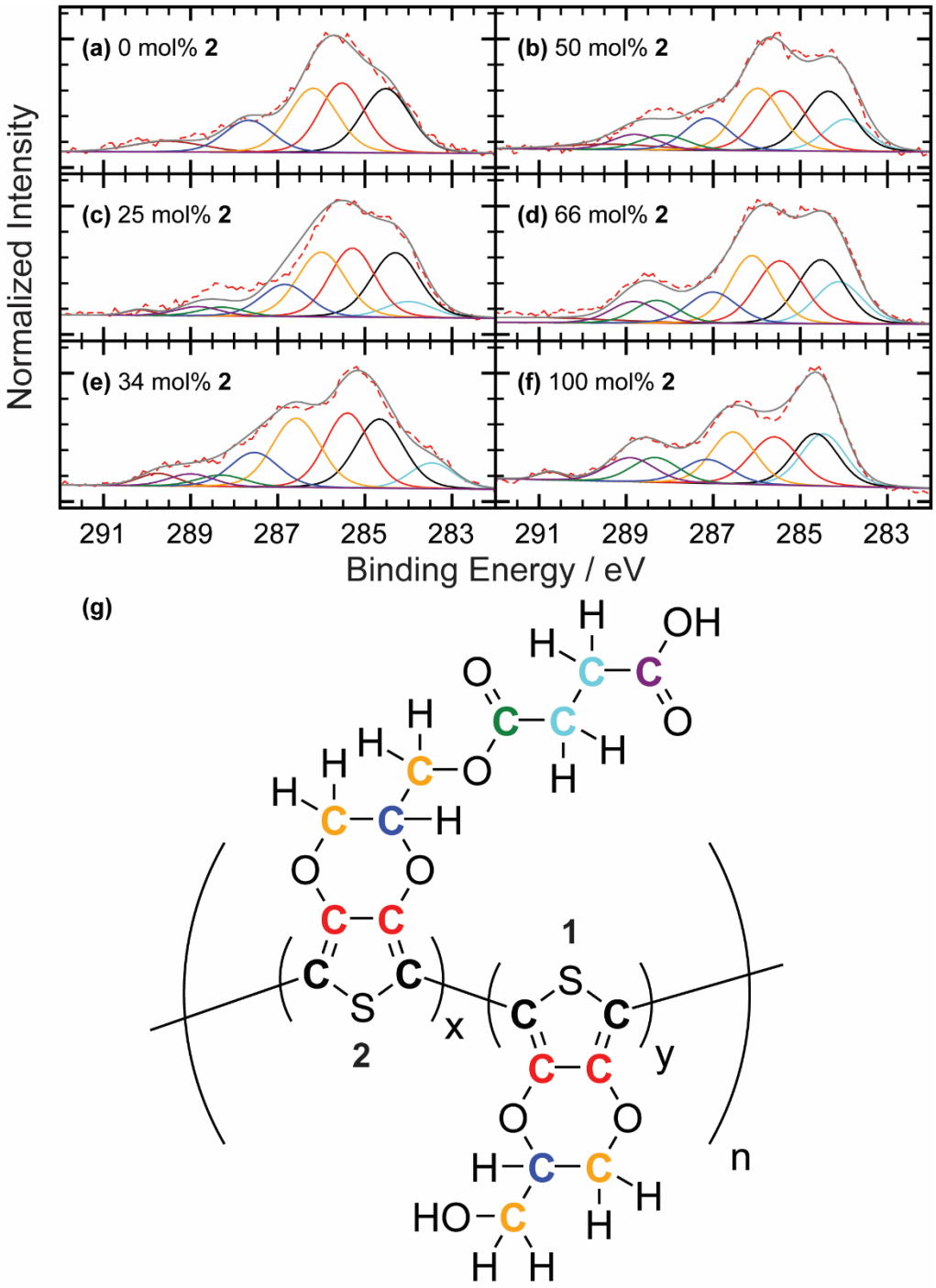

Figure 4.6. Deconvoluted and fitted C(1s) XPS spectra for **(a)** 0, **(b)** 50, **(c)** 25, **(d)** 66, **(e)** 34, and **(f)** 100 mol% **2**films. The raw XPS data is the red dotted line, the overall fit is the solid gray line, and each of the components in the deconvolution corresponds to the color coded carbons shown in **(g)** for both monomers **1** and **2**. All spectra are calibrated to 284.6 eV and additional peaks not attributed to carbon content of the monomers is due to π-π* shake-up. As the carbonyl content of the deposition solution increases the cps around 289 eV increases, which is directly related to the ester and carbonyl content of the films.

5. Conclusions and Future Work

5.1 Conclusions

The work completed in this dissertation shows the ability to co-electropolymerize thiophene derivative monomers to produce copolymer films of predictable relative concentrations based on their molar ratio in the deposition solution using the solubilizing agent SDS. This allows the surface of a micro-sized electroactive material to be modified with expected physical and electrochemical properties. A thiophene derivative monomer with the desired functionality of a carboxylic acid was synthesized and produced at high yield and characterized. This allowed co-electropolymerization with another thiophene derivative monomer on microband electrodes within an array at systematic molar ratios of the monomers in the aqueous deposition solutions. The more acidic deposition solutions were shown to produce films of fewer total monomers. By comparing the normalized capacitance to that of the normalized amount of total monomer deposited for each film it was concluded that the capacitance of each film was determined by the total number of monomer deposited and not the relative amount of mol% **2**. Also, electrodes that were modified with films containing 100 mol% **2** had the same capacitance value (0.065 ± 0.004 mF cm^{-2}, N=3) as that of the bare gold electrodes (0.0650 ± 0.0004 mF cm^{-2}, N=17). The elimination of an increased background current due to the conductive polymer film and available carboxylic acid functional groups make these modified electrodes ideal as a sensing platform upon further modification. The films were characterized by μATR-FTIR and XPS and it was shown that the relative concentration of each monomer within the film is linearly proportional to its respective molar ratio within the deposition solution. This demonstrates the ability to tune the chemistry of an electroactive surface by the directed placement and programmable thickness of polymer films of a specified molar ratio suitable for further derivatization.

5.2 Future Work

The work included in this dissertation demonstrates the ability to reliably predict the overall relative concentrations of the monomers within the co-electropolymerized films. However, these results do not provide information regarding the distribution of the monomers throughout the films. XPS and μATR-FTIR mapping of the copolymers could be performed to understand if the electropolymerization mechanism affects where certain monomers are positioned within the copolymer. Functional group mapping coupled with scanning electron microscopy (SEM) of each of the different films could discern any possible morphological differences between the films. SEM could also be used to determine the coverage of the polymer films on the electrode surface as well as height profiles of the edges and areas in which the polymer is not uniform along the electrode, as in the case of the 100 mol% **2** films.

As previously mentioned, the low background current of the 100 mol% **2** polymer makes it well suited for applications in sensing. The available carboxylic acid groups could be conjugated with a model redox compound, such as a ferrocene with either a primary amine or alcohol. The conjugation efficiency could be determined by comparing the amount of ferrocene detected electrochemically with the expected concentration of carboxylic acid groups within the film